ISSN 2518-7198 (Print)
ISSN 2663-5089 (Online)

BULLETIN
OF THE KARAGANDA UNIVERSITY

PHYSICS
Series

2024 • Volume 29 • Issue 2(114)

9ISSN 2663-5089 (Online)
ISSN-L 2518-7198 (Print)
Индексі 74616
Индекс 74616

ҚАРАҒАНДЫ УНИВЕРСИТЕТІНІҢ ХАБАРШЫСЫ

ВЕСТНИК КАРАГАНДИНСКОГО УНИВЕРСИТЕТА

BULLETIN OF THE KARAGANDA UNIVERSITY

ФИЗИКА сериясы

Серия ФИЗИКА

PHYSICS Series

2024

29-том • 2(114)-шығарылым
Том 29 • Выпуск 2(114)
Volume 29 • Issue 2(114)

1996 жылдан бастап шығады
Издается с 1996 года
Founded in 1996

Жылына 4 рет шығады
Выходит 4 раза в год
Published 4 times a year

Қарағанды / Караганда / Karaganda
2024

Редакцияның мекенжайы: 100024, Қазақстан, Қарағанды қ., Университет к-сі, 28
E-mail: vestnikku@gmail.com; karabekova71@mail.ru
Сайты: physics-vestnik.ksu.kz

Қарағанды университетінің хабаршысы. «Физика» сериясы. — 2024. — 29-т., 2(114)-шығ. — 93 б. — ISSN-L 2518-7198 (Print). ISSN 2663-5089 (Online).

Меншік иесі: «Академик Е.А. Бөкетов атындағы Қарағанды университеті» КЕАҚ.

Қазақстан Республикасы Ақпарат және қоғамдық даму министрлігімен тіркелген. 30.09.2020 ж. № KZ38VPY00027378 қайта есепке қою туралы куәлігі.

Басуға 28.06.2024 ж. қол қойылды. Пішімі 60×84 1/8. Қағазы ксерокстік. Көлемі 11,63 б.т. Таралымы 200 дана. Бағасы келісім бойынша. Тапсырыс № 49.

«Акад. Е.А. Бөкетов ат. Қарағанды ун-ті» КЕАҚ баспасының баспаханасында басылып шықты.
100024, Қазақстан, Қарағанды қ., Университет к-сі, 28. Тел. (7212) 35-63-16. E-mail: izd_kargu@mail.ru

Адрес редакции: 100024, Казахстан, г. Караганда, ул. Университетская, 28
E-mail: vestnikku@gmail.com; karabekova71@mail.ru
Сайт: physics-vestnik.ksu.kz

Вестник Карагандинского университета. Серия «Физика». — 2024. — Т. 29, вып. 2(114). — 93 с. — ISSN-L 2518-7198 (Print). ISSN 2663-5089 (Online).

Собственник: НАО «Карагандинский университет имени академика Е.А. Букетова».

Зарегистрирован Министерством информации и общественного развития Республики Казахстан. Свидетельство о постановке на переучет № KZ38VPY00027378 от 30.09.2020 г.

Подписано в печать 28.06.2024 г. Формат 60×84 1/8. Бумага ксероксная. Объем 11,63 п.л. Тираж 200 экз. Цена договорная. Заказ № 49.

Отпечатано в типографии издательства НАО «Карагандинский университет им. акад. Е.А. Букетова». 100024, Казахстан, г. Караганда, ул. Университетская, 28. Тел.(7212) 35-63-16. E-mail:izd_kargu@mail.ru

Postal address: 28, University Str., 100024, Karaganda, Kazakhstan
E-mail: vestnikku@gmail.com; karabekova71@mail.ru
Web-site: physics-vestnik.ksu.kz

Bulletin of the Karaganda University. "Physics" Series. — 2024. — Vol. 29, Iss. 2(114). — 93 p. — ISSN-L 2518-7198 (Print). ISSN 2663-5089 (Online).

Proprietary: NLC "Karagandy University of the name of academician E.A. Buketov".

Registered by the Ministry of Information and Social Development of the Republic of Kazakhstan. Rediscount certificate No. KZ38VPY00027378 dated 30.09.2020.

Signed in print 28.06.2024. Format 60×84 1/8. Photocopier paper. Volume 11,63 p.sh. Circulation 200 copies. Price upon request. Order № 49.

Printed in the Publishing house of NLC "Karagandy University of the name of acad. E.A. Buketov".
28, University Str., Karaganda, 100024, Kazakhstan. Tel. (7212) 35-63-16. E-mail: izd_kargu@mail.ru

МАЗМҰНЫ – СОДЕРЖАНИЕ – CONTENTS

КОНДЕНСАЦИЯЛАНҒАН КҮЙДІҢ ФИЗИКАСЫ
ФИЗИКА КОНДЕНСИРОВАННОГО СОСТОЯНИЯ
PHYSICS OF THE CONDENSED MATTER

ТЕХНИКАЛЫҚ ФИЗИКА
ТЕХНИЧЕСКАЯ ФИЗИКА
TECHNICAL PHYSICS

ЖЫЛУФИЗИКАСЫ ЖӘНЕ ТЕОРИЯЛЫҚ ЖЫЛУТЕХНИКАСЫ
ТЕПЛОФИЗИКА И ТЕОРЕТИЧЕСКАЯ ТЕПЛОТЕХНИКА
THERMOPHYSICS AND THEORETICAL THERMOENGINEERING

Article

Received: 09.01.2024
Accepted: 04.04.2024

UDC 535.8, 543.4

https://doi.org/10.31489/2024PH2/6-18

E.P. Menshova[1*], N.Kh. Ibrayev[1], N.D. Strekal[2]

[1]*Institute of Molecular Nanophotonics, Karaganda Buketov University, Karaganda, Kazakhstan;*
[2]*Yanka Kupala State University of Grodno, Grodno, Belarus*
[*]*(Corresponding author's e-mail: menshovayevgeniya @gmail.ru)*

Plasmon-enhanced sensitization of singlet oxygen on silver island films

The influence of the plasmonic effect of silver island films on the absorption, fluorescence and long-term luminescence of rose bengal in polyvinyl butyral films has been studied. Under the plasmon effect, the optical density of the dye increased by 3.3 times, the fluorescence intensity by 8.5 times, and the long-lived fluorescence and phosphorescence by 7.08 times and 10.21, respectively. It is shown that in the plasmon field of metal nanoparticles, both an increase in the excitation rate and an increase in the rates of radiative decay of excited singlet and triplet states occur. Phosphorescence of singlet oxygen with a lifetime of 86.46 μs was observed when excited in the absorption band of rose bengal. Based on the calculation of the quenching constants of rose bengal phosphorescence by molecular oxygen molecules, it is shown that the plasmonic effect enhances the energy transfer from dye triplets to oxygen molecules in collision complexes $[T_{PS}...^3\Sigma_g^-]$ as a result of heteroannihilation. Subsequently, the triplet pair decomposes to form a singlet oxygen molecule and a photosensitizer molecule in the ground state. The plasmonic effect of silver nanoparticles leads to an increase in the generation of singlet oxygen by 4.8 times.

Keywords: singlet oxygen generation, silver island films, plasmon effect, phosphorescence, long-lived fluorescence, photosensitizer, photodynamic therapy, molecular oxygen.

Introduction

Oncological diseases are a pressing problem both for Kazakhstan and the whole world. Over the past 20 years, the incidence of cancer has increased by 25% in our country. But the development of methods for diagnosing and treating the disease in the early stages reduced mortality by 33%.

One of the modern methods of cancer treatment is photodynamic therapy (PDT). The mechanism of PDT is complex and not fully understood. There are two processes occurring in tumor tissue: the photodynamic effect, sometimes called the photodynamic reaction, and the processes occurring in the tumor after its completion, that is the process of destruction of cancer cells [1].

Three main components are involved in PDT: light, a photosensitizing drug (photosensitizer - PS) and singlet oxygen $O_2(^1\Delta_g)$ [2]. The effectiveness of PDT is determined mainly by the level of PS accumulation, its localization in the cell and photochemical activity. This is due to the fact that in biosystems $O_2(^1\Delta_g)$ is quickly intercepted by amino acids and proteins and its lifetime is about 170–320 ns in the cytoplasm and 24–30 ns in the lipid phase of biomembranes. In cells containing many quenchers, the diffusion length of $O_2(^1\Delta_g)$ does not exceed 10–20 nm [3]. Consequently, $O_2(^1\Delta_g)$ can only damage biological structures in the immediate vicinity of photosensitizer molecules. Fluorescent microscopic studies have shown that PS mainly accumulates in membrane structures (plasma membrane, mitochondrial membranes), therefore they are considered the most likely primary targets, the defeat of which leads to cell damage and death [4–7].

Under the influence of a light quantum, O2(1Δg) is formed in the molecules of lipids, cell membrane proteins and intracellular organelles, which breaks the atomic bonds in the molecule and begins translational motion, moving in 1 μs to a distance of 50 Å [8]. The chain of the molecule is broken and destroyed with the formation of free radicals, which leads to damage to cell membranes. This process occurs within a few minutes after the start of laser irradiation [9, 10].

When a photosensitizer molecule absorbs a light quantum, it transforms into an excited singlet state (S_{1PS}) and then into a long-lived triplet state (T_{PS}) (reaction (1)). The transfer of energy from the PS in the triplet state to the oxygen molecule $O_2(^3\Sigma_g^-)$ transforms it into the singlet state $O_2(^1\Delta_g)$ (reaction (2)). Excited oxygen and photosensitizer molecules return to their original state and are able to enter into chemical reactions. The entire cycle can be restarted after the arrival of a new quantum of light energy. After several cycles, the photosensitizer "burns out" [11].

$$S_{0\,PS} + h\upsilon \rightarrow S_{1\,PS} \rightarrow T_{PS} \quad (1)$$

$$T_{PS} + {}^3\Sigma_g^- \rightarrow [T_{PS} \;\; {}^3\Sigma_g^-] \rightarrow S_{0\,PS} + {}^1\Delta_g. \quad (2)$$

Intensive development of PDT requires the development of new generations of PS based on nanomaterials with better photostability and higher efficiency of $O_2(^1\Delta_g)$ generation, as well as ways to improve the efficiency of existing ones [12–15]. For this purpose, the use of various types of metal nanoparticles and the creation of metal-PS composites are being considered [13, 16–19].

For the first time, Geddes et al. [20] observed and investigated possible mechanisms of $O_2(^1\Delta_g)$ generation under the influence of metal nanoparticles (NPs). Since then, many attempts have been made to explain this process. Many authors agree that a possible reason is an increase in the excitation rate as a result of an increase in the electric field around metal nanostructures [17, 21]. Consequently, the rate of intersystem crossing conversion ($S_{1PS} \rightarrow T_{PS}$) can be increased, which leads to increased energy transfer from PS molecules in the excited triplet state to the surrounding oxygen molecules with the formation of $O_2(^1\Delta_g)$. Also, the size and shape of silver clusters affect the performance of silver-enhanced $O_2(^1\Delta_g)$ generation [22].

The first fundamental studies were carried out on planar metal-photosensitizer systems [20]. Planar plasmonic nanostructures for studying plasmon-enhanced $O_2(^1\Delta_g)$ generation are usually fabricated by creating metal islands on a silicon or glass substrate. Metal islands can be synthesized using various approaches.

Reference [16] reported that by changing the plasmonic coupling parameters, such as nanoparticle size and shape, fluorophore/particle, and excitation wavelength of the coupling photosensitizer, the $O_2(^1\Delta_g)$ output can be easily tuned.

Various approaches to control the distance between PS molecules and the surface of a metal substrate on a nanometer scale made it possible to increase the generation of $O_2(^1\Delta_g)$ [23–25]. Firstly, this is due to the nonlinear propagation of the electric field in the environment, where the maximum electric field is observed at the surface of the metal and decreases exponentially with increasing distance from the surface. Secondly, nonlinear nonradiative energy transfer from excited PS molecules to the metal surface has an inverse relationship with the distance between the PS molecule and the metal surface [26].

For practical application of the planar metal- PS system, rigid glass and quartz substrates were replaced with flexible silicone ones. NPs were first incorporated into silicone polymers, and then PS molecules were sorbed on them. Silicone nanocomposites with NPs of various sizes have shown very effective antibacterial properties [27–30].

One of the important requirements for PCs for their practical use in PDT is their water solubility [31]. In this case, an important factor in the study is the interaction between colloidal metal NPs and PS molecules in solutions. PS molecules can be attached directly to the surface of metal NPs with their stabilizing substance through either electrostatic interaction or covalent bonding. Methods for attaching various PS molecules to metal NPs contained in various surfactant stabilizing substances, such as cetyltrimethylammonium bromide [32-33], poly(ethylene glycol) [34], tetraoctylammonium bromide [35-36], adenosine triphosphate [37], polyethyleneimine [38-39], was studied.

Metal NPs are mainly spherical gold and silver (AuNPs and AgNPs). But it is worth noting that the shape of NPs is another key factor influencing on the generation of $O_2(^1\Delta_g)$, because it determines the enhanced electric field as well as the amount of energy transferred. For example, Mthethwa and Nyokong [40] showed that Au nanobipyramids and Au nanorods (NRs) can enhance $O_2(^1\Delta_g)$ generation by 2-fold and 1.96-fold, respectively. It is assumed that the asymmetric shape and anisotropy in the enhanced electric field

around the metal NPs play a large role in the metal-enhanced $O_2(^1\Delta_g)$ generation [41]. Other studies have also shown that Au nanorods have better $O_2(^1\Delta_g)$ enhancement performance compared to spherical AuNPs [42]. Macia et al. [43] reported that silver nanocubes enhanced $O_2(^1\Delta_g)$ generation by rose bengal by 4 times. They concluded that the higher gain is due to the enhanced electric field at the sharp corners and edges of the nanocube.

As in planar metal-PS systems, plasmon-enhanced generation of singlet oxygen in colloidal systems is also distance dependent. To control the distance between PS molecules and metal NPs, silica and polymer shells are synthesized. PS molecules can be attached to the surface of the dielectric electrostatically [44], covalently [43, 45] and/or embedded inside the dielectric [46, 47]. When photosensitizer molecules are incorporated inside a dielectric layer such as silica, the final nanostructure becomes more biocompatible (due to the inertness of the dielectric layer) and has more potential for further modification (e.g. mesoporous silica shell structure) for in vivo applications with less dark cytotoxicity, because the PS molecules are not directly affected [48, 49]. When the PS molecules are attached to the surface of the dielectric layer through electrostatic interaction or covalent bonding, the distance between the PS and the metal nanoparticles is relatively easier to control [50, 51].

Fundamental research by our group showed the influence of Ag and Au NPs on the spectral and luminescent properties of xanthene [52], polymethine [52, 53], indopolycarbocyanine [21] and other dyes. The influence of the plasmonic effect of Ag nanoparticles (NPs) on singlet-singlet (S–S) and triplet-singlet (T–S) energy transfer in the same donor-acceptor pair of organic molecules was studied [52, 54]. A mathematical model was proposed that takes into account the influence of plasmonic nanoparticles on the deactivation of excited states of molecules [21, 52–55]. The distance dependence of plasmon-enhanced fluorescence and delayed luminescence of molecular planar nanostructures was also studied [55].

The purpose of this work is to study the process of enhancing the generation of singlet oxygen by dye molecules adsorbed on silver island films (SIFs).

Experimental

To study the plasmonic effect on $O_2(^1\Delta_g)$ generation, SIFs substrates were prepared using the chemical deposition method described in [52]. Then the films were annealed at 240^0C for 30 min. According to scanning electron microscope data (Mira 3LMU, Tescan), spherical islands with a size of 30–150 nm are uniformly distributed on the surface of the films (Fig. 1a). The broadened absorption spectra also indicate a large scatter in the sizes of islands in films obtained by chemical deposition (Fig. 1b).

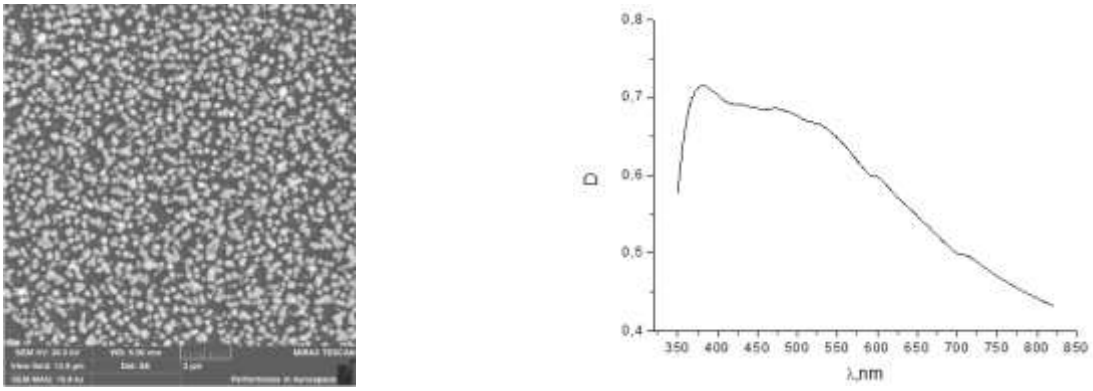

a b

Figure 1. SEM image (a) and absorption spectrum (b) of SIFs obtained by chemical deposition onto a cover glass

Rose Bengal (BR) dye was chosen as a PS [56]. Films of polyvinyl butyral (PVB, Sigma Aldrich) with a dye concentration of $5 * 10^{-5}$ M were obtained on the surface of clean cover glasses and SIFs using the spin-coating method.

Absorption, fast and long-lived luminescence spectra were recorded using Cary 300 and Eclipse spectrometers (Agilent Technologies). Measurements of delayed fluorescence (DF) and phosphorescence (Phos) of BR films were carried out using an Optistat DN vacuum cryostat (Oxford Instruments). The measurements were carried out with changes in pressure in the cryostat.

The decay kinetics of long-lived luminescence was recorded with an FLS1000 spectrometer (Edinburgh Instr.) with UV, Vis-PMT and NIR-PMT (Hamamatsu). Photoexcitation of the samples was carried out with an LQ529 Nd:YAG laser (SolarLS) with an excitation wavelength of 532 nm.

Results and Discussion

Figure 2 shows the absorption, fluorescence, and long-lived emission spectra of BR on pure glass and on SIFs. Optical density increased by 3.3 times on SIFs. The fluorescence intensity on SIFs increased by 8.5 times (Fig. 2a).

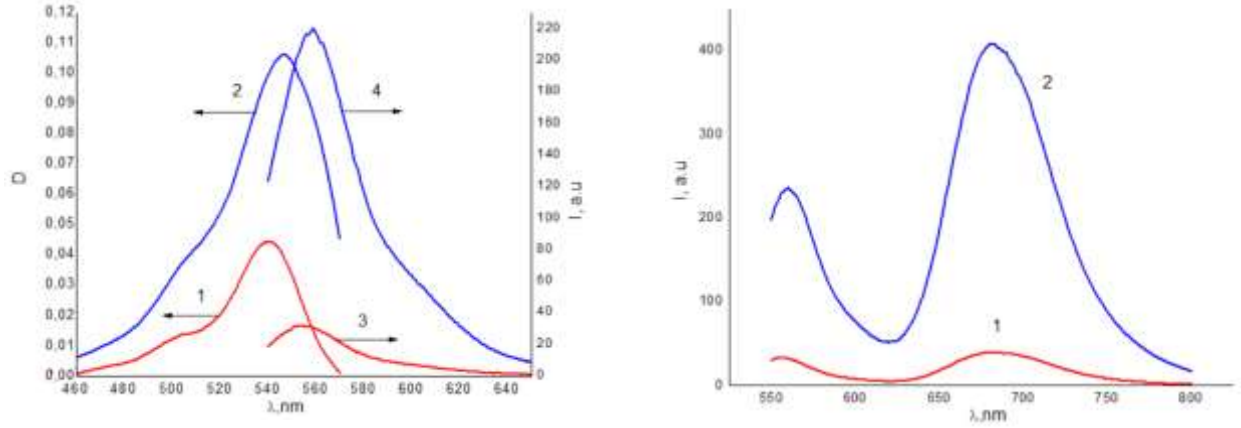

a b

Figure 2. (a) Absorption (1,2) and fluorescence (3,4) spectra of BR in a PVB film on glass (1,3) and on SIFs (2,4); (b) Long-lived emission spectra of BR on glass (1) and on SIFs (2) (λ_{ex} = 530 nm)

In the long-lived luminescence spectra of BR (Fig. 2b), two bands are observed: DF and Phos. The maximum of DF is at 560 nm, and Phos is at 685 nm. In the presence of Ag NPs, the intensity of DF increases by 7.08 times, and the intensity of Phos – by 10.21 (Table 1).

The Phos decay kinetics of BR on glass and on SIFs in air (curves 1) and in a degassed state at a pressure in a cryostat of 10^{-3} mBar (curves 2) are presented in Figure 3. The lifetime of long-lived emission in the presence of a plasmon decreases slightly for DF and Phos (Table 1). The observed increase in luminescence intensity with a simultaneous reduction in the duration of long-lived luminescence of BR on SIFs is a consequence of an increase in the rate of radiative decay [21, 55].

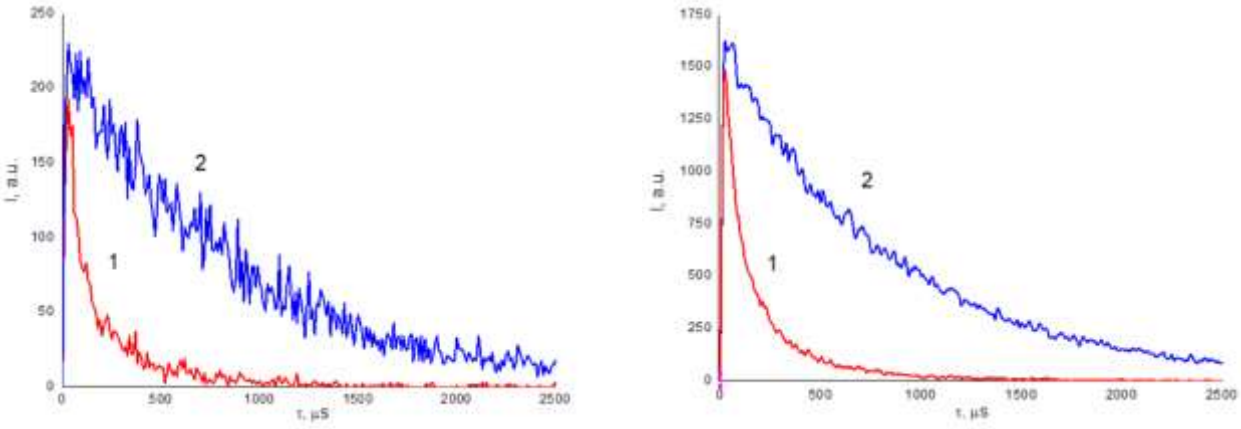

a b

Figure 3. Decay kinetics of BR Phos on glass (a) and on SIFs (b) with (1) oxygen and (2) without it (λ_{ex} = 530nm)

Table 1

Intensity, lifetime of DF and Phos of BR at an air pressure in a cryostat of 10^{-3} mBar on glass and SIFs (λ_{ex} = 530 nm)

	On glass		On SIFs		I/I_0	τ/τ_0
	I_0, o.e.	τ_0, ms	I, o.e.	τ, ms		
DF	33.41	0.85±0,1	236.49	0.81±0.1	7.08	0.95
Phos	40.06	0.80±0,1	408.82	0.78±0.1	10.21	0.98

The effect of oxygen concentration on DF and Phos in plasmon presence and without it was studied. Figure 4 shows the dependences of the intensity of DF and Phos on the pressure in the cryostat. For DF (curves 1, 2) on glass and on SIFs, an increase of the emission intensity up to 5 mBar is observed and then a decrease. While the intensity of phosphorescence (curves 3, 4) decreases monotonically.

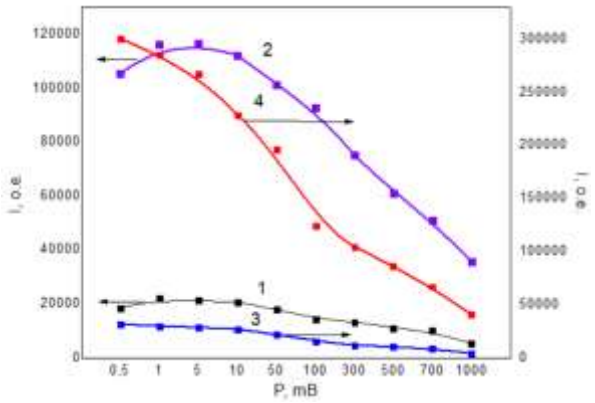

Figure 4. Dependence of the intensity of DF (1.2) and Phos (3.4) of BR on glass (2, 4) and on SIFs (1.3) on the pressure in the cryostat (λ_{ex} = 530 nm, λ_{reg} = 560 nm for DF and λ_{reg} = 690nm for Phos)

The dependence of the DF intensity on the $O_2\left({}^3\Sigma_g^-\right)$ concentration (Fig. 4) is the result of singlet-triplet annihilation (reaction (4)) between triplet-excited PS molecules and singlet oxygen molecules formed after its sensitization by the PS (reaction (3)):

$$T_{PS} + {}^3\Sigma_g^- \rightarrow [T_{PS}\ldots {}^3\Sigma_g^-] \rightarrow S_{0PS} + {}^1\Delta_g \quad (3)$$

$$T_{PS} + {}^1\Delta_g \rightarrow [T_{PS}\ldots {}^1\Delta_g]^3 \rightarrow S_{1\,PS} + {}^3\Sigma_g^- \rightarrow S_{0\,PS} + {}^3\Sigma_g^- + h\upsilon_{DF} \quad (4)$$

$$ {}^1\Delta_g \rightarrow {}^3\Sigma_g^- + h\upsilon_{Phos}\,, \quad (5)$$

where (3) is the reaction of singlet oxygen sensitization; (4) — singlet-triplet annihilation reaction; (5) — singlet oxygen phosphorescence reaction.

At low oxygen concentrations, the number of triplet PSs is still sufficient for the formation of $[T_{PS}\ldots {}^3\Sigma_g^-]$ pairs, which, decaying with the formation of S_1 states of the PS, additionally generate its DF [57–59]. This leads to an increase in DF intensity. With increasing oxygen concentration, stronger quenching of PS triplets occurs. As a result, the efficiency of both singlet–triplet (4) and intrinsic (1) annihilation processes decreases, which leads to a decrease in the intensity of PS luminescence.

Let's consider the effect of Ag NPs on the generation of singlet oxygen. Upon photoexcitation, phosphorescence of singlet oxygen was observed in the absorption band of the dye. $O_2({}^1\Delta_g)$ phosphorescence kinetic curves have two phases — rise and fall (Fig. 5) and can be approximated in accordance with the two-exponential equation:

$$I(t) = I_0\left[\exp\left(-\frac{t}{\tau_{decay}}\right) - \exp\left(-\frac{t}{\tau_{rise}}\right)\right],$$

where $I(t)$ — $O_2(^1\Delta_g)$ phosphorescence intensity per second, I_0 — pre-exponential factor, and τ_{decay} и τ_{rise} — the time constants of the decay and rise phases [60].

The rise phase is determined by the rate of formation of singlet oxygen as a result of energy transfer from BR triplets to $O_2\left(^3\Sigma_g^-\right)$, the decay phase is determined by the process of singlet oxygen deactivation.

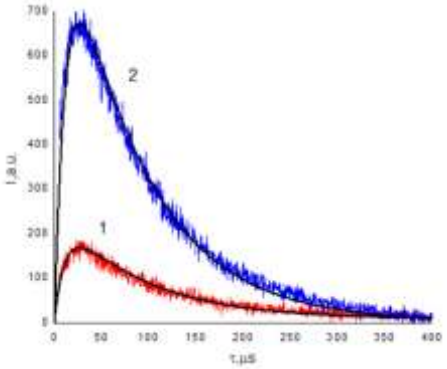

Figure 5. Decay kinetics of singlet oxygen phosphorescence (λ_{reg} = 1270 nm), sensitized with BR, on glass (1) and on SIFs (2) at atmospheric pressure (λ_{ex} = 530 nm)

Under the influence of the plasmon effect, the generation of singlet oxygen increases by 4.8 times (Fig. 5, Table 2). Under the influence of plasmon, the duration of the rise and decay phases of $O_2(^1\Delta_g)$ phosphorescence decreased by 14% and 3%, respectively. The decrease of the lifetime of $O_2(^1\Delta_g)$ phosphorescence is associated with an increase in the radiative transition $^1\Delta_g \rightarrow {}^3\Sigma_g^-$.

Table 2

Effect of SIFs on the integral intensities and lifetime of singlet oxygen (λ_{reg} = 1270 nm) at atmospheric pressure (λ_{ex} = 530 nm)

	$S \bullet 10^4$, o.e.	τ_{rise}, μs	τ_{decay}, μs	S/S_0	$\tau_{rise}/\tau_{rise\ 0}$	$\tau_{decay}/\tau_{decay\ 0}$
$O_2(^1\Delta_g)$ on glass	7.77	12.40±0.93	86.46±1.1	-	-	-
$O_2(^1\Delta_g)$ on SIFs	1.63	10.61±2.31	84.23±2.44	4.8	0.86	0.97

From the data on the effect of oxygen concentration above the sample surface on the intensity of phosphorescence, the quenching constants were determined from the Stern-Volmer equation [61; 75]:

$$\frac{I_{ph}^0}{I_{ph}} = 1 + k_q \tau_0 \cdot [Q],$$

where I_{ph}^0 — intensity of Phos in the absence of O_2, I_{ph} — intensity of Phos in the presence of O_2, k_q — the quenching coefficient, τ_0 — the lifetime of Phos in the absence of O_2, and $[Q]$ — the concentration of O_2.

Based on the Stern-Volmer graphs, the quenching constants of BR phosphorescence by oxygen molecules were calculated (Fig. 6). k_q =4,99 • 10^2 c^{-1} for dye films on glass, and k_q =6,48 • 10^2 c^{-1} on SIFs.

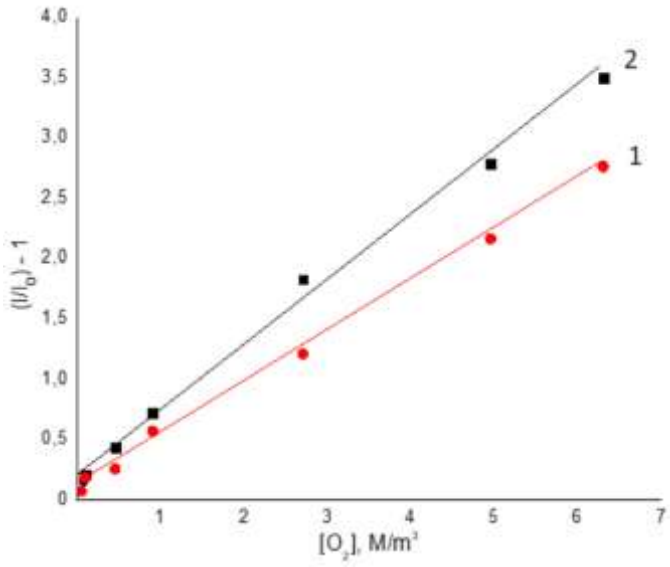

Figure 6. Stern-Volmer quenching constants of BR phosphorescence by O_2 molecules on glass (1) and on SIFs (2)

The obtained data indicate that the quenching of triplet BR molecules by molecular oxygen is enhanced in the plasmon field. The plasmonic effect promotes the transfer of energy from dye triplets to oxygen molecules in collision complexes $[T_{PS}...^3\Sigma_g^-]$ as a result of heteroannihilation. Subsequently, the triplet pair decomposes to form a singlet oxygen molecule $^1\Delta_g$ and $S_{0\,PS}$.

Conclusions

The influence of the plasmonic effect of silver nanoparticles on the absorption, fluorescence and long-term luminescence of BR in polyvinyl butyral films was studied. It was shown that in the plasmon field of metal nanoparticles, both an increase in the excitation rate and an increase in the rates of radiative decay of excited singlet and triplet states occur.

Phosphorescence of singlet oxygen with a lifetime of 86.46 μs was observed upon excitation in the absorption band of the dye. It was shown that the plasmonic effect promotes the quenching of triplet dye molecules by molecular oxygen. The intensity of the oxygen emission increased under the influence of the plasmon effect.

Acknowledgements

This research is funded by the Science Committee of the Ministry of Science and Higher Education of the Republic of Kazakhstan (Grant No. AP14870117).

References

1 Slesarevskaya M. Photodynamic therapy (Pdt): The main principles and mechanism of action / M. Slesarevskaya, A. Sokolov // Urologicheskie vedomosti. — 2012. — Vol. 2. — No. 3. — P. 24–28. DOI: 10.17816/uroved2324-28

2 Demidova T. Photodynamic therapy targeted to pathogens / T. Demidova, M. Hamblin // International Journal of Immunopathology and Pharmacology. — 2004. — Vol. 17. — No. 3. — P. 245–254. DOI:10.1177/039463200401700304

3 Hatz S. Measuring the lifetime of singlet oxygen in a single cell: Addressing the issue of cell viability / S. Hatz, J.D.C. Lambert, P.R. Ogilby // Photochemical & Photobiological Sciences. — 2007. — Vol. 6. — No. 10. — P. 1106–1116. DOI:10.1039/b707313e

4 Nelson J.S. Mechanism of tumor destruction following photodynamic therapy with hematoporphyrin derivative, chlorin, and phthalocyanine / J.S. Nelson, L.-H. Liaw, A. Orenstein, W.G. Roberts, M.W. Berns // JNCI Journal of the National Cancer Institute. — 1988. — Vol. 80. — No. 20. — P. 1599–1605. DOI:10.1093/jnci/80.20.1599

5 Berg K. Lysosomes as photochemical targets / K. Berg, J. Moan // International journal of cancer. — 1994. — Vol. 59. — No. 6. — P. 814–822. DOI: 10.1002/ijc.2910590618

6 Henderson B.W. How does photodynamic therapy work? / B.W. Henderson, T.J. Dougherty // Photochemistry and photobiology. — 1992. — Vol. 55. — No. 1. — P. 145–157. DOI: 10.1111/j.1751-1097.1992.tb04222.x

7 Jori G. The role of lipoproteins in the delivery of tumour-targeting photosensitizers / G. Jori, E. Reddi // The International journal of biochemistry. — 1993. — Vol. 25. — No. 10. — P. 1369–1375. DOI: 10.1016/0020-711x(93)90684-7

8 Байбеков И.М. Опыт использования светодиодного излучения в хирургии и других разделах медицины / И.М. Байбеков, В.П. Карташев, Д.Т. Пулатов, А.Х. Бутаев // В мире научных открытий. — 2017. — Т. 9. — № 2. — С. 54–69.

9 Moan J. The mechanism of photodynamic inactivation of human cells in vitro in the presence of haematoporphyrin / J. Moan, E.O. Pettersen, T. Christense // British journal of cancer. — 1979. — Vol. 39. — No. 4. — P. 398–407. DOI: 10.1038/bjc.1979.72

10 Specht K.G. Depolarization of mouse myeloma cell membranes during photodynamic action / K.G. Specht, M.A. Rodgers // Photochemistry and photobiology. — 1990. — Vol. 51. — No. 3. — P. 319–324. DOI: 10.1111/j.1751-1097.1990.tb01717.x

11 Karitskaya S.G. Photosensitized singlet oxygen and oxygen complexes in the occurrence and change of spatially inhomogeneous luminescence in solutions of anthraquinone / S.G. Karitskaya // Bulletin of the University of Karaganda – Physics. — 2019. — Vol. 93. — No. 1. — P. 32–43. DOI: 10.31489/2019Ph1/32-43

12 Tavakkoli Yaraki M. Metal-enhancement study of dual functional photosensitizers with aggregation-induced emission and singlet oxygen generation / M. Tavakkoli Yaraki, F. Hu, S. Daqiqeh Rezaei, B. Liu, Y.N. Tan // Nanoscale advances. — 2020. — Vol. 2. — No. 7. — P. 2859–2869. DOI: 10.1039/d0na00182a

13 Tavakkoli Yaraki M. Nanosilver-enhanced AIE photosensitizer for simultaneous bioimaging and photodynamic therapy / M. Tavakkoli Yaraki, Y. Pan, F. Hu, Y. Yu, B. Liu, Y.N. Tan // Materials Chemistry Frontiers. — 2020. — Vol. 4. — No. 10. — P. 3074–3085. DOI: 10.1039/D0QM00469C

14 Aslan K. Metal-enhanced fluorescence: An emerging tool in biotechnology / K. Aslan, I. Gryczynski, J. Malicka, E. Matveeva, J.R. Lakowicz, C.D. Geddes // Current Opinion in Biotechnology. — 2005. — Vol. 16. — No. 1. — P. 55–62. DOI: 10.1016/j.copbio.2005.01.001

15 Jain P.K. Review of Some Interesting Surface Plasmon Resonance-enhanced Properties of Noble Metal Nanoparticles and Their Applications to Biosystems / P.K. Jain, X. Huang, I.H. El-Sayed, M.A. El-Sayed // Plasmonics. — 2007 — Vol. 2. — P. 107–118. DOI: 10.1007/s11468-007-9031-1

16 Zhang Y. Plasmonic engineering of singlet oxygen generation / Y. Zhang, K. Aslan, M.J. Previte, C.D. Geddes // Proceedings of the National Academy of Sciences of the United States of America. — 2008. — Vol. 105. — No. 6. — P. 1798–1802. DOI: 10.1073/pnas.0709501105

17 Zhang Y. Metal-enhanced singlet oxygen generation: a consequence of plasmon enhanced triplet yields / Y. Zhang, K. Aslan, M.J. Previte, C.D. Geddes // Journal of fluorescence. — 2007. — Vol. 17. — No. 4. — P. 345–349. DOI: 10.1007/s10895-007-0196-y

18 Ragàs X. Singlet oxygen phosphorescence enhancement by silver islands films / X. Ragàs, A. Gallardo, Y. Zhang, W. Massad, C.D. Geddes, S. Nonell // The Journal of Physical Chemistry C. — 2011. — Vol. 115. — No. 33. — P. 16275–16281. DOI: 10.1021/jp202095a

19 Tavakkoli Yaraki M. Gold Nanostars-AIE Theranostic Nanodots with Enhanced Fluorescence and Photosensitization Towards Effective Image-Guided Photodynamic Therapy / M. Tavakkoli Yaraki, M. Wu, E. Middha, W. Wu, S. Daqiqeh Rezaei, B. Liu, Y.N. Tan // Nano-micro letters. — 2021. — Vol. 13. — No. 1. — P. 58. DOI: 10.1007/s40820-020-00583-2

20 Geddes C.D. Metal-enhanced fluorescence / C.D. Geddes // Physical chemistry chemical physics: PCCP. — 2013. — Vol. 15. — No. 45. — P. 19537. DOI: 10.1039/c3cp90129g

21 Seliverstova E. Competitive influence of the plasmon effect and energy transfer between chromophores and Ag nanoparticles on the fluorescent properties of indopolycarbocyanine dyes / E. Seliverstova, N. Ibrayev, G. Omarova, A. Ishchenko, M. Kucherenko // Journal of Luminescence. — 2021. — Vol. 235. — P. 118000. DOI: 10.1016/j.jlumin.2021.118000

22 Tavakkoli Yaraki M. Emerging strategies in enhancing singlet oxygen generation of nano-photosensitizers toward advanced phototherapy / M. Tavakkoli Yaraki, B. Liu, Y.N. Tan // Nano-Micro Letters. — 2022. — Vol. 14. — No. 1. — P. 123. DOI: 10.1007/s40820-022-00856-y

23 Zhang Y. Metal-enhanced fluorescence from silver-SiO2-silver nanoburger structures / Y. Zhang, L.N. Mandeng, N. Bondre, A. Dragan, C.D. Geddes // Langmuir: the ACS journal of surfaces and colloids. — 2010. — Vol. 26. — No. 14. — P. 12371–12376. DOI: 10.1021/la101801n

24 Zhang J. Metal-enhanced fluorescence of an organic fluorophore using gold particles / J. Zhang, J.R. Lakowicz // Optics express. — 2007. — Vol. 15. — No. 5. — P. 2598–2606. DOI: 10.1364/oe.15.002598

25 Szmacinski H. Large Fluorescence Enhancements of Fluorophore Ensembles with Multilayer Plasmonic Substrates: Comparison of Theory and Experimental Results / H. Szmacinski, R. Badugu, F. Mahdavi, S. Blair, J.R. Lakowicz // The journal of physical chemistry C, Nanomaterials and interfaces. — 2012. — Vol. 116. — No. 40. — P. 21563–21571. DOI: 10.1021/jp3072876

26 Cui Q. Controllable metal-enhanced fluorescence in organized films and colloidal system / Q. Cui, F. He, L. Li, H. Möhwald // Advances in colloid and interface science. — 2014. — Vol. 207. — P. 164–177. DOI: 10.1016/j.cis.2013.10.011

27 Noimark S. Photobactericidal polymers; the incorporation of crystal violet and nanogold into medical grade silicone / S. Noimark, M. Bovis, A.J. MacRobert, A. Correia, E. Allan, M. Wilson, I.P. Parkin // RSC Advances. — 2013. — Vol. 3. — No. 40. — P. 18383. DOI: 10.1039/c3ra42629g

28 Perni S. Prevention of biofilm accumulation on a light-activated antimicrobial catheter material / S. Perni, P. Prokopovich, I.P. Parkin, M. Wilson, J. Pratten // Journal of Materials Chemistry. — 2010. — Vol. 20. — No. 39. — P. 8668. DOI: 10.1039/c0jm01891k

29 Perni S. The antimicrobial properties of light-activated polymers containing methylene blue and gold nanoparticles / S. Perni, C. Piccirillo, J. Pratten, P. Prokopovich, W. Chrzanowski, I.P. Parkin, M. Wilson // Biomaterials. — 2009. — Vol. 30. — No. 1. — P. 89–93. DOI: 10.1016/j.biomaterials.2008.09.020

30 Perni S. Antibacterial Activity of Light-Activated Silicone Containing Methylene Blue and Gold Nanoparticles of Different Sizes / S. Perni, C. Piccirillo, A. Kafizas, M. Uppal, J. Pratten, M. Wilson & I.P. Parki // J Clust Sci. — 2010. — Vol. 21. — P. 427–438. DOI;10.1007/s10876-010-0319-5

31 Санарова Е.В. Фотодинамическая терапия — способ повышения селективности и эффективности лечения опухолей / Е.В. Санарова, Е.В. Ланцова, М.В. Дмитриева, З.С. Смирнова, Н.А. Оборотова // Рос. биотерапевт. журн. — 2014. — Т. 13. — № 3. — С. 109–118.

32 Zhou X. Au nanorods modulated NIR fluorescence and singlet oxygen generation of water soluble dendritic zinc phthalocyanine / X. Zhou, X. He, S. Wei, K. Jia, X. Liu // Journal of colloid and interface science. — 2016. — Vol. 482. — P. 252–259. DOI: 10.1016/j.jcis.2016.07.072

33 Wang J. AlPcS-loaded gold nanobipyramids with high two-photon efficiency for photodynamic therapy in vivo / J. Wang, X. Zhuo, X. Xiao, R. Mao, Y. Wang, J. Wang, J. Liu // Nanoscale. — 2019. — Vol. 11. — No. 7. — P. 3386–3395. DOI: 10.1039/c9nr00004f

34 Chu C.K. Combination of photothermal and photodynamic inactivation of cancer cells through surface plasmon resonance of a gold nanoring / C.K. Chu, Y.C. Tu, J.H. Hsiao, J.H. Yu, C.K. Yu, S.Y. Chen, P.H. Tseng, S. Chen, Y.W. Kiang, C.C. Yang // Nanotechnology. — 2016. — Vol. 27. — No. 11. — P. 115102. DOI: 10.1088/0957-4484/27/11/115102

35 Mthethwa T.P. Photophysical and photochemical properties of a novel thiol terminated low symmetry zinc phthalocyanine complex and its gold nanoparticles conjugate / T.P. Mthethwa, S. Tuncel, M. Durmuş, T. Nyokong // Dalton transactions (Cambridge, England: 2003). — 2013. — Vol. 42. — No. 14. — P. 4922–4930. DOI: 10.1039/c3dt32698e

36 Nombona N. Synthesis and photophysical studies of phthalocyanine-gold nanoparticle conjugates / N. Nombona, E. Antunes, C. Litwinski, T. Nyokong // Dalton transactions (Cambridge, England: 2003). — 2011. — Vol. 40. — No. 44. — P. 11876–11884. DOI: 10.1039/c1dt11151e

37 Yang W. Aggregation-induced enhancement effect of gold nanoparticles on triplet excited state / W. Yang, K. Liu, D. Song, Q. Du, R. Wang, H. Su // The Journal of Physical Chemistry C. — 2013. — Vol. 117. — No. 51. — P. 27088–27095. DOI: 10.1021/jp410369w

38 Yang Y. Intracellular gold nanoparticle aggregation and their potential applications in photodynamic therapy / Y. Yang, Y. Hu, H. Du, H. Wang // Chemical communications (Cambridge, England). — 2014. — Vol. 50. — No. 55. — P. 7287–7290. DOI: 10.1039/c4cc02376e

39 Khaing Oo M.K. Gold nanoparticle-enhanced and size-dependent generation of reactive oxygen species from protoporphyrin IX / M.K. Khaing Oo, Y. Yang, Y. Hu, M. Gomez, H. Du, H. Wang // ACS nano. — 2012. — Vol. 6. — No. 3. — P. 1939–1947. DOI: 10.1021/nn300327c

40 Mthethwa T. Photoinactivation of Candida albicans and Escherichia coli using aluminium phthalocyanine on gold nanoparticles / T. Mthethwa, T. Nyokong // Photochemical & photobiological sciences: Official journal of the European Photochemistry Association and the European Society for Photobiology. — 2015. — Vol. 14. — No. 7. — P. 1346–1356. DOI: 10.1039/c4pp00315b

41 Watkins Z. Fluorescence Behaviour and Singlet Oxygen Production of Aluminium Phthalocyanine in the Presence of Upconversion Nanoparticles / Z. Watkins, J. Taylor, S. D'Souza, J. Britton, T. Nyokong // Journal of fluorescence. — 2015. — Vol. 25. — No. 5. — P. 1417–1429. DOI: 10.1007/s10895-015-1632-z

42 Kuo W.S. Gold nanomaterials conjugated with indocyanine green for dual-modality photodynamic and photothermal therapy / W.S. Kuo, Y.T. Chang, K.C. Cho, K.C. Chiu, C.H. Lien, C.S. Yeh, S.J. Chen // Biomaterials. — 2012. — Vol. 33. — No. 11. — P. 3270–3278. DOI: 10.1016/j.biomaterials.2012.01.035

43 Macia N. Hybrid Silver Nanocubes for Improved Plasmon-Enhanced Singlet Oxygen Production and Inactivation of Bacteria / N. Macia, R. Bresoli-Obach, S. Nonell, B. Heyne // Journal of the American Chemical Society. — 2019. — Vol. 141. — No. 1. — P. 684–692. DOI: 10.1021/jacs.8b12206

44 Chen C.W. Plasmon-Enhanced Photodynamic Cancer Therapy by Upconversion Nanoparticles Conjugated with Au Nanorods / C.W. Chen, Y.C. Chan, M. Hsiao, R.S. Liu // ACS applied materials & interfaces. — 2016. — Vol. 8. — No. 47. — P. 32108–32119. DOI: 10.1021/acsami.6b07770

45 Mooi S.M. Amplified Production of Singlet Oxygen in Aqueous Solution Using Metal Enhancement Effects / S.M. Mooi, B. Heyne // Photochemistry and photobiology. — 2014. — Vol. 90. — No. 1. — P. 85–91. DOI: 10.1111/php.12176

46 Rosa-Pardo I. Fe_3O_4@Au@mSiO_2 as an enhancing nanoplatform for Rose Bengal photodynamic activity / I. Rosa-Pardo, M. Roig-Pons, A.A. Heredia, J.V. Usagre, A. Ribera, R.E. Galian, J. Pérez-Prieto // Nanoscale. — 2017. — Vol. 9. — No. 29. — P. 10388–10396. DOI: 10.1039/c7nr00449d

47 Zampini G. Cover feature: Effects of gold colloids on the photosensitization efficiency of silica particles doped with protoporphyrin ix / G. Zampini, L. Tarpani, G. Massaro, M. Gambucci, A. Nicoziani, L. Latterini // ChemPhotoChem. — 2017. — Vol. 1. — No. 12. — P. 533–533. DOI: 10.1002/cptc.201700209

48 Chu Z. Surface plasmon enhanced drug efficacy using core-shell Au@SiO2 nanoparticle carrier / Z. Chu, C. Yin, S. Zhang, G. Lin, Q. Li // Nanoscale. — 2013. — Vol. 5. — No. 8. — P. 3406–3411. DOI: 10.1039/c3nr00040k

49 Junqueira H.C. Modulation of methylene blue photochemical properties based on adsorption at aqueous micelle interfaces / H.C. Junqueira, D. Severino, L.G. Dias, M.S. Gugliotti, M.S. Baptista // Physical Chemistry Chemical Physics. — 2002. — Vol. 4. — No. 11. — P. 2320–2328. DOI: 10.1039/b109753a

50 Planas O. Distance-Dependent Plasmon-Enhanced Singlet Oxygen Production and Emission for Bacterial Inactivation / O. Planas, N. Macia, M. Agut, S. Nonell, B. Heyne // Journal of the American Chemical Society. — 2016. — Vol. 138. — No. 8. — P. 2762–2768. DOI: 10.1021/jacs.5b12704

51 Lismont M. Protoporphyrin IX-Functionalized $AgSiO_2$ Core-Shell Nanoparticles: Plasmonic Enhancement of Fluorescence and Singlet Oxygen Production / M. Lismont, L. Dreesen, B. Heinrichs, C.A. Páez // Photochemistry and photobiology. — 2016. — Vol. 92. — No. 2. — P. 247–256. DOI: 10.1111/php.12557

52 Ibrayev N. Plasmon effect on simultaneous singlet-singlet and triplet-singlet energy transfer / N. Ibrayev, E. Seliverstova, D. Temirbayeva, A. Ishchenko // Journal of Luminescence. — 2022. — Vol. 251. — P. 119203. DOI: 10.1016/j.jlumin.2022.119203.

53 Ibrayev N.Kh. Effect of plasmon resonance of metal nanoparticles on spectral-luminescent properties of polymethine dye / N.Kh. Ibrayev, E.V. Seliverstova, N.D. Zhumabay, G.S. Omarova, A.A. Ishchenko // Bulletin of the University of Karaganda – Physics. — 2018. — Vol. 91. — No. 3. — P. 37–41.

54 Temirbayeva D. Plasmon effect on triplet-singlet energy transfer in the dye-doped Langmuir-Blodgett films / D. Temirbayeva, N. Ibrayev, E. Seliverstova, M. Kudinova, A. Ishchenko // Bulletin of the University of Karaganda – Physics. — 2022. — Vol. 108. — No. 4. — P. 6–13. DOI:10.31489/2022ph4/6-13

55 Temirbayeva D. Distance dependence of plasmon-enhanced fluorescence and delayed luminescence of molecular planar nanostructures / D. Temirbayeva, N. Ibrayev, M. Kucherenko // Journal of Luminescence. — 2022. — Vol. 243. — P. 118642. DOI: 10.1016/j.jlumin.2021.118642

56 Redmond R.W. A compilation of singlet oxygen yields from biologically relevant molecules / R.W. Redmond, J.N. Gamlin // Photochemistry and photobiology. — 1999. — Vol. 70. — No. 4. — P. 391–475

57 Kenner R.D. Singlet oxygen-triplet organic molecule annihilation fluorescence in polymer matrices / R.D. Kenner, A. Khan // Chemical Physics Letters. — 1975. — Vol. 36. — P. 643–646.

58 Bryukhanov V.V. Enhancement of delayed fluorescence of aromatic hydrocarbons in polymer matrices by singlet oxygen / V.V. Bryukhanov, N.K. Ibraev, G.A. Ketsle, L.V. Levshin, Z.M. Muldakhmetov, Z.K. Smagulov // Journal of Applied Spectroscopy. — 1986. — Vol. 45. — P. 1263–1266

59 Kucherenko M.G. Triplet exciton reactions in MEH-PPV films registered by accompanying magneto-sensitive photoluminescence / M.G. Kucherenko, S.A. Penkov // Journal of Photochemistry and Photobiology A: Chemistry. — 2023. — Vol. 437. — P. 114440. DOI: 10.1016/j.jphotochem.2022.114440

60 Krasnovsky A.A. Luminescence and photochemical studies of singlet oxygen photonics / A.A. Krasnovsky // Journal of Photochemistry and Photobiology A: Chemistry. — 2008. — Vol. 196. — No. 2–3. — P. 210–218. DOI: 10.1016/j.jphotochem.2007.12.015

61 Паркер С.А. Фотолюминесценция растворов / С.А. Паркер; под ред. Р.Ф. Васильева; пер. с англ. — М.: Мир, 1972. — 510 с.

Е.П. Меньшова, Н.Х. Ибраев, Н.Д. Стрекаль

Күміс аралдық қабыршақтардағы синглетті оттегінің плазмонмен күшейтілген сенсибилизациясы

Күміс аралдық қабыршақтардың плазмондық әсерінің поливинилбутирал қабыршақтарындағы бенгал раушанының жұтылуына, флуоресценциясына және ұзақ мерзімді люминесценциясына әсері зерттелді. Плазмонның әсерінен бояғыштың оптикалық тығыздығы 3,3 есе, флуоресценция қарқындылығы 8,5 есе, ал баяу флуоресценция мен фосфоресценция сәйкесінше 7,08 және 10,21 есе өсті. Металл нанобөлшектерінің плазмондық өрісінде қозу жылдамдығының жоғарылауы да, қозған синглет пен триплет күйлерінің радиациялық ыдырау жылдамдығының да жоғарылауы анықталды. Бенгал раушанының жұтылу жолағында қозған кезде өмір сүру уақыты 86,46 мкс болатын синглетті оттегінің фосфоресценциясы байқалды. Бенгал раушанының фосфоресценциясын молекулалық оттегі молекулаларымен сөндіру константаларын есептеу негізінде, плазмондық әсер гетероаннигиляция нәтижесінде соқтығысу кешендеріндегі $[T_{ФС}...^3\Sigma_g^-]$ бояғыш триплеттерінен оттегі молекулаларына энергияның берілуін күшейтуге ықпал ететіндігі көрсетілген. Кейіннен триплет жұбы ыдырап, синглетті оттегі молекуласын және негізгі күйдегі фотосенсибилизатор молекуласын түзеді. Күміс нанобөлшектерінің плазмондық әсері синглетті оттегінің 4,8 есе көбеюіне әкеледі.

Кілт сөздер: синглетті оттегінің генерациясы, күміс аралдық қабыршақ, плазмондық әсер, фосфоресценция, баяу флуоресценция, фотосенсибилизатор, фотодинамикалық терапия, молекулалық оттегі.

Е.П. Меньшова, Н.Х. Ибраев, Н.Д. Стрекаль

Плазмон-усиленная сенсибилизация синглетного кислорода на островковых пленках серебра

Исследовано влияние плазмонного эффекта островковых пленок серебра на поглощение, флуоресценцию и длительную люминесценцию бенгальской розы в пленках поливинилбутираля. Под воздействием плазмона оптическая плотность красителя возросла в 3,3 раза, интенсивность флуоресценции — в 8,5, а замедленной флуоресценции и фосфоресценции — в 7,08 и в 10,21 раз, соответственно. Показано, что в плазмонном поле металлических наночастиц происходит как увеличение скорости возбуждения, так и рост скоростей радиационного распада возбужденных синглетных и триплетных состояний. При возбуждении в полосе поглощения бенгальской розы наблюдалась фосфоресценция синглетного кислорода со временем жизни 86.46 мкс. На основе расчета констант тушения фосфоресценции бенгальской розы молекулами молекулярного кислорода показано, что плазмонный эффект способствует усилению передачи энергии от триплетов красителя к молекулам кислорода в комплексах столкновения $[T_{ФС}...^3\Sigma_g^-]$ в результате гетероаннигиляции. В последующем триплетная пара распадается с образованием молекулы синглетного кислорода и молекулы фотосенсибилизатора в основном состоянии. Плазмонный эффект наночастиц серебра приводит к увеличению генерации синглетного кислорода в 4,8 раза.

Ключевые слова: генерация синглетного кислорода, островковые пленки серебра, плазмонный эффект, фосфоресценция, замедленная флуоресценция, фотосенсибилизатор, фотодинамическая терапия, молекулярный кислород.

References

1 Slesarevskaya, M.N., & Sokolov, A.V. (2012). Photodynamic therapy (Pdt): The main principles and mechanism of action. *Urologicheskie vedomosti*, *2*(3), 24–28.

2 Demidova, T.N., & Hamblin, M.R. (2004). Photodynamic therapy targeted to pathogens. *International Journal of Immunopathology and Pharmacology*, *17*(3), 245–254.

3 Hatz, S., Lambert, J.D.C., & Ogilby, P.R. (2007). Measuring the lifetime of singlet oxygen in a single cell: Addressing the issue of cell viability. *Photochemical & Photobiological Sciences*, *6*(10), 1106–1116.

4 Nelson, J.S., Liaw, L.-H., Orenstein, A., Roberts, W.G., & Berns, M.W. (1988). Mechanism of tumor destruction following photodynamic therapy with hematoporphyrin derivative, chlorin, and phthalocyanine. *JNCI Journal of the National Cancer Institute*, *80*(20), 1599–1605.

5 Berg, K., & Moan, J. (1994). Lysosomes as photochemical targets. *International journal of cancer*, *59*(6), 814–822.

6 Henderson, B.W., & Dougherty, T.J. (1992). How does photodynamic therapy work? *Photochemistry and photobiology*, *55*(1), 145–157.

7 Jori, G., & Reddi, E. (1993). The role of lipoproteins in the delivery of tumour-targeting photosensitizers. *The International journal of biochemistry*, *25*(10), 1369–1375.

8 Baybekov, I.M., Kartashev, V.P., Pulatov, D.T. & Butaev, A.Kh. (2017). Opyt ispolzovaniia svetodiodnogo izlucheniia v khirurgii i drugikh razdelakh meditsiny [Experience in using LED radiation in surgery and other areas of medicine]. *V mire nauchnykh otkrytii — In the world of scientific discoveries, 9*(2), 54–69 [in Russian].

9 Moan, J., Pettersen, E.O., & Christensen, T. (1979). The mechanism of photodynamic inactivation of human cells in vitro in the presence of haematoporphyrin. *British journal of cancer*, *39*(4), 398–407.

10 Specht, K.G., & Rodgers, M.A. (1990). Depolarization of mouse myeloma cell membranes during photodynamic action. *Photochemistry and photobiology*, *51*(3), 319–324.

11 Karitskaya, S.G. (2019). Photosensitized singlet oxygen and oxygen complexes in the occurrence and change of spatially inhomogeneous luminescence in solutions of anthraquinone. *Bulletin of the University of Karaganda – Physics*, *93*(1), 32–43.

12 Tavakkoli Yaraki, M., Hu.F., Daqiqeh Rezaei, S., Liu, B., & Tan, Y.N. (2020). Metal-enhancement study of dual functional photosensitizers with aggregation-induced emission and singlet oxygen generation. *Nanoscale advances*, *2*(7), 2859–2869.

13 Tavakkoli Yaraki, M., Pan, Y., Hu, F., Yu, Y., Liu, B., & Tan, Y.N. (2020). Nanosilver-enhanced AIE photosensitizer for simultaneous bioimaging and photodynamic therapy. *Materials Chemistry Frontiers*, *4*(10), 3074–3085.

14 Aslan, K., Gryczynski, I., Malicka, J., Matveeva, E., Lakowicz, J.R., & Geddes, C.D. (2005). Metal-enhanced fluorescence: An emerging tool in biotechnology. *Current Opinion in Biotechnology*, *16*(1), 55–62.

15 Jain, P.K., Huang, X., El-Sayed, I.H., & El-Sayed, M.A. (2007). Review of Some Interesting Surface Plasmon Resonance-enhanced Properties of Noble Metal Nanoparticles and Their Applications to Biosystems. *Plasmonics*, *2*, 107–118.

16 Zhang, Y., Aslan, K., Previte, M.J., & Geddes, C.D. (2008). Plasmonic engineering of singlet oxygen generation. *Proceedings of the National Academy of Sciences of the United States of America*, *105*(6), 1798–1802.

17 Zhang, Y., Aslan, K., Previte, M.J., & Geddes, C.D. (2007). Metal-enhanced singlet oxygen generation: a consequence of plasmon enhanced triplet yields. *Journal of fluorescence*, *17*(4), 345–349.

18 Ragàs, X., Gallardo, A., Zhang, Y., Massad, W., Geddes, C.D., & Nonell, S. (2011). Singlet oxygen phosphorescence enhancement by silver islands films. *The Journal of Physical Chemistry C*, *115*(33), 16275–16281.

19 Tavakkoli Yaraki, M., Wu, M., Middha, E., Wu, W., Daqiqeh Rezaei, S., Liu, B., & Tan, Y.N. (2021). Gold Nanostars-AIE Theranostic Nanodots with Enhanced Fluorescence and Photosensitization Towards Effective Image-Guided Photodynamic Therapy. *Nano-micro letters*, *13*(1), 58.

20 Geddes, C.D. (2013). Metal-enhanced fluorescence. *Physical chemistry chemical physics: PCCP*, *15*(45), 19537.

21 Seliverstova, E., Ibrayev, N., Omarova, G., Ishchenko, A., & Kucherenko, M. (2021). Competitive influence of the plasmon effect and energy transfer between chromophores and Ag nanoparticles on the fluorescent properties of indopolycarbocyanine dyes. *Journal of Luminescence*, *235*, 118000.

22 Tavakkoli Yaraki, M., Liu, B., & Tan, Y.N. (2022). Emerging strategies in enhancing singlet oxygen generation of nanophotosensitizers toward advanced phototherapy. *Nano-Micro Letters*, *14*(1), 123.

23 Zhang, Y., Mandeng, L.N., Bondre, N., Dragan, A., & Geddes, C.D. (2010). Metal-enhanced fluorescence from silver-SiO2-silver nanoburger structures. *Langmuir: the ACS journal of surfaces and colloids*, *26*(14), 12371–12376.

24 Zhang, J., & Lakowicz, J.R. (2007). Metal-enhanced fluorescence of an organic fluorophore using gold particles. *Optics express*, *15*(5), 2598–2606.

25 Szmacinski, H., Badugu, R., Mahdavi, F., Blair, S., & Lakowicz, J.R. (2012). Large Fluorescence Enhancements of Fluorophore Ensembles with Multilayer Plasmonic Substrates: Comparison of Theory and Experimental Results. *The journal of physical chemistry. C, Nanomaterials and interfaces*, *116*(40), 21563–21571.

26 Cui, Q., He, F., Li, L., & Möhwald, H. (2014). Controllable metal-enhanced fluorescence in organized films and colloidal system. *Advances in colloid and interface science*, *207*, 164–177.

27 Noimark, S., Bovis, M., MacRobert, A.J., Correia, A., Allan, E., Wilson, M., & Parkin, I.P. (2013). Photobactericidal polymers; the incorporation of crystal violet and nanogold into medical grade silicone. *RSC Advances*, *3*(40), 18383.

28 Perni, S., Prokopovich, P., Parkin, I.P., Wilson, M., & Pratten, J. (2010). Prevention of biofilm accumulation on a light-activated antimicrobial catheter material. *Journal of Materials Chemistry*, *20*(39), 8668.

29 Perni, S., Piccirillo, C., Pratten, J., Prokopovich, P., Chrzanowski, W., Parkin, I. P., & Wilson, M. (2009). The antimicrobial properties of light-activated polymers containing methylene blue and gold nanoparticles. *Biomaterials*, *30*(1), 89–93.

30 Perni, S. et al. (2010). Antibacterial Activity of Light-Activated Silicone Containing Methylene Blue and Gold Nanoparticles of Different Sizes. *J Clust Sci* 21, 427–438.

31 Sanarova, E.V., Lantsova, E.V., Dmitrieva, M.V., Smirnova, Z.S., & Oborotova, N.A. (2014). Fotodinamicheskaia terapiia — sposob povysheniia selektivnosti i effektivnosti lecheniia opukholei [Photodynamic therapy is a way to increase the selectivity and effectiveness of tumor treatment]. *Rossiiskii bioterapevticheskii zhurnal — Russian Biotherapeutic Journal*, *13*(3), 109–118 [in Russian].

32 Zhou, X., He, X., Wei, S., Jia, K., & Liu, X. (2016). Au nanorods modulated NIR fluorescence and singlet oxygen generation of water soluble dendritic zinc phthalocyanine. *Journal of colloid and interface science*, *482*, 252–259.

33 Wang, J., Zhuo, X., Xiao, X., Mao, R., Wang, Y., Wang, J., & Liu, J. (2019). AlPcS-loaded gold nanobipyramids with high two-photon efficiency for photodynamic therapy in vivo. *Nanoscale*, *11*(7), 3386–3395.

34 Chu, C.K., Tu, Y.C., Hsiao, J.H., Yu, J.H., Yu, C.K., Chen, S.Y., Tseng, P.H., Chen, S., Kiang, Y.W., & Yang, C.C. (2016). Combination of photothermal and photodynamic inactivation of cancer cells through surface plasmon resonance of a gold nanoring. *Nanotechnology*, *27*(11), 115102.

35 Mthethwa, T.P., Tuncel, S., Durmuş, M., & Nyokong, T. (2013). Photophysical and photochemical properties of a novel thiol terminated low symmetry zinc phthalocyanine complex and its gold nanoparticles conjugate. *Dalton transactions (Cambridge, England: 2003)*, *42*(14), 4922–4930.

36 Nombona, N., Antunes, E., Litwinski, C., & Nyokong, T. (2011). Synthesis and photophysical studies of phthalocyanine-gold nanoparticle conjugates. *Dalton transactions (Cambridge, England: 2003)*, *40*(44), 11876–11884.

37 Yang, W., Liu, K., Song, D., Du, Q., Wang, R., & Su, H. (2013). Aggregation-induced enhancement effect of gold nanoparticles on triplet excited state. *The Journal of Physical Chemistry C*, *117*(51), 27088–27095.

38 Yang, Y., Hu, Y., Du, H., & Wang, H. (2014). Intracellular gold nanoparticle aggregation and their potential applications in photodynamic therapy. *Chemical communications (Cambridge, England)*, *50*(55), 7287–7290.

39 Khaing Oo, M.K., Yang, Y., Hu, Y., Gomez, M., Du, H., & Wang, H. (2012). Gold nanoparticle-enhanced and size-dependent generation of reactive oxygen species from protoporphyrin IX. *ACS nano*, *6*(3), 1939–1947.

40 Mthethwa, T., & Nyokong, T. (2015). Photoinactivation of Candida albicans and Escherichia coli using aluminium phthalocyanine on gold nanoparticles. *Photochemical & photobiological sciences: Official journal of the European Photochemistry Association and the European Society for Photobiology*, *14*(7), 1346–1356.

41 Watkins, Z., Taylor, J., D'Souza, S., Britton, J., & Nyokong, T. (2015). Fluorescence Behaviour and Singlet Oxygen Production of Aluminium Phthalocyanine in the Presence of Upconversion Nanoparticles. *Journal of fluorescence*, *25*(5), 1417–1429.

42 Kuo, W.S., Chang, Y.T., Cho, K.C., Chiu, K.C., Lien, C.H., Yeh, C.S., & Chen, S.J. (2012). Gold nanomaterials conjugated with indocyanine green for dual-modality photodynamic and photothermal therapy. *Biomaterials*, *33*(11), 3270–3278.

43 Macia, N., Bresoli-Obach, R., Nonell, S., & Heyne, B. (2019). Hybrid Silver Nanocubes for Improved Plasmon-Enhanced Singlet Oxygen Production and Inactivation of Bacteria. *Journal of the American Chemical Society*, *141*(1), 684–692.

44 Chen, C.W., Chan, Y.C., Hsiao, M., & Liu, R.S. (2016). Plasmon-Enhanced Photodynamic Cancer Therapy by Upconversion Nanoparticles Conjugated with Au Nanorods. *ACS applied materials & interfaces*, *8*(47), 32108–32119.

45 Mooi, S.M., & Heyne, B. (2014). Amplified Production of Singlet Oxygen in Aqueous Solution Using Metal Enhancement Effects. *Photochemistry and photobiology*, *90*(1), 85–91.

46 Rosa-Pardo, I., Roig-Pons, M., Heredia, A.A., Usagre, J.V., Ribera, A., Galian, R.E., & Pérez-Prieto, J. (2017). Fe_3O_4@Au@mSiO_2 as an enhancing nanoplatform for Rose Bengal photodynamic activity. *Nanoscale*, *9*(29), 10388–10396.

47 Zampini, G., Tarpani, L., Massaro, G., Gambucci, M., Nicoziani, A., & Latterini, L. (2017). Cover feature: Effects of gold colloids on the photosensitization efficiency of silica particles doped with protoporphyrin ix. *ChemPhotoChem*, *1*(12), 533–533.

48 Chu, Z., Yin, C., Zhang, S., Lin, G., & Li, Q. (2013). Surface plasmon enhanced drug efficacy using core-shell Au@SiO2 nanoparticle carrier. *Nanoscale*, *5*(8), 3406–3411.

49 Junqueira, H.C., Severino, D., Dias, L.G., Gugliotti, M.S., & Baptista, M.S. (2002). Modulation of methylene blue photochemical properties based on adsorption at aqueous micelle interfaces. *Physical Chemistry Chemical Physics*, *4*(11), 2320–2328.

50 Planas, O., Macia, N., Agut, M., Nonell, S., & Heyne, B. (2016). Distance-Dependent Plasmon-Enhanced Singlet Oxygen Production and Emission for Bacterial Inactivation. *Journal of the American Chemical Society*, *138*(8), 2762–2768.

51 Lismont, M., Dreesen, L., Heinrichs, B., & Páez, C.A. (2016). Protoporphyrin IX-Functionalized $AgSiO_2$ Core-Shell Nanoparticles: Plasmonic Enhancement of Fluorescence and Singlet Oxygen Production. *Photochemistry and photobiology*, *92*(2), 247–256.

52 Ibrayev, N., Seliverstova, E., Temirbayeva, D., & Ishchenko, A. (2022). Plasmon effect on simultaneous singlet-singlet and triplet-singlet energy transfer. *Journal of Luminescence*, *251*, 119203.

53 Ibrayev N.Kh., Seliverstova E.V., Zhumabay N.D., Omarova G.S., & Ishchenko A.A. (2018). Effect of plasmon resonance of metal nanoparticles on spectral-luminescent properties of polymethine dye. *Bulletin of the University of Karaganda – Physics*, *91*(3), 37–41.

54 Temirbayeva, D., Ibrayev, N., Seliverstova, E., Kudinova, M., & Ishchenko, A. (2022). Plasmon effect on triplet-singlet energy transfer in the dye-doped Langmuir-Blodgett films. *Bulletin of the University of Karaganda – Physics*, *108*(4), 6–13.

55 Temirbayeva, D., Ibrayev, N., & Kucherenko, M. (2022). Distance dependence of plasmon-enhanced fluorescence and delayed luminescence of molecular planar nanostructures. *Journal of Luminescence*, *243*, 118642.

56 Redmond, R.W., & Gamlin, J.N. (1999). A compilation of singlet oxygen yields from biologically relevant molecules. *Photochemistry and photobiology*, *70*(4), 391–475.

57 Kenner, R.D., & Khan, A. (1975). Singlet oxygen-triplet organic molecule annihilation fluorescence in polymer matrices. *Chemical Physics Letters*, *36*, 643-646.

58 Bryukhanov, V.V., Ibraev, N.K., Ketsle, G.A., Levshin, L.V., Muldakhmetov, Z.M., & Smagulov, Z.K. (1986). Enhancement of delayed fluorescence of aromatic hydrocarbons in polymer matrices by singlet oxygen. *Journal of Applied Spectroscopy*, *45*, 1263-1266.

59 Kucherenko, M.G., & Penkov, S.A. (2023). Triplet exciton reactions in MEH-PPV films registered by accompanying magneto-sensitive photoluminescence. *Journal of Photochemistry and Photobiology A: Chemistry*, *437*, 114440.

60 Krasnovsky, A.A. (2008). Luminescence and photochemical studies of singlet oxygen photonics. *Journal of Photochemistry and Photobiology A: Chemistry*, *196*(2–3), 210–218.

61 Parker, S.A. (1972). Fotoliuminestsentsiia rastvorov / R.F. Vasilev (Ed.). Moscow: Mir, 510 [in Russian].

Information about authors

Menshova, Evgeniya — Junior Research Fellow, Institute of Molecular Nanophotonics, Karaganda Buketov University, Karaganda, Kazakhstan; e-mail: menshovayevgeniya@gmail.com; ORCID ID: https://orcid.org/0000-0003-3646-3763;

Ibrayev, Niyazbek — Doctor of physical and mathematical sciences, Professor, Director, Institute of Molecular Nanophotonics, Karaganda Buketov University, Karaganda, Kazakhstan; e-mail: niazibrayev@mail.ru; ORCID ID: https://orcid.org/0000-0002-5156-5015;

Strekal, Natalia — Doctor of physical and mathematical sciences, Professor, Department of General Physics, Yanka Kupala State University of Grodno, Grodno, Belarus; e-mail: nat@grsu.by; ORCID ID: https://orcid.org/0000-0001-6560-3679.

Article

Received: 05.12.2024
Accepted: 19.02.2024

UDC: 533.9.01

https://doi.org/10.31489/2024PH2/19-26

T. Koshtybayev[1], M. Aliyeva[2*]

[1]*Kazakh National Women's Pedagogical University, Almaty, Kazakhstan;*
[2]*Abai Kazakh National Pedagogical University, Almaty, Kazakhstan*
[*]*(Corresponding author's e-mail: moldir-2008@mail.ru)*

To plasma electrons motion theory in high-frequency fields

The article is dedicated to the kinetic theory of plasma, where the problem of interaction of high-frequency electric fields with weakly non-uniform plasma is investigated using kinetic equations with binary collision integrals for plasma particles. A new methodology for determining the expression of the averaged high-frequency pressure force is proposed based on solving the kinetic equation and using the method of successive approximations (separation of slow motions and fast oscillations) under the limiting conditions. An expression for the averaged quasi-potential force is derived based on the kinetic equation for the electron distribution function in weakly inhomogeneous magnetoactive plasma, taking into account electrons collisions with fixed ions and the presence of a longitudinally inhomogeneous high-frequency electric field using well-known methods of theoretical and mathematical physics, such as successive approximations, averaging over the effective field oscillation period, and integration over trajectories. The amplitude of the field is a slowly varying function in both time and space coordinates. The obtained expression allows us to estimate the influence of collisions of plasma particles on the Miller force, and under limiting conditions it coincides with the known expressions for the high-frequency pressure force derived from the equation of plasma electrons motion in high-frequency fields. In all calculations, the contribution of the magnetic component of the electromagnetic field is neglected, which is quite justified for the longitudinal electric field.

Keywords: weakly inhomogeneous plasma, plasma electrons, kinetic equation, averaged force, electricfield, particle collisions, fixed ions, high frequency.

Introduction

The heightened interest shown by scientists in plasma physics over the last quarter-century is primarily due to space exploration and the prospect of obtaining controlled thermonuclear reactions. Among other fields of application, it is worth mentioning plasma accelerators and generators, gas-discharge devices, plasma electronics, etc. Just from this list, it is evident that the plasma under scrutiny by researchers exhibits a tremendous diversity of numerical parameters, sometimes differing by many orders of magnitude.

It is difficult to imagine laboratory plasma without external fields. The existence of powerful sources of monochromatic electromagnetic radiation in various frequency ranges has stimulated the publication of a large number of studies on the interaction of such radiation with matter. In particular, the interaction of intense electromagnetic waves with magnetically active plasma is of interest due to solving a number of issues arising in the fusion programme development process, the study of nonlinear properties of the ionosphere with both given and artificially created inhomogeneity. The peculiar properties plasma appears very clearly when its behaviour under the influence of an electric field of high frequency is examined. Studies of the interaction of charged plasma particles with high-frequency fields have recently gained particular relevance addressing issues related to plasma heating and confinement, nonlinear wave evolution in laboratory and space plasmas, the development of charged particle acceleration methods, exploration of new wave generation and transformation techniques, and more. The initial studies in the late 1950s on the interaction of charged plasma particles with inhomogeneous high-frequency fields revealed the existence of the Miller quasi-potential force and led to ideas for high-frequency plasma confinement and acceleration [1–7]. The averaged effect of high-frequency fields on the plasma has been studied by many authors. At the same time, the theoretical description of the particle motion was based on simple physical grounds on the possibility of separation of slow motions and fast oscillations under compliance with a number of limiting conditions (nonrelativistic approximation stationary and homogeneous external magnetic field, homogeneous plasma, high-frequency fields in the quasi-stationary approximation or in the form of plane waves, etc.). Along with this, there is a significant interest in moving beyond the dipole approximation and studying a spatially inhomoge-

neous system of charged particles in inhomogeneous alternating fields. All this indicates the relevance of the study of plasma behaviour in high-frequency fields.

In the works of a number of authors [2–4] devoted to the acceleration of plasma particles and the retention of high-temperature plasma by high-frequency electromagnetic fields, an expression for the force in question was determined based on the equation of electron motion. In this paper, the expression for the Miller force is derived from the kinetic equation for the electron distribution function, which takes into account collisions of electrons with ions and the influence of a longitudinal, high-frequency and inhomogeneous electric field on a weakly inhomogeneous magnetoactive plasma, using the method of successive approximations (separation of slow movements and fast oscillations).

Experimental

Plasma can be considered as an ideal system where particles interact only in collisions. In this case collisions of plasma particles are considered as a correction leading to slow dissipation of energy, concentrated in collective degrees of freedom. Developing a consistent collision theory in plasma encounters significant difficulties associated with the slow decrease of Coulomb forces with increasing distance between interacting particles. At any given time, each charged plasma particle is exposed to a huge number of surrounding particles, and all of these effects shall be somehow taken into account. Instead of a simple two-body problem, we face the challenging problem of many-body interactions. In a strict formulation such a problem is hardly solvable. To make a solution possible, it is necessary to introduce some simplifications. The simplest is the pair collision approximation, in which the plasma particle interactions are reduced to independent and instantaneous interactions of pairs of particles.

Results and Discussion

It is known that in high-frequency electromagnetic fields, particles (specifically, electrons) experience not only the generalized Lorentz force $\vec{F}_0$ but also an additional force $\vec{f}_M$ determined by the high-frequency quasi-potential U_e, i.e., $\vec{f}_M = -n_e grad_{\vec{r}} U_e$ where n_e is the electron concentration. As a result of its action, the plasma electrons tend to move to the field minimum. The physics of such a phenomenon can be explained as follows. The electromagnetic field, causing high-frequency oscillations of electrons with velocity $\vec{\upsilon}_e$ creates as if an additional high-frequency pressure $P_{hf} \square n_e m_e \upsilon_e^2$ (or $P_{hf} \sim n_e U_e$, where m_e is the electron mass), as a result of which the plasma electrons are displaced from the areas occupied by the field. In oscillatory motion, the force $\vec{f}_M = -grad_{\vec{r}} P_{hf}$ is directed against the displacement of electrons, so when an electron is displaced to the right, a return force of greater magnitude acts on it compared to when it is displaced to the left. The averaged force $\vec{f}_M$, so called the high-frequency pressure force, or sometimes the quasi-potential Miller force, do not depend on the particle charge sign. An expression for the studied force, based on the equation of motion of electrons, was defined in the works of a number of authors [8–12], devoted to the acceleration of plasma particles and the confinement of high-temperature plasma by high-frequency electromagnetic fields. In this article, the expression for the Miller force is derived from the kinetic equation for the electron distribution function, considering electron-ion collisions and the influence of a longitudinal, high-frequency electric field

$$\vec{E} = \vec{E}_0\left(\varepsilon\vec{r}, \varepsilon t\right)\sin\omega_0 t \tag{1}$$

on weakly inhomogeneous magnetically active plasma, using the method of successive approximations (separation of slow motions and fast oscillations), where $\vec{E}_0$ the amplitude of the field is a slowly varying function in both time t and space coordinates $\vec{r}$. The parameter ε, characterising the slowness of change $\vec{E}_0$, fulfils the condition $\varepsilon = \left(V_T / \omega_0 L\right) << 1$, where V_T — thermal velocity of electrons; ω_0 — frequency, L — typical value of the change in the electron distribution function F_e (or typical size of the area occupied by the plasma). When referring to high field frequencies, we will assume that during the period of field oscilla-

tion $T = 2\pi / \omega_0$ the electron goes a distance l_{ω_0} much shorter than the free path length l, i.e., $l_{\omega_0} < l < L$ and hence it can be considered as moving in an almost homogeneous field. Here $l_{\omega_0} = V_T \omega_0^{-1}$ and $l = V_T \nu_{ei}^{-1}$; ν_{ei} is the frequency of electron-ion collisions. We will assume that the plasma

- is weakly inhomogeneous, i.e., the functions F_e and $\vec{E}$ do not change much at a distance of the Debye radius r_d or the condition $\left(L / \upsilon_0 T\right) >> 1$ is fulfilled, where υ_0 is the average particle velocity;
- fully ionised, i.e., $\gamma \to \infty$, where γ is the degree of ionisation;
- strongly discharged, i.e.,

$$\frac{\nu_{ei}}{\omega_0} < \varepsilon \text{ or } \omega_0 >> \nu_{ei} \qquad (*).$$

$$l >> \left(m_e V_T^{\,2} / eE\right). \qquad (**)$$

In addition, we will assume that:

- the activity of the electric field on the length l is greater than the energy of thermal motion kT_e (strong field condition), i.e. $eEl / k_B T_e >> 1$;
- due to the smallness of the ratio $\left(m_e / m_i\right) << 1$ (or $m_i = \infty$) we can assume that the ions are fixed, where e — electron charge; m_i — ion mass, k — Boltzmann constant; T_e — electron temperature. It should be noted that due to the field's longitudinally $\vec{E}$, the magnetic component of the electromagnetic field can be neglected, which gives significant simplifications of a computational nature, and the collisions of electrons among themselves are also neglected.

The kinetic equation for F_e, taking into account collisions of electrons with ions and fields (1), is written in the form

$$\hat{L}_0 F_e + \vec{\upsilon} \frac{\partial F_e}{\partial \vec{r}} = St_{ei}(F_e), \qquad (2)$$

where $\vec{\upsilon} = \vec{p}/m_e$ is the electron velocity;

$$\hat{L}_0 = \frac{\partial}{\partial t} - e\vec{E} \frac{\partial}{\partial \vec{p}}.$$

In accordance with (1) the function F_e depends on both fast and slow variables, i.e. $F_e = F_e\left(t, \vec{p}, \varepsilon t, \varepsilon \vec{r}\right)$. In this connection, using the method of successive approximations, we can write:

$$\begin{aligned} &\frac{\partial F_e}{\partial t} \to \left(\frac{\partial F_e}{\partial t} + \varepsilon \frac{\partial F_e}{\partial \varepsilon t} \right); \\ &\frac{\partial F_e}{\partial \vec{r}} \to \varepsilon \frac{\partial F_e}{\partial \varepsilon \vec{r}}, \end{aligned} \qquad (3)$$

and also

$$F_e = F_e^{\,0} + \varepsilon F_e^{\,1}, \qquad (4)$$

where $F_e^{\,1}$ is the fast-variable part, $F_e^{\,0}$ is the stationary (slowly changing) part of the distribution function.

Substituting expressions (3) and (4) into (2), then equating terms at the same degrees of the parameter ε, we obtain the following two equations of zero and first approximations

$$\begin{cases} \hat{L}_0 F_e^{\,0} = St_{ei}\left(F_e^{\,0}\right) & (5) \\ \hat{L}_0 F_e^{\,0} = -\hat{L}_1 F_e^{\,0} & (6) \end{cases},$$

where

$$\hat{L}_1 = \frac{\partial}{\partial \varepsilon t} + \vec{\upsilon}\frac{\partial}{\varepsilon \vec{r}}.$$

Considering the obtained system of equations, it is seen that the left part of the subsequent equation is determined by the solution of the previous equation and can be considered to be known. The integral of collisions of electrons with ions in (5) is defined by the expression [13-14]:

$$St_{ei}\left(F_e^{\,0}\right) = \frac{3\sqrt{\pi}}{8\tau_{ei}} \frac{\left(kT_e / m_e\right)^{3/2}}{\upsilon_e^{\,2}} \frac{\partial F_e^{\,0}}{\partial \upsilon_e}, \tag{7}$$

where $\tau_{ei} \square 1/\nu_{ei}^{\,-1}$ — characteristic time of collisions of electrons with ions:

$$\tau_{ei} = \frac{3\sqrt{m_e}\left(kT_e\right)^{3/2}}{4\sqrt{2\pi}\Lambda e^2 e_i^{\,2} n_i}.$$

Λ Coulomb logarithm; e_i and n_i — charge and ion concentration, respectively. It should be noted that in (7) the terms of order $\left(m_e / m_i\right)$ are neglected. After substituting instead of $F_e^{\,0}$ in expression (7), the solution

$$F_e^{\,0(0)} = n_e\left(2\pi m_e kT_e\right)^{-3/2} \exp\left\{-\left(2m_e kT_e\right)^{-1}\left(\vec{p} - e\omega_0^{\,-1}\vec{E}_0 \cos\omega_0 t\right)^2\right\},$$

of the homogeneous equation $\hat{L}_0 F_e^{\,0(0)} = 0$, we have

$$\begin{aligned} \hat{L}_0 F_e^{\,0} = \Gamma = n_e\left(2\pi m_e kT_e\right)^{-3/2} \frac{4\pi\Lambda e^2 e_i^{\,2} n_i}{\left(\upsilon_e m_e\right)^3 kT_e} \vec{p}\left(\vec{p} - e\omega_0^{\,-1}\vec{E}_0 \cos\omega_0 t\right)\times \\ \times \exp\left\{-\left(2m_e kT_e\right)^{-1}\left(\vec{p} - e\omega_0^{\,-1}\vec{E}_0 \cos\omega_0 t\right)^2\right\}. \end{aligned} \tag{5A}$$

The general solution of this equation can be represented as

$$F_e^{\,0} = F_e^{\,0(0)} + F_e^{\,0(1)}, \tag{5B}$$

where $F_e^{\,0(1)}$ is the solution of the inhomogeneous equation. The first approximation equations (6) can be rewritten in the form

$$\hat{L}_0 F_e^{\,1} = -G\left(t, \vec{p}, \varepsilon t, \varepsilon \vec{r}\right), \tag{6A}$$

where $G = \hat{L}_1 F_e^{\,0}$. The solution $F_e^{\,1(0)}$ of the homogeneous equation $\hat{L}_0 F_e^{\,1(0)} = 0$ is the expression for $F_e^{\,0(0)}$, and the general solution of (6A) is of the form:

$$F_e^1 = F_e^{1(0)} + F_e^{1(1)}, \tag{8}$$

where $F_e^{1(1)}$ is the solution of the inhomogeneous equation. In order to find the solutions $F_e^{1(1)}$ and $F_e^{0(1)}$ let's write down the characteristics of the homogeneous equation (2), i.e.

$$\frac{d\vec{p}}{dt} = -e\vec{E}; \qquad m_e \frac{d\vec{r}}{dt} = \vec{p}, \tag{9}$$

solutions ща which are the values of impulses $\vec{p}$ and coordinates $\vec{r}$ at time instant t; they are related to the values $\vec{P}_0$ and $\vec{R}$ at the initial time instant t as follows [15–18]:

$$\vec{P}_0\left(t', t, \vec{p}, \varepsilon t, \varepsilon\vec{r}\right) \equiv \vec{p} + \frac{e\vec{E}_0}{\omega_0}\left\{1 - \cos\omega_0\left(t - t'\right)\right\};$$

$$\vec{R}\left(t', t, \vec{P}_0, \vec{r}, \varepsilon t, \varepsilon\vec{r}\right) \equiv \vec{r} - \frac{\vec{P}_0}{m_e}\left(t - t'\right) - \frac{e\vec{E}_0}{m_e\omega_0}\left\{\omega_0^{-1}\sin\omega_0\left(t - t'\right) - \left(t - t'\right)\right\}.$$

Moving from $\vec{p}$ to $\vec{P}_0$ and from $\vec{r}$ to $\vec{R}$, he required solutions are determined [9; 10]:

$$F_e^{1(1)}\left(t, \vec{P}_0, \varepsilon t, \varepsilon\vec{R}\right) = -\int_0^t G\left(t - t', \varepsilon t, \varepsilon\vec{R}, \vec{P}_0\right)dt'. \tag{10}$$

$$F_e^{0(1)}\left(t, \vec{P}_0\right) = \int_0^t \Gamma\left(t - t', \vec{P}_0\right)dt'. \tag{10A}$$

Hence, the general solution of equation (2), according to (4), (5B) and (8) will be as follows

$$F_e = F_e^{0(0)} + \int_0^t \Gamma dt' + \varepsilon\left(F_e^{1(0)} - \int_0^t G dt'\right). \tag{11}$$

Note that when integrating the integrand exponential functions Γ and G, in (10) the condition $\left(eE_0 / \omega_0 P_0\right) < 1$ was taken into account, using which these functions were expanded into a series. At the same time, only terms were considered in the expansion □ $E_0^{\,2}$.

Oscillatory components in (11) can be eliminated by averaging this relation over T. The operator of averaging the function F_e will be denoted by the symbol $\langle\ \rangle$:

$$\left\langle F_e \right\rangle = T^{-1}\int_0^T F_e dt. \tag{11A}$$

Representing the solution in this form involves constructing the first approximation, the so-called averaging method, which has found wide application in nonlinear physics tasks [19–21].

Finally, integrating the product of $T^{-1}\vec{P}_0\left\langle F_e\right\rangle$ over $\vec{P}_0$ in the limit from $-\infty$ to $+\infty$, we obtain the final expressions for the force $\vec{f}_M$:

$$\vec{f}_M = -\frac{3}{2}\frac{n_e e^2 \vec{E}_0}{m_e \omega_0^2}\frac{\partial \vec{E}_0}{\partial \varepsilon \vec{R}}\left\{1-0,5\left(\frac{\nu_{ei}}{\omega_0}\right)^2\right\}, \quad (12)$$

or

$$\vec{f}_M = -\frac{3}{2} n_e \frac{\partial U_e}{\partial \varepsilon \vec{R}}\left\{1-0,5\left(\frac{\nu_{ei}}{\omega_0}\right)^2\right\},$$

and

$$U_e = -\frac{1}{2m_e}\left(\frac{e\vec{E}_0}{\omega_0}\right)^2.$$

Under condition (*), from (12) follows the expression [11–13]:

$$\vec{f}_M = -\frac{3n_e e^2 \vec{E}_0}{2m_e \omega_0^2}\frac{\partial \vec{E}_0}{\partial \varepsilon \vec{R}}.$$

The obtained result coincides, up to a constant, with known expressions for the Miller force, and is also of theoretical interest and reveals the picture of the interaction of a weakly inhomogeneous plasma with a high-frequency electric field. However, the approximate solution (11) allows estimating the influence of electron-ion collisions on the high-frequency pressure forceand can be used in constructing the kinetic theory of inhomogeneous plasma located in high-frequency electromagnetic fields. In all calculations, the contribution of the magnetic component of the electromagnetic field is neglected, which is quite true for the longitudinal electric field, and well-known methods of theoretical and mathematical physics are used, such as averaging over the period of oscillation of the electric field and integration along trajectories.

Conclusions

Therefore, in the article a new methodology has been proposed for determining the expression of the averaged high-frequency pressure force. It is based on solving the kinetic equation with the collision integral of plasma particles and the method of successive approximations, while adhering to a number of limiting conditions (weakly inhomogeneous and fully ionized plasma, longitudinal and inhomogeneous high-frequency electric field, nonrelativistic approximation, as well as fixed ions approximations, strong electric field, and pair collisions between particles). The effects of the weak inhomogeneity of the plasma and the external field on particle collisions and the Miller force are estimated. The motion of charged particles in an electric field is considered on the basis of representations of classical physics and these representations retain their force not only when analyzing the movements of charged particles under the action of macroscopic external fields, but form the foundation necessary for understanding the processes of particle interaction in plasma–processes involving microscopic fields of individual particles.

References

1 Veksler, V.I., & Kovrizhnykh, L.M. (1958). Cyclical Acceleration of Particles in High-Frequency Fields. *Journal of Experimental and Theoretical Physics*, *5*(11), 1116–1118.

2 Miller, M.A. (1958). Motion of Charged Particles in High-Frequency Electromagnetic Fields. *Radio-physics and Quantum Electronics series*, 3, 110–123.

3 Gaponov, A.V., & Miller, M.A. (1958). On Potential Wells for Charged Particles in a High-Frequency Electromagnetic Field.*Journal of Experimental and Theoretical Physics*, 1, 242–243.

4 Morozov, A.I., & Solovyev, L.S. (1963). Motion of Charged Particles in a High-Frequency Electromagnetic Field. *Plasma Theory*, 2, 214–218.

5 Kulumbayev, E.B., & Nikulicheva, T.B. (2012). Interaction of plasma jets in a two-jet electric arc. *High Temperature*, 4, 483–490. https://doi.org/10.1134/S0018151X12040141 https://www.mathnet.ru/rus/tvt/v50/i4/p483

6 Olevanov, M.A., Mankelevich, Yu.A., & Rakhimova, T.B. (2003). On The Effect of Dust Particles on The Properties of Low-Temperature Plasma. *Journal of Experimental and Theoretical Physics*, 3, 503–517.

7 Vysikaylo, F.I. (2004). Accumulation of an Electric Field in Dissipative Structures in a Gas-Discharge Plasma. *Journal of Experimental and Theoretical Physics*, 5, 1071–1081.

8 Gildenburg, V.B. (1964). On nonlinear effects in inhomogeneous plasma. *Journal of Experimental and Theoretical Physics*, 6, 2156–2164.

9 Artsimovich, L.A. (1978). Motion of charged particles in electric and magnetic fields. *Science*, 224.

10 Matveyev, A.I. (2008). Evolution of the Langmuir Wave in a Weakly Homogeneous Plasma with a Longitudinal Electric Field. *Plasma Physics*, 2, 114–121.

11 Artsimovich, L.A., & Sagdeyev, R.Z. (1979). Plasma Physics for Physicists. *Publishing House of Literature in the field of Atomic Science and Technology*, 317.

12 Kosarev, I.N. (2006). Kinetic theory of plasmas and gases. Interaction of high-intensity laser pulses with plasmas. *Achievements of the physical sciences*, 49, 1239–1252. DOI: 10.1070/PU2006v049n12ABEH006027

13 Klimontovich, Yu.L. (1964). Statistical theory of nonequilibrium processes in plasma. *Publishing House of Moscow State University*, 281.

14 Magee, R.M., Galante, M.E., Gulbrandsen, N., McCarren, D.W. & Scime, E.E. (2012). Direct measurments of the ionization profile in krypton helicon plasmas. *Physics of Plasmas*, 19, 123506. https://doi.org/10.1063/1.4772060

15 Charles, C., Boswell, R.W., Laine, R. & MacLellan, P. (2008). An experimental investigation of alternative propellants for the helicon. *Journal of Physics D: Applied Physics*, 6, 175213. DOI 10.1088/0022-3727/41/17/175213

16 Lafleur, T., Charles, C., & Boswell, R.W. (2009). Detailed plasma potential measurements in a radio-frequency expanding plasma obtained from various electrostatic probes. *Physics of Plasmas*, 16, 044510. DOI: 10.1063/1.3125314

17 Anisimov, I.A., & Litoshenko, T.E. (2008). Interaction of a Modulated Electron Beam with an Inhomogeneous Plasma: Two-Dimensional Electrostatic Modeling. *Physics of Plasmas*, 10, 918–925.

18 Repin, A.Yu., Stupicki, E.L. & Shapranov, A.V. (2004). Dynamics and interaction with the barrier of a toroidal plasma clot. Ionization-dynamic characteristics and electromagnetic radiation. *High Temperature*, 4, 523–538. https://www.mathnet.ru/rus/tvt/v42/i4/p523

19 Lafleur, T., Boswell R.W., & Charles, C. (2010). Ion beam formation in a very low magnetic field expanding helicon discharge. *Physics of Plasmas*, 17, 043505.https://doi.org/10.1063/1.3381093

20 Shaihitdinov, R.Z. (2014). The Mechanism of Attraction of Negatively Charged Macroparticles in Dusty Plasma. *Low-Temperature Plasma in Functional Coating Processes*, 5, 168–171.

21 Kralkina, E.A., Neklyudova, P.A., Pavlov, V.B., Vavilin, K.V., & Tarakanov, V.P. (2014). Radial inhomogenity of plasma parameters in a low-pressure inductive RF discharge. *Bulletin of Moscow. University Physics Astronomy*, 1, 79.

Т. Қоштыбаев, М. Алиева

Плазмадағы электрондардың жоғарыжиілікті өрістердегі қозғалыс теориясына

Мақала плазманың кинетикалық теориясына арналған және жоғарыжиілікті электр өрісінің әлсіз біртексіз плазмаға әсері туралы мәселе плазма бөлшектері арасындағы жұптық әсерлесу интегралы бар кинетикалық теңдеуді қолдану арқылы шешілген. Белгілі бір шектеу шарттары орындалған жағдай үшін орташаланған жоғарыжиілікті қысым күшін табудың жаңа әдістемесі ұсынылған және ол кинетикалық теңдеуді шешуге, кезектестік жуықтау тәсіліне негізделген. Соңғы айтылған тәсілде баяу қозғалыстар мен шапшаң тербелістерді бөліп қарастырған. Әлсіз біртексіз, әрі магнитті-белсенді плазмадағы бөлшектердің үлестірім функциясына арналған кинетикалық теңдеуді шешу арқылы орташаланған квазипотенциалды күштің өрнегі қорытылып шығарылды. Қолданылған кинетикалық теңдеу электрондардың қозғалмайтын иондармен соқтығысуын және жоғарыжиілікті бойлық-біртексіз электр өрісінің әсерін ескереді. Сонымен бірге, күштің өрнегін шығару барысында теориялық және математикалық физиканың белгілі тәсілдері қолданылды, атап айтқанда: кезектестік жуықтау тәсілі, сыртқы өрістің тербеліс периоды бойынша орташалау тәсілі және траектория бойынша интегралдау тәсілі. Өрістің амплитудасы уақыт пен координатаға тәуелді баяу өзгермелі функция болып табылады. Алынған өрнек плазма бөлшектерінің соқтығысуларының Миллер күшіне ықпалын бағалауға мүмкіндік жасайды және шектеу шарттары орындалған кезде электрондардың жоғарыжиілікті өрістердегі қозғалыс теңдеуінен алынған жоғарыжиілікті қысым күшінің өрнегімен белгілі бір тұрақтыға дейінгі дәлдікпен сәйкес келеді. Жүргізілген барлық есептеулер кезінде электромагниттік өрістің магниттік құраушысы ескерілмеді және бұл жағдай бойлық электр өрісіне тура болады.

Кілт сөздер: әлсіз біртексіз плазма, плазмалық электрондар, кинетикалық теңдеу, орташаланған күш, электр өрісі, бөлшектердің соқтығысуы, қозғалмайтын иондар, жоғарыжиілік.

Т. Коштыбаев, М. Алиева

К теории движения плазменных электронов в высокочастотных полях

Статья посвящена кинетической теории плазмы, и в ней исследована проблема взаимодействия электрического поля высокой частоты со слабо неоднородной плазмой методом кинетических уравнений с интегралами парных столкновений частиц плазмы. Предложена новая методика определения выражения усредненной силы высокочастотного давления, основанная на решении кинетического уравнения и методе последовательных приближений (разделение медленных движений и быстрых осцилляций) при соблюдении ограничительных условий. Выведено выражение для усредненной квазипотенциальной силы на основе кинетического уравнения для функции распределения электронов слабо неоднородной магнитоактивной плазмы, учитывающей столкновение электронов с неподвижными ионами и наличие продольно-неоднородного электрического поля высокой частоты с использованием общеизвестных методов теоретической и математической физики, таких как последовательные приближения, усреднения по периоду колебания действующего поля и интегрирования по траекториям. Амплитуда поля является медленно меняющейся функцией по времени и координатам. Полученное выражение позволяет оценить влияние столкновений плазменных частиц на силу Миллера, и при ограничительных условий оно совпадает с точностью до постоянной с известными выражениями для силы высокочастотного давления, рассчитанного на основе уравнения движения электронов плазмы в высокочастотных полях. Во всех вычислениях не учитывается вклад магнитной составляющей электромагнитного поля, что вполне справедливо для продольного электрического поля.

Ключевые слова: слабо неоднородная плазма, плазменные электроны, кинетическое уравнение, усредненная сила, электрическое поле, столкновение частиц, неподвижные ионы, высокая частота.

Information about authors

Koshtybayev, Talgat — Candidate of physical and mathematical sciences, Associate Professor, Department of Physics, Kazakh National Women's Teacher Training University, Almaty, Kazakhstan; e-mail: koshtybayev70@mail.ru; ORCID ID: https://orcid.org/0009-0004-7344-6801;

Aliyeva, Moldir — Master of sciences, Senior lecturer, Department of Physics, Abai Kazakh National Pedagogical University, Almaty, Kazakhstan; e-mail: moldir-2008@mail.ru; ORCID ID: https://orcid.org/0000-0003-0440-6211.

Article

Received: 11.12.2023
Accepted: 06.02.2024

UDC 621.793

https://doi.org/10.31489/2024PH2/27-35

Zh.B. Sagdoldina[1], B.K. Rakhadilov[2], D.B. Buitkenov[1], L.G. Sulyubayeva[1], A.B. Nabioldina[1*], N.S. Raisov[1], S.D. Bolatov[1]

[1]Research Center Surface Engineering and Tribology, Sarsen Amanzholov East Kazakhstan University, Ust-Kamenogorsk, Kazakhstan;
[2]PlasmaScience LLP, Ust-Kamenogorsk, Kazakhstan
[*](Corresponding author's e-mail: anabioldina@gmail.com)

Investigation of the structural and phase state of detonation multilayer coatings based on NiCr/NiCr–Al_2O_3/Al_2O_3 during high-temperature oxidation

This paper presents a study of the structural and phase state of detonation multilayer coatings under high-temperature oxidation. The experiment aimed to find out the effect of high temperatures on the structural-phase state of coatings and their effectiveness in preventing oxidative processes. As a result of the research, it was found that after high-temperature tests, protective phases such as $NiCr_2O_4$, Al_2O_3, and Cr_2O_3 are formed in the structure of multilayer coatings. These phases were identified to play a key role in preventing intensive oxidation of the metal surface. It was determined that $NiCr_2O_4$ provides stability to the metal layer, and Al_2O_3 and Cr_2O_3 are effective barriers protecting the surface from aggressive environmental influences. It is important to note that no signs of fracture or detachment were found in the multilayer coatings during the entire experiment. After the first cycle, the uncoated sample experienced peeling of its oxide film, resulting in a significant loss of mass. It was determined that the uncoated steel experiences significantly higher mass loss, indicating a faster formation of oxides on its surface. The experimental data confirm the effectiveness of coatings in protecting against oxidative processes at high temperatures, thereby maintaining the stability and durability of the material under extreme thermal influences.

Keywords: detonation spraying, structure, phase composition, high-temperature oxidation, multilayer coatings.

Introduction

In modern industry, where components are exposed to harsh operating conditions, including high-temperature gas flows, aggressive chemical environments and abrasive particles, the issue of improving the wear resistance, heat resistance and corrosion resistance of material surfaces is becoming increasingly important [1-2]. To effectively solve this problem, the use of multilayer gradient coatings is recommended, which in recent decades have successfully found application in various industries such as power engineering and mechanical engineering [3-4].

Multilayer gradient coatings provide reliable protection of surfaces against wear, corrosion and oxidation, increasing the durability and performance of parts and reducing maintenance costs [5-6]. Their uniqueness lies in their ability to combine different material characteristics in a single coating due to smoothly varying composition along the thickness. Compositions consisting of metal-ceramic layers with a uniformly distributed oxide component in them are the most promising for harsh operating conditions. Recent research has led to multilayer gradient coatings combining nickel chromium (NiCr) and aluminum oxide (Al_2O_3), which showed outstanding properties and provided unique advantages over conventional homogeneous coatings [7–9]. Al_2O_3 stands out for its abrasion and corrosion resistance, excellent dielectric resistance and thermal shock resistance. These characteristics make Al_2O_3 coatings particularly attractive for surface protection of metal components that are exposed to harsh environments [9]. Scientific studies emphasize the importance of proper chemical composition selection in the interface between the substrate and the coating to ensure high corrosion resistance, indicating that the boundaries between layers can act as effective protective barriers in aggressive environments [10–14]. Studies [15] have confirmed that the use of nickel chromium as the bottom metal layer in multilayer coatings helps to improve the thermal resistance of oxide coatings. This is due to improved adhesion strength and equalization of the difference in thermal expansion coefficients between the metal sample and the coating. This combination minimizes the stresses generated during thermal cycling and therefore reduces the likelihood of coating failure.

Under conditions of cyclic oxidation and high temperatures, a special approach is required to protect surfaces from aggressive environments. There are many coating methods available, and the selection of an

appropriate method plays a key role in ensuring the durability and effectiveness of the protection. From the analysis of literature studies, it is revealed that detonation sputtering is a promising technology for NiCr-Al_2O_3-based multilayer gradient coatings [16–19]. This method provides high sputtering speed and is capable of producing high density coatings, minimizing the formation of pores and defects in the coating structure. This approach can provide reduced porosity and increased corrosion resistance, which is critical in corrosive environments. Nevertheless, not all multilayer gradient coatings exhibit resistance to high temperatures under real operating conditions. In certain instances, structural degradation occurs due to exposure to high temperatures and cyclic thermal loads, potentially resulting in a loss of effectiveness of protective properties. Hence, to achieve maximum efficiency and durability of multilayer gradient coatings, it is crucial to conduct research focused on optimizing their chemical composition, structure, and application methods. This will enable us to enhance the technology for creating such coatings, rendering them more stable and effective in high temperatures and aggressive environments.

Hence, the purpose of our study is to investigate the structural and phase states of detonation multilayer coatings under conditions of high-temperature oxidation. To accomplish this objective, we intend to conduct a study on the structural and phase characteristics of multilayer coatings under high-temperature exposure.

Materials and methods of research.

NiCr, NiCr–Al_2O_3 and Al_2O_3 powders with an average size of 40–45 μm were used to apply multilayer coatings on stainless steel 12Kh18N10T samples. The sputtering was carried out using a CCDS2000 machine [13]. The use of detonation spraying technology provided an opportunity to create multilayer gradient coatings. This process allows to sequentially apply layers with changing composition, which leads to a coating with a gradual change in characteristics from layer to layer. Technological parameters of the process and the effect of detonation sputtering on the properties and phase-structural states of NiCr/NiCr–Al_2O_3/Al_2O_3-based coatings are described in detail in the scientific paper [17-18]. As a result of the positive conclusions obtained in previous studies [11, 17], further high-temperature tests were carried out exclusively on samples with five-layer coatings.

An X'Pert PRO X-ray diffractometer (using CuKα radiation) was used to study the structural-phase composition of the coatings. Imaging was carried out at the following parameters: tube voltage U = 40 kV; tube current I = 30 mA. The obtained diffractograms were decoded using the HighScore program. Investigations of surface microstructure and morphology of coating cross-section were carried out by scanning electron microscopy (SEM) on MIRA3 (Tescan, Czech Republic) with energy dispersive analysis attachment INCA ENERGY (“Oxford Instruments”, Great Britain) in the laboratory of Karaganda Buketov University.

Experiments on high-temperature oxidation were carried out at a temperature of 1100 °C using a muffle electric furnace model SNOL 3/1100. All tests were performed in accordance with GOST 6130-71 “Metals. Methods of determination of heat resistance”. This standard establishes a methodology for evaluating the resistance of metals to high temperatures. In this test, 50 cycles were performed, and each cycle included one hour of heating to 1100 °C, followed by a 20-minute cooling to room temperature. To assess the extent of corrosion, samples were periodically removed from the crucible and weighed on analytical scales to the nearest 0.1 mg to determine the change in mass. This allowed monitoring the effect of thermal cycling on the surface properties of the materials.

Results and discussion.

Two types of samples were tested to assess oxidation resistance: uncoated steel 12X18H10T and a multilayer coating based on NiCr/NiCr–Al_2O_3/Al_2O_3. The coatings were uniformly applied to all six sides of the samples to ensure uniformity and minimize measurement errors. Figure 1 shows the samples before and after the high-temperature oxidation tests.

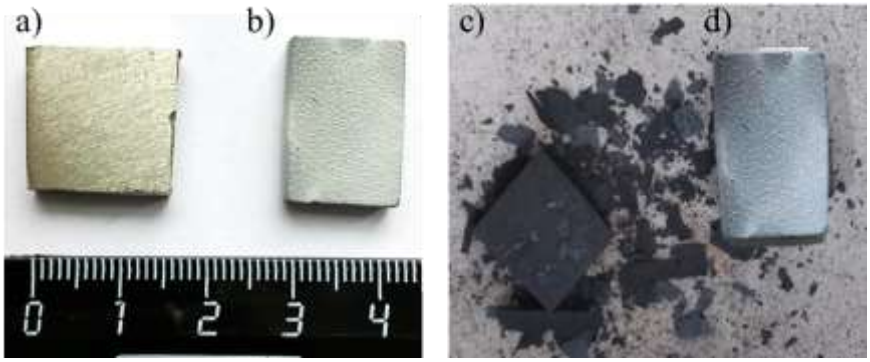

Figure 1. Samples before (a, b) and after (c, d) high-temperature oxidation tests

a-c) 12Kh18H10T steel; b-d) NiCr/NiCr–Al_2O_3/Al_2O_3 multilayer coating

Figure 2 shows the value of mass change of the samples after 50 cycles of high temperature oxidation test. The results indicated that the coated samples exhibited superior performance, whereas the uncoated samples yielded the poorest results. In the uncoated steel, intense delamination of the oxide film (scale) was already observed after the first cycle (Fig. 1c), and this process increased with time. The multilayer coatings showed no signs of failure or delamination throughout the experiment. It has been determined that the uncoated steel experiences a significantly higher mass loss, indicating a faster formation of oxides on its surface. Such a significant increase in the mass loss of the original sample may be due to the destruction of the sample due to cyclic exposure to high temperatures, which is not characteristic of coated samples.

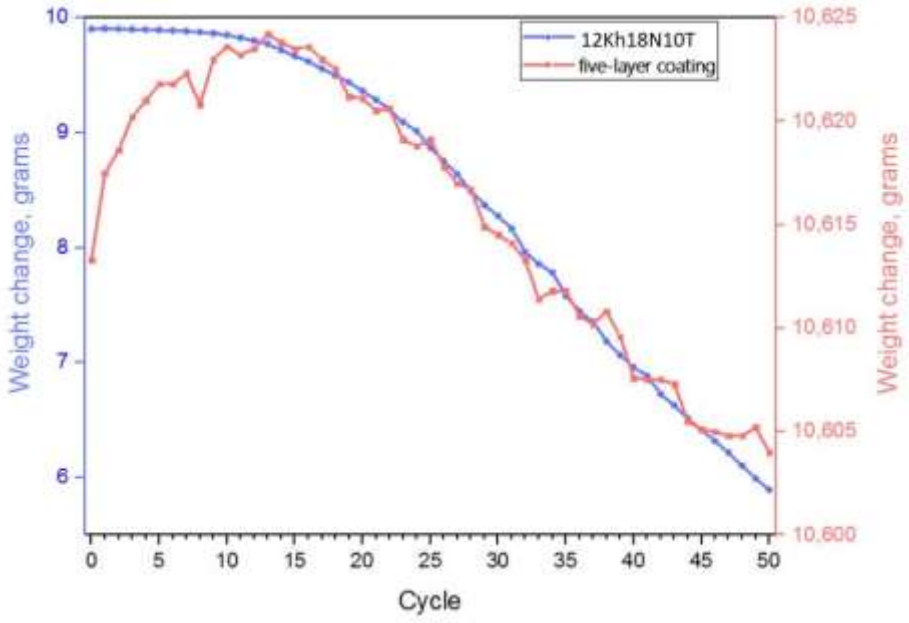

Figure 2. Weight change of uncoated steel and multilayer coating based on NiCr/NiCr–Al_2O_3/Al_2O_3 after high-temperature oxidation tests

Figure 3 shows the results of a scanning electron microscope of the cross-section of a multilayer coating NiCr/NiCr–Al_2O_3/Al_2O_3, after high-temperature tests for 50 hours at a temperature of 1100°C. After high-temperature oxidation tests, the multilayer coatings NiCr/NiCr–Al_2O_3/Al_2O_3 remain completely intact and dense. Cracks and peeling were not observed, which suggests that these multilayer coatings prevent direct contact of oxygen with the steel substrate and thus protect the steel from oxidation. The microstructure of the coating contains a significant amount of oxides and has low porosity.

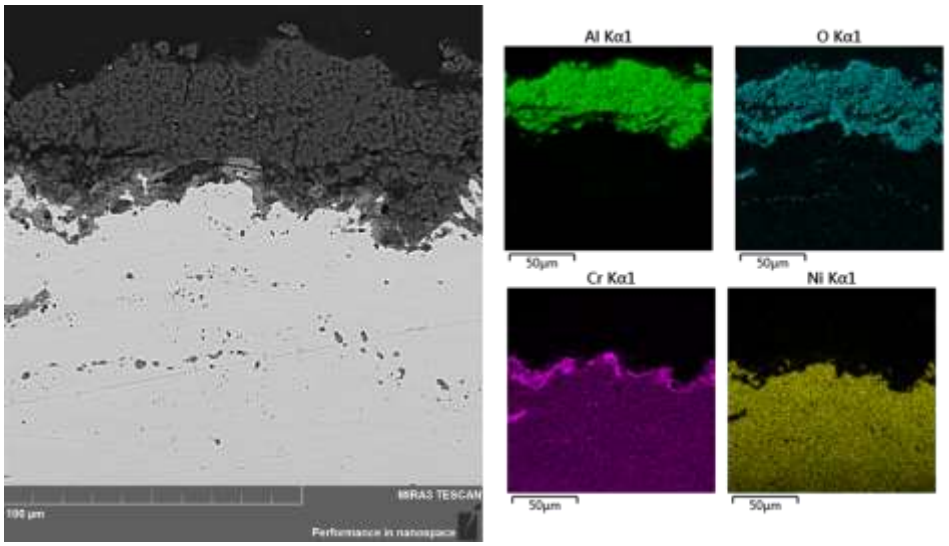

Figure 3. SEM images of cross-sectional morphology of multilayer coating after high-temperature oxidation

As a result of morphological studies of the cross-sectional structure of uncoated steel, it was found that heating to 1100 °C with prolonged holding time leads to the formation of a thin oxide layer (Fig. 4). This layer has a clear boundary with the metal, but its thickness is not uniform across the cross-section of the sample. The non-uniformity of the layer thickness across the cross-section of the sample may indicate complex oxidation processes and interaction with the environment in different parts of the material. Such morphological changes may affect the mechanical and chemical properties of the material.

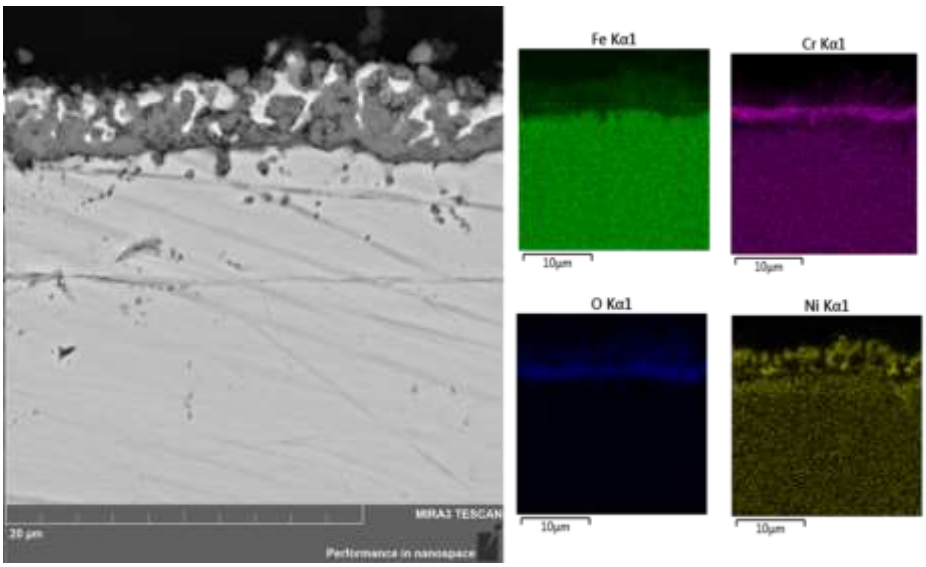

Figure 4. SEM images of cross-sectional morphology of uncoated steel after high-temperature oxidization

Figure 5 shows the X-ray images of the multilayer coatings before and after the high-temperature tests. It was found that the multilayer coatings consist of protective phases such as $NiCr_2O_4$, Al_2O_3 and Cr_2O_3 after high temperature testing. These phases play a key role in preventing intense oxidation at high temperatures. $NiCr_2O_4$ provides the stability of the metal layer, while Al_2O_3 and Cr_2O_3 are effective barriers protecting the surface from aggressive environmental influences. Prior to heat treatment, the graded five-layer coatings contain aluminum oxide phases including α- and γ-phases (Fig. 5c). Studies have shown that when heated to a temperature of 1100°C, γ-Al_2O_3 is converted to the more resistant α-Al_2O_3. This phase transition process from γ-phase to α-phase observed at high temperatures has also been reported in previous research studies [9, 20]. This phase transformation indicates the structural stability and adaptability of the coatings to changes in temperature conditions.

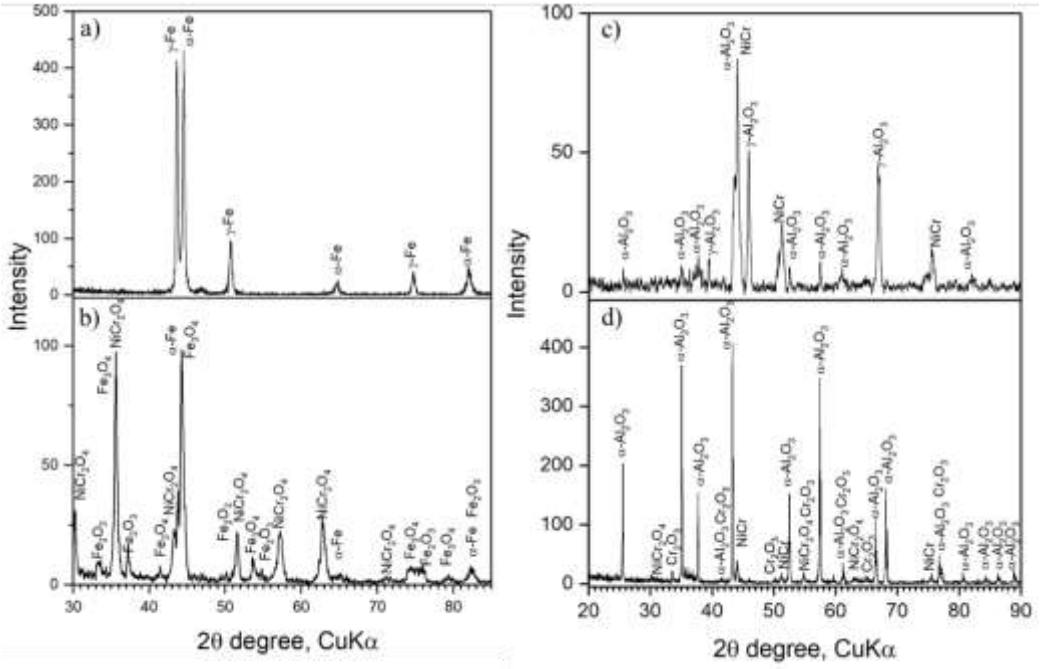

a-b) 12Kh18H10T steel; c-d) NiCr/NiCr–Al_2O_3/Al_2O_3 multilayer coating
Figure 5. Results of X-ray diffraction analysis before (a, c) and after (b, d) high temperature tests

After the experiment, uncoated steel shows the formation of different phases such as Fe_2O_3, Fe_3O_4 and $NiCr_2O_4$ (Fig. 5 b). This indicates an initiated oxidation process of the material under the influence of high temperatures. Especially interesting is the formation of $NiCr_2O_4$ spinel, which may be a consequence of high temperatures reaching 1100 °C. This process leads to the formation of a clear boundary between metal and oxide. The explanation of this effect is related to the partial dissolution of chromium carbides, which are oriented along the grain boundaries of the material.

Conclusion

Based on the conducted studies using five-layer coatings on 12Kh18N10T steel at high temperatures, the following conclusions can be made:

NiCr/NiCr–Al_2O_3/Al_2O_3 based multilayer coatings shown that the coated samples exhibit higher oxidation resistance characteristics compared to the uncoated sample. It is important to note that the multilayer coatings show no signs of failure or delamination throughout the experiment. In the uncoated sample, intense delamination of the oxide film was observed after the first cycle, resulting in significant mass loss. X-ray studies showed that the multilayer coatings contain protective phases such as $NiCr_2O_4$, Al_2O_3 and Cr_2O_3 after high temperature testing. It is found that these phases play a key role and indicates the effectiveness of these components in preventing the intense oxidation of the metal surface. It is determined that morphological changes such as non-uniformity of the oxide layer thickness can affect the mechanical properties of the material.

Thus, the experimental data confirm the effectiveness of coatings in protecting against oxidative processes at high temperatures and shows their importance in maintaining the stability and durability of the material under conditions of extreme thermal effects.

Acknowledgments

This research is funded by the Science Committee of the Ministry of Science and Higher Education of the Republic of Kazakhstan (Grant No. AP13068364).

References

1 Салахов А.М. Современные керамические материалы / А.М. Салахов // Министерство образования и науки РФ; Казанский федеральный университет. — 2016. — С. 407.

2 Okavity V.A. Paramets optimization for plasma spraying and pulsed plasma treatment of surface layers of gas-thermal composite coatings based on multifunctional oxid4 ceramics / V.A. Okavity, A.I. Shevtsov, V.V. Okavity, V.M. Astashinsky, E.A. Kostyukevich // High Temperature Material Processes. — 2014. — Vol. 18 (1-2). — P. 45–62.

3 Bassiouny S. 30 Years of functionally graded materials: An overview of manufacturing methods / S. Bassiouny, J. Jinghua, F. Reham, A. Tareq, X. Qiong, W. Lisha, S. Dan, M. Aibin // Applications and Future Challenges, Composites Part B: Engineering. — 2020. — Vol. 201. — P. 108376.

4 Sova A. Development of multimaterial coatings by cold spray and gas detonation spraying / A. Sova, D. Pervushin, I. Smurov // Surface and Coatings Technology. — 2010. — Vol. 205(4). — P. 1108–114.

5 Ozgurluak Y. Structural characteristics, oxidation performance and failure mechanism of thermal barrier coatings fabricated by atmospheric plasma spraying and detonation gun spraying / Y. Ozgurluk, A. Gulec, D. Ozkan, G. Binal, A.C. Karaoglanly // Engineering Failure Analysis. — 2023. — Vol. 152. — P. 107499.

6 Kameneva A. Corrosion, wear, and friction behavior of a number of multilayer two-, three- and multicomponent nitride coatings on different substrates, depending on the phase and elemental composition gradient / A. Kameneva, V. Kichigin // Applied Surface Science. — 2019. — Vol. 489 — P. 165–174.

7 Sathish M. A critical review on functionally graded coatings: Methods, properties, and challenges / M. Sathish, N. Radhika, S. Bassiouny // Composites Part B: Engineering — 2021. — Vol. 225. — P. 109278.

8 Maulet M. Influence of the content of aluminum on the structure of gradient detonation coatings based on NiCr-Al / M. Maulet, Zh.B. Sagdoldina, B.K. Rakhadilov, D.N. Kakimzhanov, N.M. Magazov // Bulletin of the University of Karaganda – Physics. — 2022. — Vol. 3(107). — P. 18–24. DOI: 10.31489/2022PH3/18-24

9 Vandana C.M. Strongly adherent Al_2O_3 coating on SS 316L: Optimization of plasma spray parameters and investigation of unique wear resistance behaviour under air and nitrogen environment / C.M. Vandana, Y. Chakravarthy, N. Khare, K. Singh, S. Ghorui // Ceramics International. — 2019. — Vol. 46(7). DOI: 10.1016/j.ceramint.2019.12.099

10 Rakhadilov B. Comparative study of structures and properties of detonation coatings with α-Al_2O_3 and γ-Al_2O_3 main phases / B. Rakhadilov, D. Kakimzhanov, D. Baizhan, G. Muslimanova, S. Pazylbek, L. Zhurerova // Coatings. — 2021. — Vol. 11. — P. 1566. https://doi.org/10.3390/coatings11121566.

11 Lashmi P.G. Present status and future prospects of plasma sprayed multilayered thermal barrier coating systems / P.G. Lashmi, P.V. Ananthapadmanabhan, G. Unnikrishnan, S.T. Aruna // Eur Ceram Soc. — 2020. — Vol. 40(8). — P. 2731–2745.

12 Pogrebnjak A.D. Structure and properties of Al_2O_3 and Al_2O_3+Cr_2O_3 coatings deposited to steel 3 (0.3 wt%C) substrate using pulsed detonation technology / A.D. Pogrebnjak, M. Iljashenko, O.P. Kulmenteva, V.S. Kshnajakin, A.P. Kobzev, Y.N. Tyurin, O. Kolisnichenko // Vacuum. — 2001. — Vol. 62(1). — P. 21–26.

13 Rakhadilov B. Preparation and characterization of NiCr/NiCr–Al_2O_3/ Al_2O_3 multilayer gradient coatings by gas detonation spraying / B. Rakhadilov, D. Buitkenov, Zh. Sagdoldina, Z. Idrisheva, M. Zhamanbayeva, D. Kakimzhanov // Coatings. — 2021. — Vol. 11(12). — P. 1524.

14 Sreedhar G. Hot corrosion behaviour of plasma sprayed YSZ/ Al_2O_3 dispersed NiCrAlY coatings on Inconel-718 superalloy / G. Sreedhar, MD.M. Alam, V.S. Raja // Surface & Coatings Technology — 2009. — Vol. 204. — P. 291–299.

15 Rakhadilov B.K. Structure and properties of multilayer coatings based on CoCrAlY/Al_2O_3 obtained by detonation spraying / B.K. Rakhadilov, Yu.N. Tyurin, O.V. Kolisnichenko, D.N. Kakimzhanov, L.G. Zhurerova // Eurasian Journal of Physics and Functional Materials. — 2022. — Vol. 6(3). — P. 234–243. DOI: 10.32523/ejpfm.2022060308

16 Rakhadilov B.K. Tribological and mechanical properties of gradient coating on Al_2O_3 based coating produced by detonation spraying methods / B.K. Rakhadilov, D.N. Kakimzhanov, D.B. Buitkenov, R.S. Kozhanova, L.G. Zhurerova, Zh.B. Sagdoldina // Advances in Tribology. — 2023. — P. 9. https://doi.org/10.1155/2023/1520135.

17 Rakhadilov B. Preparation and Characterization of NiCr/NiCr–Al_2O_3/ Al_2O_3 Multilayer Gradient Coatings by Gas Detonation Spraying / B. Rakhadilov, D. Buitkenov, Zh. Sagdoldina, Zh. Idrisheva, M. Zhamanbayeva, D. Kakimzhanov // Coatings. — 2021. — Vol. 11(12). — P. 1524. DOI: 10.3390/coatings11121524

18 Wang X. Manufacturing and the process-structure-property correlation of detonation sprayed iron coatings under an unconventional coating deposition mechanism / X. Wang, D. Zhou, Z. Guo, F. Wang, Y. Qiu, J. Huang // Surface and Coatings Technology. — 2023. — Vol. 466. — P. 129634.

19 Ульяницкий В.Ю. Детонационные покрытия из оксидов / В.Ю. Ульяницкий, И.С. Батраев, А.А. Штерцер // Отработка концентрированными потоками энергии. — 2015. — № 5. — С. 37–44.

20 Bye G.C. Influence of Cr and Fe on formation of α-Al_2O_3 from γ- Al_2O_3 / G.C. Bye, G.T. Simpkin // Journal of the American Ceramic Society. — 2006. — Vol. 53(8). — P. 367–371.

Ж.Б. Сағдолдина, Б.К. Рахадилов, Д.Б. Буйткенов, Л.Г. Сулюбаева, А.Б. Нәбиолдина, Н.С. Райсов, С.Д. Болатов

Жоғары температуралы тотығу кезінде NiCr/NiCr–Al_2O_3/Al_2O_3 негізіндегі детонациялық көп қабатты жабындардың құрылымдық-фазалық күйін зерттеу

Жұмыста жоғары температуралы тотығу (оксидтеу) жағдайында детонациялық бүрку әдісі мен алынған көп қабатты жабындардың құрылымдық-фазалық күйінде болатын өзерістер бойынша зерттеу нәтижелері ұсынылған. Зерттеу жұмысының негізгі мақсаты детонациялық жабындардың құрылымдық-фазалық күйіне жоғары температураның әсері және олардың тотығу процестерінің алдын алудағы тиімділігін анықтау. Зерттеу жұмысының нәтижесінде жоғары температуралық сынақтардан кейін детонациялық көп қабатты жабындардың құрылымында $NiCr_2O_4$, Al_2O_3 және Cr_2O_3 сияқты қорғаныс фазаларының түзілетіні анықталды, сондай-ақ бұл фазалар металл бетінің қарқынды тотығуын болдырмауда шешуші рөл атқаратыны белгілі болды. $NiCr_2O_4$ фазасы металл қабатының тұрақтылығын қамтамасыз етуші екені айқындалды, ал Al_2O_3 және Cr_2O_3 бетті қоршаған ортаның агрессивті әсерінен қорғайтын тиімді кедергілер ретінде әрекет етеді. Көп қабатты жабындарда зерттеу жұмысының барысында бұзылу немесе қабыршақтану сияқты белгілердің байқалмағанын атап өту маңызды. Керісінше қапталмаған үлгі (12Х18Н10Т болаты) үшін бірінші циклден кейін оксидті пленканың бөлінуі байқалды, бұл массаның айтарлықтай жоғалуына (төмендеуіне) әкелді. Бастапқы болат массасының жоғалуы айтарлықтай жоғары екендігі анықталды, бұл оның бетінде оксидтердің тезірек түзілуін көрсетеді. Осылайша, зерттеу нәтижелері детонациялық көп қабатты жабындардың жоғары температура кезінде тотығу процестерінен қорғауда тиімді екенін растайды және де экстремалды жылу әсерлері жағдайында материалдың тұрақтылығы мен беріктігін сақтауда маңыздылыққа ие екенін көрсетеді.

Кілт сөздер: детонациялық бүрку, құрылым, фазалық құрамы, жоғары температуралы тотығу, көп қабатты жабындар.

Ж.Б. Сағдолдина, Б.К. Рахадилов, Д.Б. Буйткенов, Л.Г. Сулюбаева, А.Б. Нәбиолдина, Н.С. Райсов, С.Д. Болатов

Исследование структурно-фазового состояния детонационных многослойных покрытий на основе NiCr/NiCr–Al_2O_3/Al_2O_3 при высокотемпературном окислении

В работе представлены результаты исследования структурно-фазового состояния детонационных многослойных покрытий в условиях высокотемпературного окисления. Основная цель эксперимента — выяснить, как воздействие высоких температур влияет на состояние этих покрытий и их способность предотвращать окислительные процессы. В результате исследования было обнаружено, что после высокотемпературных испытаний в структуре детонационных многослойных покрытий формируются защитные фазы, такие как $NiCr_2O_4$, Al_2O_3 и Cr_2O_3. Было установлено, что эти фазы играют ключевую роль в предотвращении интенсивного окисления металлической поверхности. Особенно выделяется роль $NiCr_2O_4$, обеспечивающего устойчивость металлического слоя, и Al_2O_3 с Cr_2O_3, которые действуют как эффективные барьеры, защищающие поверхность от воздействия окружающей среды. Важно отметить, что в многослойных покрытиях не обнаружено признаков разрушения или отслоения в течение всего эксперимента. В отличие от этого, в образце без покрытия (сталь 12Х18Н01Т) уже после первого цикла наблюдалось отслоение оксидной пленки, что существенно увеличило потерю массы. Определено, что потеря массы у стали без покрытия значительно выше, что указывает на более быстрое образование оксидов на её поверхности. Таким образом, результаты исследования подтверждают эффективность детонационных многослойных покрытий в защите от окислительных процессов при высоких температурах, а также указывают на то, что они играют важную роль в поддержании стабильности и прочности материала в условиях экстремальных тепловых эффектов.

Ключевые слова: детонационное напыление, структура, фазовый состав, высокотемпературное окисление, многослойные покрытия.

References

1 Salahov, A.M. (2016). Sovremennye keramicheskie materialy [Modern ceramic materials]. *Ministerstvo obrazovaniia i nauki RF; Kazanskii federalnyi universitet — Ministry of Education and Science of the Russian Federation, Kazan Federal University* [in Russian].

2 Okavity, V.A., Shevtsov, A.I., Okavity, V.V., Astashinsky, V.M., & Kostyukevich, E.A. (2014). Paramets optimization for plasma spraying and pulsed plasma treatment of surface layers of gas-thermal composite coatings based on multifunctional oxid4 ceramics. *High Temperature Material Processes*, *18* (1-2), 45–62.

3 Bassiouny, S., Jinghua, J., Reham, F., Tareq, A., Qiong, X., Lisha, W., Dan, S., & Aibin, M. (2020). 30 Years of functionally graded materials: An overview of manufacturing methods. *Applications and Future Challenges, Composites Part B: Engineering*, *201*, 108376.

4 Sova, A., Pervushin, D., & Smurov, I. (2010). Development of multimaterial coatings by cold spray and gas detonation spraying. *Surface and Coatings Technology*, *205*(4), 1108–114.

5 Ozgurluak, Y., Gulec, A., Ozkan, D., Binal, G., & Karaoglanly, A.C. (2023). Structural characteristics, oxidation performance and failure mechanism of thermal barrier coatings fabricated by atmospheric plasma spraying and detonation gun spraying. *Engineering Failure Analysis*, 152, 107499.

6 Kameneva, A., & Kichigin, V. (2019). Corrosion, wear, and friction behavior of a number of multilayer two-, three- and multicomponent nitride coatings on different substrates, depending on the phase and elemental composition gradient. *Applied Surface Science*, 489, 165–174.

7 Sathish, M., Radhika, N., & Bassiouny, S. (2021). A critical review on functionally graded coatings: Methods, properties, and challenges. *Composites Part B: Engineering*, 225, 109278.

8 Maulet, M., Sagdoldina, Zh.B., Rakhadilov, B.K., Kakimzhanov, D.N., & Magazov, N.M. (2022). Influence of the content of aluminum on the structure of gradient detonation coatings based on NiCr-Al. *Bulletin of the University of Karaganda – Physics*, *3*(107), 18–24. DOI: 10.31489/2022PH3/18-24.

9 Vandana, C.M., Chakravarthy, Y., Khare, N., Singh, K., & Ghorui, S. (2019). Strongly adherent Al_2O_3 coating on SS 316L: Optimization of plasma spray parameters and investigation of unique wear resistance behaviour under air and nitrogen environment. *Ceramics International*, *46*(7), 9. DOI: 10.1016/j.ceramint.2019.12.099.

10 Rakhadilov, B., Kakimzhanov, D., Baizhan, D., Muslimanova, G., Pazylbek, S., & Zhurerova, L. (2021). Comparative study of structures and properties of detonation coatings with α- Al_2O_3 and γ- Al_2O_3 main phases. *Coatings*, *11*, 1566.

11 Lashmi, P.G, Ananthapadmanabhan, P.V., Unnikrishnan, G., & Aruna, S.T. (2020). Present status and future prospects of plasma sprayed multilayered thermal barrier coating systems. *J Eur Ceram Soc*, *40*(8), 2731–2745.

12 Pogrebnjak, A.D., Iljashenko, M., Kulmenteva, O.P., Kshnajakin, V.S., Kobzev, A.P, Tyurin, Y.N., & Kolisnichenko, O. (2001). Structure and properties of Al_2O_3 and Al_2O_3+Cr_2O_3 coatings deposited to steel 3 (0.3 wt%C) substrate using pulsed detonation technology. *Vacuum*, *62*(1), 21–26.

13 Rakhadilov, B., Buitkenov, D., Sagdoldina, Z., Idrisheva, Z., Zhamanbayeva, M., & Kakimzhanov, D. (2021). Preparation and characterization of NiCr/NiCr–Al_2O_3/Al_2O_3 multilayer gradient coatings by gas detonation spraying. *Coatings*, *11*(12), 1524.

14 Sreedhar, G., Alam, MD.M., & Raja, V.S. (2009). Hot corrosion behaviour of plasma sprayed YSZ/Al_2O_3 dispersed NiCrAlY coatings on Inconel-718 superalloy. *Surface & Coatings Technology*, *204*, 291–299.

15 Rakhadilov, B.K., Tyurin, Yu.N., Kolisnichenko, O.V., Kakimzhanov, D.N., & Zhurerova, L.G. (2022). Structure and properties of multilayer coatings based on CoCrAlY/Al_2O_3 obtained by detonation spraying. *Eurasian Journal of Physics and Functional Materials*, *6*(3), 234–243.

16 Rakhadilov, B.K., Kakimzhanov, D.N., Buitkenov, D.B., Kozhanova, R.S., Zhurerova, L.G., & Sagdoldina, Zh.B. (2023). Tribological and mechanical properties of gradient coating on Al_2O_3 based coating produced by detonation spraying methods. *Advances in Tribology*, 9.

17 Rakhadilov, B., Buitkenov, D., Sagdoldina, Zh., Idrisheva, Zh., Zhamanbayeva, M., & Kakimzhanov, D. (2021). Preparation and Characterization of NiCr/NiCr–Al_2O_3/ Al_2O_3 Multilayer Gradient Coatings by Gas Detonation Spraying. *Coatings*, *11*(12), 1524.

18 Wang, X., Zhou, D., Guo, Z., Wang, F., Qiu, Y., & Huang, J. (2023). Manufacturing and the process-structure-property correlation of detonation sprayed iron coatings under an unconventional coating deposition mechanism. *Surface and Coatings Technology*, *466*, 129634.

19 Ulyanickii, V.Yu., Batraev, I.S., & Shtercer, A.A. (2015). Detonatsionnye pokrytiia iz oksidov [Detonation oxide coatings]. *Otrabotka kontsentrirovannymi potokami energii* **—** W*orking out with concentrated energy flows*, 5, 37–44 [in Russian].

20 Bye, G.C. & Simpkin, G.T. (2006). Influence of Cr and Fe on formation of α-Al_2O_3 from γ- Al_2O_3. *Journal of the American Ceramic Society*, *53*(8), 367–371.

Information about authors

Sagdoldina, Zhuldyz — PhD, Associate Professor, Senior Researcher of Scientific Research Center "Surface Engineering and Tribology", S. Amanzholov East Kazakhstan University, Ust-Kamenogorsk, Kazakhstan; e-mail:zh.sagdoldina@gmail.com; ORCID ID: https://orcid.org/0000-0001-6421-2000;

Rakhadilov, Bauyrzhan — PhD, Associate Professor, Director of PlasmaScience LLP, Ust-Kamenogorsk, Kazakhstan; e-mail: rakhadilovb@gmail.com; ORCID ID:https://orcid.org/0000-0001-5990-7123;

Buitkenov, Dastan — PhD, Leading Researcher of Scientific Research Center “Surface Engineering and Tribology”, S. Amanzholov East Kazakhstan University, Ust-Kamenogorsk, Kazakhstan; e-mail: buitkenov@gmail.com;ORCID ID:https://orcid.org/0000-0002-0239-5849;

Sulyubayeva, Laila — PhD, Associate Professor, Senior Researcher of Scientific Research Center “Surface Engineering and Tribology”, S. Amanzholov East Kazakhstan University, Ust-Kamenogorsk, Kazakhstan; e-mail:lsulyubayeva@gmail.com; ORCID ID:https://orcid.org/0000-0002-1924-1459;

Nabioldina, Aiym (contact person) — Junior Researcher of Scientific Research Center “Surface Engineering and Tribology”, S. Amanzholov East Kazakhstan University, Ust-Kamenogorsk, Kazakhstan; e-mail: anabioldina@gmail.com; ORCID ID:https://orcid.org/0000-0001-5581-2194;

Raisov, Nurmahanbet — Engineer of Scientific Research Center “Surface Engineering and Tribology”, S. Amanzholov East Kazakhstan University, Ust-Kamenogorsk, Kazakhstan; e-mail: 2002raisov@gmail.com; ORCID ID:https://orcid.org/0009-0007-1698-957X;

Bolatov, Sanzhar — Engineer of Scientific Research Center “Surface Engineering and Tribology”, S. Amanzholov East Kazakhstan University, Ust-Kamenogorsk, Kazakhstan; e-mail: sanzharbolatov94@gmail.com; ORCID ID: https://orcid.org/0009-0003-3136-0535.

Article

Received: 18.12.2023
Accepted: 27.03.2024

UDC 541.6:541.1223

https://doi.org/10.31489/2024PH2/36-42

Azizov Samir

Ministry of Science and Education of the Republic of Azerbaijan, Institute of Physics, H. Javid ave131, AZ-1143 Baku, Azerbaijan
**(Corresponding author's e-mail: samir_azizov@mail.ru)*

Investigation of the temperature dependence of the dielectric relaxation of chlorobenzene, bromobenzene and iodobenzene

This paper deals with the investigation results of temperature dependence of complex permittivity's$\varepsilon^* = \acute{\varepsilon} - i\varepsilon''$ of chloro, bromo and iodo- benzene at wavelength 11,50 cm and 12,80 cm within the temperature range 20 ÷ -80˚. It is established that dielectric properties of given liquids are characteristic of one relaxation time. The dielectric spectra were studied taking into account other frequencies given in the literature. In all investigated liquids, a jump appears in the real and imaginary parts of the complex permittivity at the point of the phase transition. The temperature dependence of the dielectric relaxation time of molecules in the liquid state has been determined. It was found that with an increase in the amount of the halogen substituent, an increase in the relaxation time occurs. Macroscopic and molecular relaxation times were calculated from the experimental values. The thermodynamic quantities characterizing the process of dielectric relaxation are calculated. The activation enthalpy of dielectric relaxation processes is compared. The studies were carried out using the dielectric spectroscopy method. This method allows a more detailed study of the dielectric properties of the objects of study due to the large equilibrium ("static") dielectric constant of the object. It has been determined that the height of the potential barrier separating the two equilibrium positions of a polar molecule is greatest in the state of a pure polar liquid and decreases with dilution in a non-polar solvent.

Keywords: dielectric spectroscopy, complex dielectric constant, dielectric properties, benzene, bromobenzene, chlorobenzene, iodo-benzene.

Introduction

The study of the dielectric properties of polar liquids is one of the most fundamental and complex problems of science, which is of great theoretical and practical importance. Interpretation of experimental data on dielectric relaxation presents difficulties for substances that are characterized by the presence of intramolecular interactions, hydrogen bonds and other complicating factors. Therefore it is advantageous to investigate rather elementary molecules. At the moment, the central place in the works involved in the study of intermolecular interactions in liquids is occupied by studies of the molecular structure of a liquid and the dynamics of its transformation during thermal motion. To solve these problems, modern physical and physico-chemical research methods are used, such as diffraction and thermodynamic methods, dielectric, acoustic spectroscopy, etc. [1].

Among these methods, an important place belongs to dielectric spectroscopy [2-3]. Studies of the dielectric properties of polar liquids make it possible to obtain extensive information about their molecular structure, intermolecular interactions, information about thermodynamic parameters, mechanisms of molecular processes, as well as the process of absorption of electromagnetic radiation. According to the available literature the investigation results of relaxation phenomena observed in microwave range are rather limited and often-contradicted. In particular by data [4–7] in benzene halogen derivatives the distribution of relaxation time is taken place. Yet the results [8–11] are indicative of presence of one relaxation time. On the base of experimental data analysis the conclusion has been confirmed by probable presence of additional dispersion region at millimetric waves in benzene halogen derivatives.

Various molecular associations are determined in terms of relaxation time τ and dipole moment μ to estimate different molecular interactions among polar molecules or polar-non-polar molecules. Thermodynamic energy parameters are also calculated using Eyring's rate theory to predict molecular dynamics or nature of molecular environment surrounding the polar molecules DMF, DMA or phenol (p-cresol, p-chlorophenol, 2,4dichlorophenol and p-nitrophenol). The existence of the Debye relaxation mechanism in all the systems under observation is validated by the estimated Debye factor from both of the measurement methods [15].

Various molecular associations are determined in terms of relaxation time s and dipole moment l in polar-non-polar liquid mixture. Thermodynamic energy parameters are also calculated from Eyring rate theory

to predict molecular dynamics or nature of molecular environment surrounding the polar molecule TBP. Debye relaxation mechanism in all the systems under observation is validated by the estimated Debye factor from both the measurement methods. A new simple microwave sensor is proposed to design for determination of TBP concentration from measured penetration depth at different temperatures under microwave field [16].

The study of the anomalous dispersion of the permittivity of liquids and the strong absorption of electromagnetic energy associated with it makes it possible to judge the nature of intermolecular forces and the molecular structure of polar liquids [12–14].

The anomalous dispersion of polar liquids is determined by the relaxation time τ, which characterizes the process of polarization in a dielectric when an external field is applied. The relaxation time is related to the frequency of the maximum absorbed wave ωm by the condition.

Exsperimental

The polar liquids chlorobenzene, bromobenzene, and iodobenzene (United States, Keysight Technologies) were chosen as the objects of study. Measurements are carried out by method suggested and on assembled installation [3–5] which allows the complex dielectric constant $\varepsilon^* = \acute{\varepsilon} - i\acute{\varepsilon}''$ of highly absorbed substances to be determined.

The short-circuited line method [3–6] uses the relationship between the input impedance Z_0 and the complex propagation constant γ of a line filled with a dielectric. Since the value of γ, in turn, is related to the complex permittivity ε*, by measuring the value of Z_0, one can find the value of the complex permittivity ε*.

$$\gamma = \alpha + i\beta = i\omega(\varepsilon * \mu *)^{\frac{1}{2}}, \quad (3)$$

where α is the damping constant characterizing the decrease in the amplitude of the wave propagating along the line, β is the phase constant characterizing the change in the phase of the same wave, $\mu*$ is the complex magnetic permeability. Taking $\mu* = 1$, we get:

$$\varepsilon^* = \varepsilon' - i\varepsilon'' = \frac{\gamma\lambda_1}{2\pi}. \quad (4)$$

The quantity γ is related to the input impedance Z_0 as follows:

$$\frac{\text{th}\gamma d}{\gamma d} = -i\frac{\lambda_1}{2\pi d}\frac{Z_0}{Z_1}, \quad (5)$$

where d is the thickness of the dielectric, Z_1 is the wave impedance of the air part of the line. The input impedance Z_0 is expressed in terms of the experimentally determined running coefficient $q = E_{min}/E_{max}$ (E is the electric field strength) and the displacement of the node y1 of the standing wave, due to the introduction of a dielectric into the line before the short circuit:

$$Z_0 = Z_1\frac{q - i\,tg\beta_0 y_1}{1 - iq\,tg\beta_0 y_1}, \quad (6)$$

here $\beta_0 = \frac{2\pi}{\lambda_1}$.

It should be noted that in the case of small and medium losses ($tg\delta < 0.1$), accurate results are achieved at thicknesses that are multiples of an odd number of quarters of the wavelength in the sample. For large losses ($tg\delta > 0{,}l$), the sample thickness has to be taken so small that it itself becomes a source of noticeable errors. Another disadvantage is the extreme sensitivity of the detector part of the equipment to temperature fluctuations, which seriously complicates temperature measurements. Both of these shortcomings can be eliminated in a new modification of the method [5]. The essence of this modification is that the input impedance of a short-circuited line filled with a dielectric is transformed into a measuring line in such a way that optimal conditions for measurements are created. By measuring the transformed impedance, by the known transformation coefficient, the required input impedance of the line filled with a dielectric is found [3, 4, 6]. Measurements are made out over a wide temperature range. Mean deviation for values $\acute{\varepsilon}$ does not exceed 1%, for values $\acute{\varepsilon}''$ is 3%. It should be noted that dielectric properties of abovementioned liquids at low temperatures are not clearly investigated.

The essence of the novelty of the proposed method is that the input impedance of a short-circuited line filled with a dielectric is transformed into a measuring line in such a way that optimal conditions for measurements are created. By measuring the transformed impedance, using a known transformation coefficient, the desired input impedance of the line filled with a dielectric is found.

The method proposed in the article can be used in the microwave range and in the temperature range corresponding to the condition of phase transition from the liquid state of the solutions under study to the solidification phase of the solutions under study.

Result and Discussion

In present paper there have been given investigation results of dielectric relaxation of three benzene halogen derivatives (C_6H_5C1, C_6H_5Br, C_6H_5J) at wave length 11,50 cm and 12,80 cm within the temperature range 20 ÷ -80˚C. Temperature range is effective in liquid phase as well as in solid one of liquids under investigation.

In Figure 1 and 2 there have been shown the data of temperature dependence of real ε' and imaginary ε'' parts of complex dielectric constant ε^* for chlorobenzene, bromobenzene and iodo-benzene. Curve graphs for chlorobenzene and iodo-benzene have been obtained at wavelength 12,80 cm. Curve diagrams for bromobenzene have been obtained at wavelength 11,50 cm.

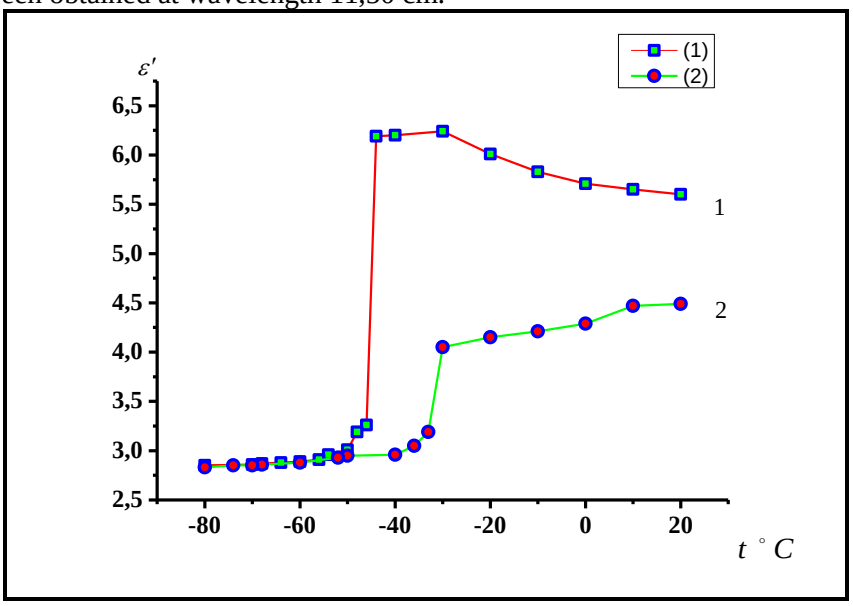

Figure 1. Temperature dependence of dielectric constant ε', 1 is the chlorobenzene; 2 is the iodo-benzene

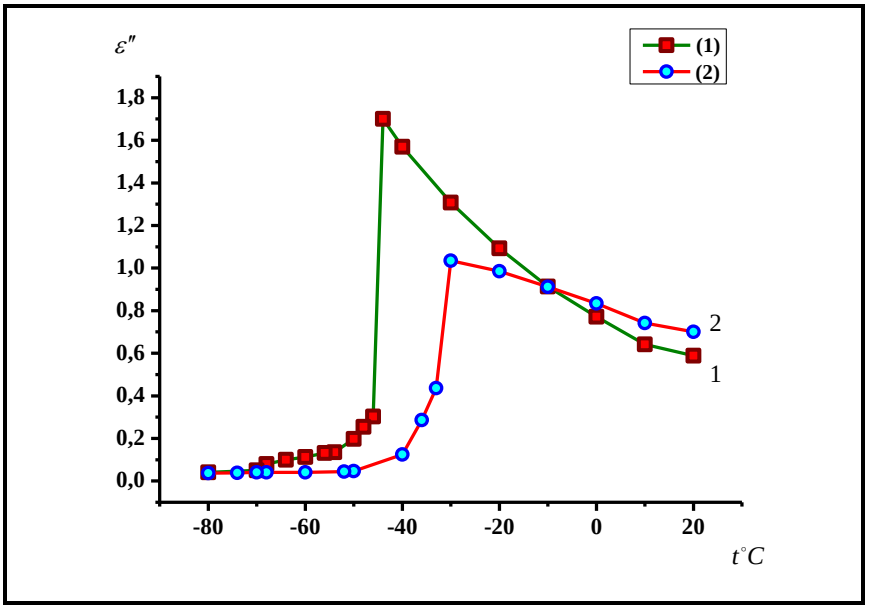

Figure 2. Temperature dependence of absorption coefficient ε'', 1 is the chlorobenzene; 2 is the iodo-benzene

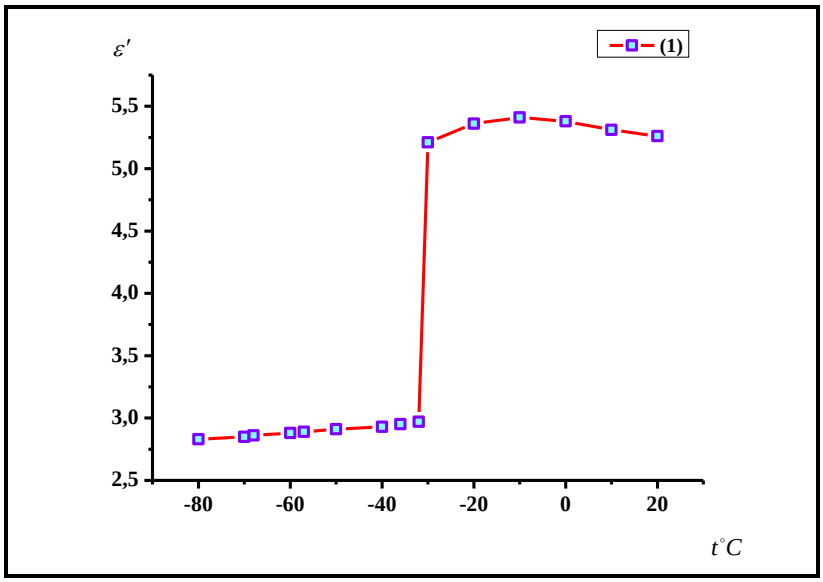

Figure 3. Temperature dependence of dielectric constant ε' is the bromobenzene

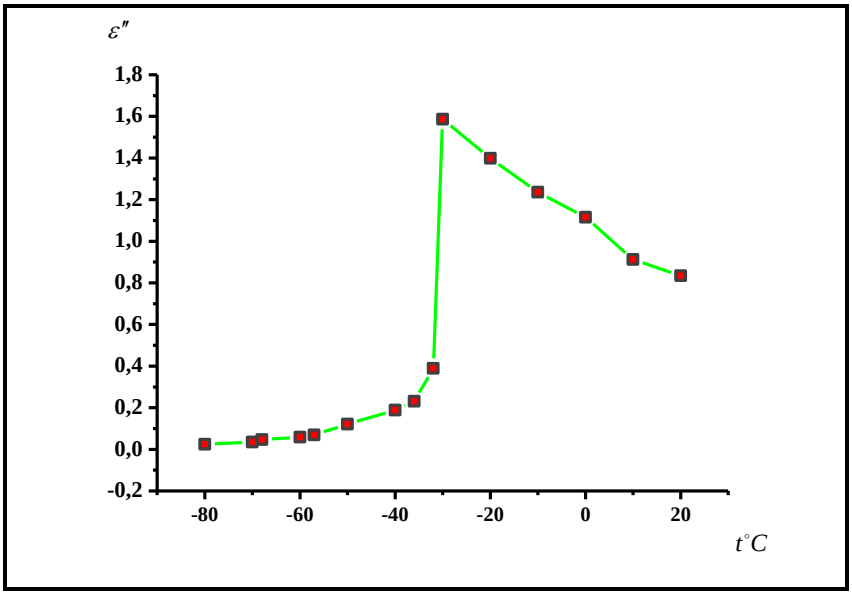

Figure 4. Temperature dependence of absorption coefficient ε'' is the bromobenzene

For all substances under examination the phase transition agrees with the complex dielectric constant jump ε^*. In this case the constant value ε' settles at several degrees after transition (Fig. 3). Dielectric loss is retained at the same range which is observed both by cooling and by heating objects under study. Mentioned pecularities of temperature change of complex dielectric constant values ε^* may be attributed to the liquid structure. According to them close to the hardening temperature the clusters of molecule groups have been occurred (Fig. 4). It is evident that after hardening the dielectric properties over a given temperature ranges are determined by isolated molecules not included in these clusters. While attaching to the clusters the orientation part of polarization is avoided.

Figure 5 illustrates reducible iodo-benzene diagram. In case of chlorobenzene and bromobenzene the diagrams have a similar type. Values ε_0 and ε_∞ have been taken from literature and extrapolated [5].

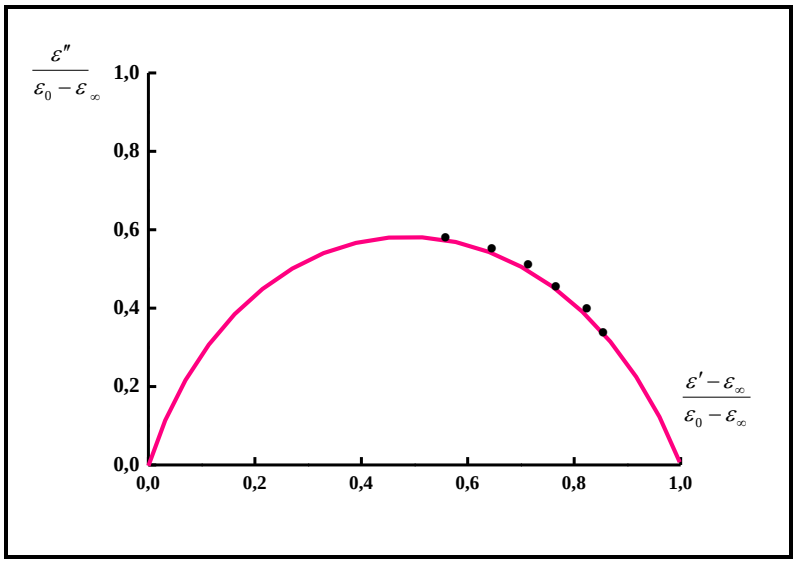

Figure 5. Reducible iodo-benzene diagram

It is seen from the diagram that dielectric properties up to the transition temperature is characteristic of one relaxation time. Therefore relaxation time values have been calculated by the familiar Debye formula. It should be noted that the factor providing for the presence of internal field is taken to be equal a unit. In this case this factor is practically independent of the temperature. Consequently obtained values can be used for interpretation of dielectric relaxation temperature change.

If we suppose that dipole molecule orientation is carried out by its transition through potential barrier separating two equilibrium position of molecules the relaxation time is defined as follows [6]:

$$\tau = exp\frac{U}{RT}(1),$$

where U is the activation energy, R is the Boltzmann constant, T is the temperature. We note that activation energy can be evaluated from slope of the dependence $ln\tau$ on $\frac{1}{T}$.

Table lists the appropriate values of activation energy. There have been presented energy magnitudes established by scattering line width growth values for comparison [7].

T a b l e

Substance	Activation energy kcal /mol	
	Dielectric measurements	Measurements of scattering line width growth values
Chlorobenzene	1,9	2,1
Bromobenzene	2,1	2,3
Iodo- benzene	2,3	2,4

Conclusions

The paper presents a new modification of the short-circuited line method, with the help of which it is possible to study the temperature dependence of the complex permittivity of polar liquids in the microwave range. This method is based on the transformation of the input resistance of a short-circuited line filled with the liquid under study. Data on the temperature dependence of the complex permittivity ε* of chlorobenzene, bromobenzene and iodo-benzene in the range of –80°C ÷ +20°C at a wavelength of 11.5 cm are presented. When passing through the solidification point of these liquids, a sharp change in the value of the complex permittivity ε* was found. The value of the relaxation time over the entire temperature range and the activation energy for the molecules of liquid chlorobenzene, bromobenzene, and iodo-benzene are found. As a result of pursuance of research we can state that in all cases the activation energy for dielectric relaxation have the values rather close to the values established by scattering line width growth.

References

1 Gusev, Yu.A. (2008). Fundamentals of dielectric spectroscopy. *Tutorial Kazan KSU,* P. 112.

2 Vuks, M.F. (1984). *Electrical and Optical Properties of Molecules and Condensed Matter*. Leningrad, P. 334. Retrieved from https://search.rsl.ru/ru/record/01001225959

3 Azizov, S.T., & Aliyev, O.A. (2022). Dielectric relaxation of bromobenzene in the microwave range. *AJP Fizika, section C: Conference L.M. Imanov,* 57–60. Retrieved from http://physics.gov.az/physart/014_2022_C-ILM_57_az.pdf

4 Azizov, S.T., & Gasanova, A.S. (2022). Research of complex dielectric constant of chlorobenzene in the microwave range. *AJP Fizika, section C: Conference, M.H. Shahtakhtinski,* 30–32. Retrieved from http://physics.gov.az/physart/008_2022_C-ShMH_30_az.pdf

5 Kasimova, S.R. (2021). Information support of methods for measuring the dielectric properties of absorbing liquids. *Science, technology and education*, *4*(79), 22–24. Moscow.

6 Salaev, E.Y., Gasimov, E.R., Qajar, Ch.O., & Azizov, S.T. (1998). Resonans reflektionles absorbpnion of elektromagnetik waves in solutions. *Turkish journal of Physics, 5,* 389–393. Retrieved from https://journals.tubitak.gov.tr/physics/vol22/iss5/4/

7 Kremer, F., & Schonhals, A. (2002). Broad band Dielectric Spectroscopy, P. 729. Retrieved from https://link.springer.com/book/10.1007/978-3-642-56120-7

8 Akhadov, Ya.Yu. (1999). Dielectric parameters of pure liquids. Moscow, P. 854. Retrieved from https://search.rsl.ru/ru/record/01000640835

9 Azizov, S.T., Aliev, O.A., & Abaszade, R.G. (2019). Equilibrium and dynamic properties of dielectric polarization of chlorobenzene-n-butyl alcohol syste. *National Academy of Sciences of Ukraine V.E. Lashkaryov Institute of Semiconductor Physics. The conference of young scientists in semiconductor physics "Lashkariv Readings" with international participation, April 3–5,* P. 68.

10 Doroshenko, I., Pitsevich, G., & Shablinskas, V. (2012). Cluster structure of liquid alcohols: study by vibrational spectroscopy. *LAMBERT Academic Publishing,* P. 290.

11 Qacar, C.O., Azizov, S.T., Aliev, O.A., & Zulfugarzade, K.E. (2015). Dielectric spectroscopy of mesoorder in acetone. *TRANSACTIONS of Azerbaijan National Academy of Sciences, series of physical – technical and mathematical sciences, physics and astronomy,* 66–73. Retrieved from http://physics.gov.az/Transactions/2015/journal2015(5).pdf

12 Azizov, S.T., Agamuradova, Sh.K., & Aliev, O.A. (2009). Dielectric properties and molecular structure of a solution of nitromethane – dioxane. *XII Interregional Conference of young scientists on the physics of semiconductor, dielectric and magnetic materials,* 195–199. Vladivostok.

13 Kasimova, S.R. (2016). Measurements of the Dielectric Properties of Strongly Absorbing Substances at Microwave Frequencies. *Measurement Techniques, 8,* 1372–1375. USA, New York.

14 Kumar, S., Sivakumar, S., & Jeevanandham, P. (2010). Molecular interaction and dielectric relaxation studies of cycloalcohols with acetamide in a non – polar solvent using frequency domain technique. *International Journal of Recent Scientific Research IJRSR,* 177–181.

15 Kumar, Dilip, Kumar, Sit Swapan, N., Shiva, & Swagatadeb Sahoo, Singh (2021). Dielectric Relaxation Behavior of Amide and Phenol Mixtures in C6H6 Under Microwave Field. *Journal of Solution Chemistry*, 690–722.

16 Bachhar, T., Sit, S., & Laskar, S. (2021). Investigation of dielectric relaxation in tributyl phosphate from susceptibility and conductivity measurement under microwave field. *Bulletin of Materials Science*, 120–126.

С. Азизов

Хлорбензол, бромбензол және йодбензолдың диэлектрлік релаксациясының температураға тәуелділігін зерттеу

Жұмыста 20÷-80 температура аралығындағы 11,50 және 12,80 см толқын ұзындығындағы хлор, бром және йодбензолдың ε^*=ε^-iε^″ күрделі диэлектрлік өткізгіштіктерінің температураға тәуелділігін зерттеу нәтижелері келтірілген. Бұл сұйықтықтардың диэлектрлік қасиеттері бір релаксация уақытына тән екендігі белгілі болды. Диэлектрлік спектрлер әдебиетте келтірілген басқа жиіліктерді ескере отырып зерттелді. Зерттелген барлық сұйықтықтардың фазалық ауысу нүктесінде күрделі диэлектрлік өткізгіштіктің нақты және болжалды бөліктерінің секірісі пайда болады. Сұйық күйдегі молекулалардың диэлектрлік релаксация уақытында температураға тәуелділігі анықталды. Галоген алмастырғыш мөлшерінің жоғарылауымен релаксация уақытының ұзақтығы арта түсетіні айқындалды. Тәжірибелік мәндерден макроскопиялық және молекулалық релаксация уақыттары табылды. Диэлектриктердің релаксациялану процесін сипаттайтын термодинамикалық шамалар есептелген. Диэлектриктердің релаксация процестерінің активтену энтальпиясы салыстырылды. Зерттеулер диэлектрлік спектроскопия көмегімен жүргізілді. Бұл әдіс объектінің үлкен тепе-теңдік («статикалық») диэлектрлік өтімділігіне байланысты зерттеу объектілерінің диэлектрлік қасиеттерін егжей-тегжейлі зерттеуге мүмкіндік береді. Полярлы молекуланың екі тепе-теңдік жағдайын бөлетін потенциалдық тосқауылдың биіктігі таза полярлы сұйықтық күйінде ең үлкен және полярсыз еріткішпен сұйылтылғанда ең төмен болатыны нақтыланды.

Кілт сөздер: диэлектрлік спектроскопия, күрделі диэлектрлік өтімділік, диэлектрлік қасиеттер, бензол, бромбензол, хлорбензол, йодбензол.

С. Азизов

Исследование температурной зависимости диэлектрической релаксации хлорбензола, бромбензола и йодбензола

В работе представлены результаты исследования температурной зависимости комплексных диэлектрических проницаемостей ε^*=ε^́-iε^″ хлора, брома и йодбензола на длинах волн 11,50 и 12,80 см в интервале температур 20÷–80˚. Установлено, что диэлектрические свойства данных жидкостей характерны для одного времени релаксации. Диэлектрические спектры изучались с учетом других частот, приведенных в литературе. Во всех исследованных жидкостях возникает скачок действительной и мнимой частей комплексной диэлектрической проницаемости в точке фазового перехода. Определена температурная зависимость времени диэлектрической релаксации молекул в жидком состоянии. Установлено, что с увеличением количества галогенового заместителя возрастает продолжительность времени релаксации. Время макроскопической и молекулярной релаксации определяли по экспериментальным значениям. Рассчитаны термодинамические величины, характеризующие процесс диэлектрической релаксации. Сравнивалась энтальпия активации процессов диэлектрической релаксации. Исследования проводились методом диэлектрической спектроскопии. Данный метод позволяет детально изучить диэлектрические свойства объектов исследования благодаря большой равновесной («статической») диэлектрической проницаемости объекта. Установлено, что высота потенциального барьера, разделяющего два положения равновесия полярной молекулы, наибольшая в состоянии чистой полярной жидкости и наименьшая при разбавлении неполярным растворителем.

Ключевые слова: диэлектрическая спектроскопия, комплексная диэлектрическая проницаемость, диэлектрические свойства, бензол, бромбензол, хлорбензол, йодбензол.

Information about athors

Azizov, Samir (contact person) — Candidate of physical and mathematical sciences, Leading researcher, Ministry of Science and Education of the Republic of Azerbaijan, Institute of Physics; email: samir_azizov@mail.ru.

Article

Received: 31.01.2024
Accepted: 03.04.2024

UDC**:** 621.315.592, 530, 574

https://doi.org/10.31489/2024PH2/43-52

E.R. Hasanov[1,2], Sh.G. Khalilova[2*], R.K. Mustafayeva[1]

[1]*Baku State Uviversity, Baku, Azerbaijan Republic;*
[2]Institute of Physics, Baku, *Azerbaijan Republic*
[*]*(Corresponding author's e-mail: shahlaganbarova@gmail.com)*

Excitation of transverse and longitudinal thermomagnetic waves in anisotropic conducting media in the presence of a temperature gradient $\vec{\nabla}T$ without an external magnetic field H

In anisotropic conducting media, the excited thermomagnetic waves at different orientations of the magnetic field and temperature gradient significantly depend on the direction of the anisotropic medium. Theoretical calculations of the electrical conductivity tensor σ_{ik} depending on the frequency of the thermomagnetic wave are of scientific interest. In this theoretical work, the frequencies of the thermomagnetic wave at $\vec{k} \parallel \vec{\nabla}T$ and at $\vec{k} \perp \vec{\nabla}T$ were found, and it was proven that at longitudinal ($\vec{k} \parallel \vec{\nabla}T$) and at transverse ($\vec{k} \perp \vec{\nabla}T$) the direction of the frequency and growth rate of these waves depends differently on the external magnetic field. The work theoretically studies the conditions for the excitation of thermomagnetic waves. It is indicated that the directions of external fields play a significant role in the appearance of growing waves in the sample. It is shown that, depending on the value of the electrical conductivity tensor σ_{ik}, thermomagnetic waves are excited in the longitudinal (i.e. $\vec{k} \parallel \vec{\nabla}T$) and transverse (i.e. $\vec{k} \perp \vec{\nabla}T$) directions. The frequencies of these thermomagnetic waves in both the longitudinal and transverse directions have been calculated. The growth rates of these waves are determined by the values of the inverse electrical conductivity tensor σ_{ik}. It has been proven that the excited wave is mainly of a thermomagnetic nature. In theory, the dispersion equation obtained is of algebraically high powers relative to the oscillation frequency. The dispersion equation in both cases (longitudinal $\vec{k} \parallel \vec{\nabla}T$ and transverse $\vec{k} \perp \vec{\nabla}T$) contains terms in which there are thermomagnetic frequencies in a low degree of frequency. It has been proven that if the value of the electrical conductivity tensor σ_{ik} is the same, then the propagation frequencies of thermomagnetic waves are different. The theory is constructed without an external magnetic field $H_0 = 0$. In the presence of an external magnetic field, the conditions for the excitation of thermomagnetic waves, and of course the conditions for their growth, will change significantly.

Keywords: frequency, increment, thermomagnetic waves, transverse waves, longitudinal waves, growth, electrical conductivity tensor, inverse tensor.

Introduction

In works [1–4] it was proven that hydrodynamic movements in a plasma in which there is a constant temperature gradient give rise to a magnetic field. In this case, the plasma has oscillatory properties that are noticeably different from ordinary plasma. In such a plasma, thermomagnetic waves are excited, in which only the magnetic field oscillates. In the presence of an external magnetic field, the wave vector of thermomagnetic waves is perpendicular to the magnetic field or lies in the plane $\vec{H},\vec{\nabla}T$. The speed of thermomagnetic waves is comparable to the speed of sound and the speed of the Alfvén wave. The temperature gradient does not depend on time or coordinates. The Larmor frequency of charge carriers is less than the frequency of their collisions, i.e.

$$\Omega\tau << 1,\ \Omega = \frac{eH}{mc}\ . \tag{1}$$

It has been suggested that magnetic fields exist for explaining the production of cosmic rays and cosmic radio waves. Such fields are based on both the Fermi's statistical mechanism for the acceleration of charged particles and bremsstrahlung at radio frequency by relativistic electrons.

However, the mechanism by which sufficiently strong magnetic fields can be created remains unclear. In [1] it is shown that hydrodynamic motion in a nonequilibrium plasma, in which the existence of a temperature gradient leads to the formation of magnetic fields. Under such conditions, ions arise for which the Larmor frequency of ions is comparable to the oscillation frequency. An increase in parametric resonance and, possibly, resonant acceleration of ions is realized. In sufficiently weak acoustic waves, parametric resonance occurs for electrons. In a hot plasma with high radiation pressure, much stronger magnetic fields arise in a turbulent nonequilibrium plasma. In [1] it is shown that plasma with a temperature gradient ∇T has oscillatory properties that differ from normal plasma. In the absence of an external magnetic field and hydrodynamic motion, transverse "thermomagnetic" waves are possible in the plasma. Magnetic field oscillations occur in them. If there is a constant external magnetic field H, then the wave vector of the thermomagnetic wave must be perpendicular to it.

In addition, the Alfvén wave is split up into "hydrothermomagnetie" waves in which the vectors v and H are perpendicular to ∇T. The spectrum of magnetic sound waves can be modified. The speed of propagation of the thermomagnetic waves is comparable to the velocity of sound and velocity of the Alfvén wave.

In this work, the magnetic fields are divided as follows $H_\perp = H_{\perp\infty} + H'_\perp$.

$$\begin{aligned} &\upsilon_m k^2 \frac{\partial^2 H_{\perp\infty}}{\partial\xi^2} - k\frac{\partial}{\partial\xi}\left[(\upsilon + u_T - u - u_s)H_{\perp\infty}\right] = ck\frac{\partial E'}{\partial\xi} \\ &\frac{\partial H'_\perp}{\partial t} - \upsilon_m k^2 \frac{\partial^2 H'_\perp}{\partial\xi^2} - k\frac{\partial}{\partial\xi}\left[(\upsilon + u_T - u)H'_\perp\right] = 0. \end{aligned} \tag{2}$$

Here u_s is speed of sound propagation, υ_m is magnetic viscosity, from the solutions of these equations

$$H_\perp = \frac{cT\tilde{\Lambda}\left[\nabla \ln T, k\right]}{ke}\frac{kv_0\cos\xi + v_0\nabla \ln T\sin\xi}{\omega\left(u - u_T - \upsilon_0\cos\xi + u_s\right)}\ . \tag{3}$$

At condition $\upsilon(\xi) << u - u_T + u_s$,

$$H_\perp = \frac{1}{2}\tilde{\Lambda}\frac{\nabla_z T}{e}\frac{c}{s}\left(\frac{\upsilon_0}{s}\right)^2 \tag{4}$$

was obtained.

Showing estimates relate to the case $\upsilon_0 << s$ and $\lambda << L$ are valid at $\upsilon_0 \approx s$ and $\lambda \approx L$. $\Omega \approx N\omega/n$ under a condition $\Omega \approx S/\lambda \approx \omega$. Oscillation and Lamor frequencies can be equal in sound waves. It can likely produce in strong magnetic fields. For $|v_{\max}| > |u - u_T + u_s|$ ($|u - u_T + u_s| < s$) $H_\perp$ can be large than Ω_i. The magnetic fields excited by these processes can be amplified further by of the magnetic field lines.

In [1] the damping of the turbulence that arises from the conversion of part of the energy of turbulence into magnetic energy was estimated. Then for frequency

$$\Omega_1 = eH_1 / mc > \nu \tag{5}$$

was obtained.

In the hydrodynamic movements, in this work the oscillation frequency

$$\omega(k) = \frac{1}{2}\left[\sqrt{4\omega_A^2 + \omega_T^2} \pm \omega_T\right] \tag{6}$$

was obtained

$$\begin{aligned}&\left(\omega^2 - \omega\omega_T - \omega_A^2\right)\left\{\omega^4 - \omega^3\omega_T - \omega^2 k^2\left(s^2 + \upsilon_A^2\right) + \right.\\ &\left. + \omega\left[k^2 s^2 \omega_T + k^2 \upsilon_A\left(k\left[u_1 v_A\right]\right)\right] + \omega_s^2 \omega_A^2\right\} = 0.\end{aligned} \tag{7}$$

The second factor in (7) is the frequencies of the magnetic sound waves determines at $\omega_T = 0$ [2]. At conditions $\omega_A << \omega_s << \omega_T$ or $\omega_T < \omega_s, \omega_A < \omega_T^2/\omega_s$ the solution is $\omega = \pm\omega_s$ and the roots are $\omega \approx \omega_T$, $\omega \approx \omega_A^2/\omega_T$. For large radiation pressure

$$\frac{\omega_1}{\omega_s} = \frac{l}{L}\frac{N}{n}\sqrt{\frac{M}{m}} \geq 1, \tag{8}$$

l is the mean free path of the electrons and N is the number of protons in a unit volume.

In rarefied plasma radiation pressure of the gas and the interaction of electrons with photons is much stronger than Coulomb scattering. The Compton scattering predominates over bremsstrahlung and its corresponding inverse process for electron collisions [3]. The velocity u_i in (7) is increased roughly by N/n times. If N/n is so large that the velocities s and u_T are much smaller than $\left(u_1 u_A^2\right)^{1/3}$.

In the presence of an electric field E, a temperature gradient $\nabla T = const$, a gradient of charge carrier concentrations $\vec{\nabla} n$ and hydrodynamic movements with speed $\vec{\vartheta}(\vec{r},t)$, the electric current density has the form

$$\begin{aligned}&\vec{j} = \sigma\vec{E}^* + \sigma'\left[\vec{E}^*\vec{H}\right] - \alpha\nabla T - \alpha'\left[\nabla T H\right]\\ &E^* = \vec{E} + \frac{\left[\vec{\vartheta}\vec{H}\right]}{c} + \frac{T}{e}\frac{\nabla n}{n}, e > 0.\end{aligned} \tag{9}$$

The definition E from the vector equation (9) is reduced to solving the vector equation

$$\vec{x} = \vec{a} + \left[\vec{b}\vec{x}\right]. \tag{10}$$

From (10)

$$\left(\vec{b}\vec{x}\right) = \left(\vec{b}\vec{a}\right), \vec{x} = \vec{a} + \left[\vec{b}\vec{a}\right] + \left[\vec{b}\left[\vec{b}\vec{x}\right]\right].$$

At $b^2 << 1$,

$$\begin{aligned}&\vec{E} = -\frac{\left[\vec{\vartheta}\vec{H}\right]}{c} - \Lambda'\left[\vec{\nabla} T\vec{H}\right] + \frac{c}{4\pi\sigma} rot\vec{H} - \\ &- \frac{c\sigma'}{4\pi\sigma^2}\left[rot\vec{H}, \vec{H}\right] + \frac{T}{c}\frac{\nabla\rho}{\rho} + \Lambda\nabla T\end{aligned} \tag{11}$$

was obtained.

To obtain expression (11), Maxwell's equation $rot\vec{H} = \frac{4\pi}{c}\vec{j}$ was used. Here $\Lambda = \frac{\alpha}{\sigma}$, $\Lambda' = \frac{\alpha'\sigma - \alpha\sigma'}{\sigma^2}$, σ is the electrical conductivity coefficient, Λ is the differential thermopower, Λ' is the Nerst-Ettinizhausen effect coefficient. Substituting (10) into the equation $\frac{\partial\vec{H}}{\partial e} = -crot\vec{E}$, we obtain an equation containing $\vec{H}$ and $\vec{\nabla} T$. It was proven in [1-2] that at $\vec{k} \perp \vec{H}'$ a thermomagnetic wave with a frequency is excited

$$\omega_T = -c\Lambda'\vec{k}\vec{\nabla}T. \tag{12}$$

In anisotropic media with an electronic type of charge carriers, an increasing thermomagnetic wave is excited under certain conditions. Analytical formulas are found for the frequency and for the increment of this wave. The analytical formulas for the tensor of electrical conductivity of the medium are indicated in the form of a table. A formula is found for the ratios of the temperature gradient [5].

In [6] using the kinetic equation for a nonequilibrium process, analytical values of the critical electric field are obtained without an external magnetic field. The estimate of this critical electric field is consistent with Gunn's experiment in which energy is emitted from the sample.

[7] is proved that in anisotropic conducting media of electric type of charge carriers, different waves of a thermomagnetic nature are excited. With the longitudinal $\vec{k} \parallel \vec{\nabla}T$ and transverse $\vec{k} \perp \vec{\nabla}T$ orientation of the wave vector relative to the temperature gradient, waves of a thermomagnetic nature with different frequencies and increments are excited.

From the conclusions [8], it follows that in anisotropic conducting media, it is possible to excite a number of thermomagnetic waves with frequency frequencies. However, at present, there are no experimental data on thermomagnetic waves in the public domain. In [8] frequency is three times less than the frequency of thermomagnetic waves in plasma (i.e., than the frequency ω_T).

In this theoretical work, we will prove

- to determine the frequencies of thermomagnetic waves, when the wave vector of thermomagnetic waves is directed along the temperature gradient $\vec{k} \parallel \vec{\nabla}T$ (longitudinal wave);

- to prove that at $\vec{k} \parallel \vec{\nabla}T$ (longitudinal wave) and at $\vec{k} \perp \vec{\nabla}T$ (transverse wave) thermomagnetic waves can grow (instability).

The growth rate of the thermomagnetic wave differed significantly at $\vec{k} \parallel \vec{\nabla}T$ and at $\vec{k} \perp \vec{\nabla}T$.

Materials and Methods

In the presence of a temperature gradient and an external magnetic field in an isotropic solid, the total electric field [4] has the form:

$$\vec{E} = \varsigma\vec{j} + \varsigma'\left[j\vec{H}\right] + \varsigma''\left(\vec{j}\vec{H}\right)\vec{H} + \Lambda\frac{\partial T}{\partial x} + \Lambda'\left[\vec{\nabla}T\vec{H}\right] + \Lambda''\left(\vec{\nabla}T\vec{H}\right)\vec{H}.$$

In an anisotropic solid, all coefficients in equation (13) are tensors. Then for an anisotropic solid body (13) will have the form:

$$E_i = \varsigma_{ik} j'_k + \left[j\vec{H}\right]_k j'_{ik} + \varsigma''_{ik}\left(\vec{j}\vec{H}\right)\vec{H}_k + \Lambda_{ik}\frac{\partial T}{\partial x_k} + \Lambda'_{ik}\left[\vec{\nabla}T\vec{H}\right]_k + \Lambda''_{ik}\left(\vec{\nabla}T\vec{H}\right)\vec{H}_k. \tag{14}$$

Here j_{ik} is the tensor of the reciprocal value of the ohmic resistance $\varsigma_{ik} = \frac{1}{\sigma_{ik}}$, Λ_{ik} is the differential thermopower, Λ'_{ik} is the Nerist-Ettinizhausen coefficient [8-9]. We will consider an external magnetic field $\vec{H}_0 = 0$ in an anisotropic solid. Then in equation (14) the terms containing $\varsigma'_{ik}, \varsigma''_{ik}, \Lambda''_{ik}$ equal to zero. Then for our problem the system of equations has the form

$$\begin{aligned} E'_i &= \varsigma_{ik} j'_k + \Lambda'_{ik}\left[\vec{\nabla}TH\right]_k \\ rot\vec{E}' &= -\frac{1}{c}\frac{\partial\vec{H}'}{\partial t} \\ rot\vec{H}' &= \frac{4\pi}{c}\vec{j}' + \frac{1}{c}\frac{\partial\vec{E}'}{\partial t}. \end{aligned} \tag{15}$$

Let us assume that all variables have the character of a monochromatic wave. Then from (15)

$$\begin{aligned} E'_i &= \varsigma_{ik} j'_k + \Lambda'_{ik}\left[\vec{\nabla}TH\right]_k \\ j' &= \frac{ic^2}{4\pi\omega}\left[\vec{k}\left[\vec{k}\vec{E}'\right]\right] + \frac{i\omega}{4\pi}E'_{ik} \end{aligned} \tag{16}$$

was obtained.

From joint solution (16) for the electric field tensor we obtain the equation

$$E_i' = \frac{ic^2}{4\pi\omega}\varsigma_{ik}\left(\vec{k}\vec{E}'\right)K_k + \frac{i\left(\omega^2 - c^2k^2\right)}{4\pi\omega}\varsigma_{ik}E_k' + \\ + \frac{c\Lambda'_{ik}}{\omega}\left(\vec{\nabla}T\vec{E}'\right)K_k - \frac{c\Lambda'_{ik}}{\omega}\left(\vec{k}\vec{\nabla}T\right)E_k' \tag{17}$$

was obtained.

The solution of equation (17) is generally impossible, and therefore we will consider excitations of thermomagnetic waves in both the transverse and longitudinal directions. To determine the direction of the wave vector $\vec{k}$, you need to choose a coordinate system.

Results and Discussion

Transverse thermomagnetic waves $\vec{k} \perp \vec{\nabla}T$

At $\vec{k} \perp \vec{\nabla}T$ coordinate system

$$k_1 \neq 0,\ k_2 = k_3 = 0,\ k_1\frac{\partial T}{\partial x_1} = \left(\vec{k}\vec{\nabla}T\right) = 0,\ \frac{\partial T}{\partial x_2} \neq 0,\ \frac{\partial T}{\partial x_3} = 0\ . \tag{18}$$

With this choice from (17)

$$E_i' = \left(A\varsigma_{il}k_lk_k + B\varsigma_{ik} + \frac{c\Lambda'_{ik}}{\omega}k_l\frac{\partial T}{\partial x_k}\right)E_k' \\ E_i' = \delta_{ik}E_k', \delta_{ik} = \begin{cases}1, at\ i = k\\ 0, at\ i \neq k\end{cases} \\ A = \frac{ic^2}{4\pi\omega}, B = \frac{i\left(\omega^2 - c^2k^2\right)}{4\pi\omega} \tag{19}$$

was obtained.

Let's denote

$$\varphi_{ik} = A\varsigma_{il}k_lk_k + B\varsigma_{ik} + \frac{c\Lambda'_{il}}{\omega}k_l\frac{\partial T}{\partial x_k}. \tag{20}$$

From (19)

$$\varphi_{11} = \frac{i\omega}{4\pi}\varsigma_{11}, \varphi_{12} = i\Omega\varsigma_{12} + \frac{\omega_{12}}{\omega}, \varphi_{13} = i\Omega\varsigma_{13}, \Omega = \frac{\omega^2 - c^2k^2}{4\pi\omega} \\ \varphi_{21} = \frac{i\omega}{4\pi}\varsigma_{21}, \varphi_{22} = i\Omega\varsigma_{22} + \frac{\omega_{22}}{\omega}, \varphi_{23} = i\Omega\varsigma_{23} \\ \varphi_{31} = \frac{i\omega}{4\pi}\varsigma_{31}, \varphi_{32} = i\Omega\varsigma_{32} + \frac{\omega_{32}}{\omega}, \varphi_{33} = i\Omega\varsigma_{33} \tag{21}$$

was obtained.

Substituting (21) into (19), we got follow dispersion equation in tensor form

$$\left|\left(\varphi_{ik} - \delta_{ik}\right)\right| = 0 \tag{22}$$

or

$$\varphi_{31}\varphi_{12}\varphi_{23} + \varphi_{21}\varphi_{32}\varphi_{13} + \\ + \left(\varphi_{11} - 1\right)\left(\varphi_{22} - 1\right)\left(\varphi_{33} - 1\right) - \\ - \varphi_{31}\varphi_{13}\left(\varphi_{22} - 1\right) - \\ - \varphi_{32}\varphi_{23}\left(\varphi_{11} - 1\right) - \varphi_{21}\varphi_{12}\left(\varphi_{33} - 1\right) = 0 \tag{23}$$

was obtained.

Dispersion equation (23) taking into account (21) has the form

$$\sum_{i=1}^{5} u_i \omega_i + u_0 = 0. \tag{24}$$

The fifth degree relative to the purity of vibrations of equation (24) has a very complex form. Simplifying equation (24) requires a lot of mathematical approximations. However, equation (24) is easily simplified depending on the tensor ς_{ik}.

If

$$\begin{aligned} &\varsigma_{12} = \varsigma_{13} = \varsigma_{22} = \varsigma_{23} = \varsigma_{32} = \varsigma_{33} \\ &\varsigma_{11} = \varsigma_{21} = \varsigma_{31}. \end{aligned} \tag{25}$$

The dispersion equation has the form:

$$\begin{aligned} &\frac{1}{2\pi}\left(\frac{i\varsigma_{11}}{2} + \varsigma_{22}\right)\omega^2 + \left[\frac{i\varsigma_{11}}{4\pi}\left(\omega_{13} + \omega_{12} - \omega_{22}\right) - 1\right]\omega + \\ &+ \omega_{22} + \omega_{33} - \frac{ic^2k^2}{2\pi}\varsigma_{22} = 0. \end{aligned} \tag{26}$$

Substituting for frequency

$$\omega = \omega_0 + i\gamma,\ \gamma << \omega_0.$$

We can get from (26) next two equation for definition ω_0 and γ

$$\begin{aligned} &\frac{1}{2\pi}\varsigma\omega_0^2 - \frac{1}{4\pi}\varsigma\omega_0\gamma - \frac{\varsigma}{4\pi}\left(\omega_{13} + \omega_{12} - \omega_{22}\right)\gamma - \\ &- \omega_0 + \omega_{22} + \omega_{33} = 0 \end{aligned} \tag{27}$$

$$\begin{aligned} &\frac{1}{4\pi}\varsigma\omega_0^2 + \frac{1}{2\pi}\varsigma\omega_0\gamma + \frac{\varsigma}{4\pi}\left(\omega_{13} + \omega_{12} - \omega_{22}\right)\omega_0 - \\ &- \gamma - \frac{c^2k^2\varsigma}{2\pi} = 0. \end{aligned} \tag{28}$$

From (28)

$$\gamma = \frac{1}{4\pi}\varsigma\omega_0^2 + \frac{\varsigma}{4\pi}\left(\omega_{13} + \omega_{12} - \omega_{22}\right)\omega_0 - \frac{c^2k^2\varsigma}{2\pi}. \tag{29}$$

Substituting (29) into (27)

$$\begin{aligned} &\frac{1}{2\pi}\varsigma\omega_0^2 - \frac{\varsigma}{4\pi}\left(\omega_{13} + \omega_{12} - \omega_{22}\right)\left[\frac{1}{4\pi}\varsigma\omega_0^2 + \right. \\ &\left. + \frac{\varsigma}{4\pi}\left(\omega_{13} + \omega_{12} - \omega_{22}\right)\omega_0 - \frac{c^2k^2\varsigma}{2\pi}\right] - \\ &- \omega_0 + \omega_{22} + \omega_{33} = 0. \end{aligned} \tag{30}$$

From (30) is shown, at $\omega_{22} = \omega_{13} + \omega_{12}$, $\varsigma = \frac{\pi}{2\left(\omega_{22} + \omega_{33}\right)}$.

Thus, real part of frequency of thermomagnetic wave is

$$\omega_0 = 2\left(\omega_{22} + \omega_{33}\right). \tag{31}$$

Substituting (31) into (29)

$$\gamma = \frac{1}{2}\left(\omega_{22} + \omega_{33}\right) - \frac{1}{2}\frac{c^2k^2}{\omega_{22} + \omega_{33}} \tag{32}$$

was obtained.

From (32) it is shown wave with frequency (31) will rise is

$$\omega_{22} + \omega_{33} >> ck.$$

Longitudinal thermomagnetic wave $\vec{k} \| \vec{\nabla} T$

At condition $\vec{k} \| \vec{\nabla} T$ axis can be chosen like

$$k_1 = k,\ k_2 = k_3 = 0,\ \frac{\partial T}{\partial x_2} = \frac{\partial T}{\partial x_3} = 0, k_1 \frac{\partial T}{\partial x_1} \neq 0\ \ \frac{\partial T}{\partial x_2} \neq 0,\ \frac{\partial T}{\partial x_3} = 0. \tag{33}$$

At this choose, tensors φ_{ik} are

$$\begin{aligned}
&\varphi_{11} = \frac{i\omega}{4\pi}\varsigma_{11}, \varphi_{12} = i\Omega\varsigma_{12} + \frac{\omega_{12}}{\omega}, \varphi_{13} = i\Omega\varsigma_{13} + \frac{\omega_{13}}{\omega} \\
&\varphi_{21} = \frac{i\omega}{4\pi}\varsigma_{21}, \varphi_{22} = i\Omega\varsigma_{22} + \frac{\omega_{22}}{\omega}, \varphi_{23} = i\Omega\varsigma_{23} + \frac{\omega_{23}}{\omega} \\
&\varphi_{31} = \frac{i\omega}{4\pi}\varsigma_{31}, \varphi_{32} = i\Omega\varsigma_{32} + \frac{\omega_{32}}{\omega}, \varphi_{33} = i\Omega\varsigma_{33} + \frac{\omega_{33}}{\omega}.
\end{aligned} \tag{34}$$

Substituting (34) into (23) we got follow dispersion equation

$$\begin{aligned}
&-\frac{i}{64\pi^3}\left(\varsigma_{31}\varsigma_{21}\varsigma_{23} + \varsigma_{31}\varsigma_{13}\varsigma_{32}\right)\omega^4 + -\frac{1}{64\pi^2}\left(\varsigma_{11}\varsigma_{22} + \varsigma_{11}\varsigma_{33}\right)\omega^3 + \\
&+\left[\frac{i}{64\pi^3}\left(\varsigma_{31}\varsigma_{21}\varsigma_{23} + 2\varsigma_{31}\varsigma_{13}\varsigma_{32}\right)c^2k^2 + \frac{i}{4\pi}\left(\varsigma_{11} + \varsigma_{22} + \varsigma_{33}\right) + \right. \\
&\left. + \frac{\omega_{22}}{16\pi^2}\left(\varsigma_{11}\varsigma_{33} + 2\varsigma_{31}\varsigma_{13}\right)\right]\omega^3 + \left[-\frac{1}{64\pi^3}\left(\varsigma_{11}\varsigma_{22} + \varsigma_{11}\varsigma_{33}\right)c^2k^2 - 1 + \right. \\
&\left. + + \frac{i\omega_{22}}{4\pi}\left(\varsigma_{11} - \varsigma_{21}\right)\right]\omega - \frac{ic^2k^2}{4\pi}\left(\frac{1}{64\pi^2}\varsigma_{31}\varsigma_{13}\varsigma_{32}c^2k^2 - \varsigma_{22} - \varsigma_{33}\right) - \\
&-\frac{1}{64\pi^2}\omega_{22}c^2k^2\left(\varsigma_{11}\varsigma_{33} + \varsigma_{13}\varsigma_{31}\right) - \omega_{22} = 0.
\end{aligned} \tag{35}$$

Solving (24) in general is difficult and almost impossible, so we choose the following value. The tensors have the same values in all directions ς_{ik}, then from (35)

$$\begin{aligned}
&x^4 + 16\pi i x^3 + \left(-48\pi^2 + 12\pi i\omega_{22}\varsigma\right)x^2 + \\
&+ 64\pi^3 i\left(-1 + i\frac{\omega_{22}\varsigma}{2\pi}\right)x - \omega_{22}\varsigma = 0 \\
&\omega = ck\varsigma x \\
&ck\varsigma << 1
\end{aligned} \tag{36}$$

was obtained.

Assuming $x = x_0 + ix_1, x_1 << 0$ and separating real and imaginary parts in (36), we got

$$\begin{aligned}
&x_0^4 - 48\pi x_0^2 x_1 - 48\pi^2 x_0^2 - 24\pi\omega_{22}\varsigma x_0 x_1 + \\
&+ 64\pi^3\frac{\omega_{22}\varsigma}{2\pi}x_0 + 64\pi^3 x_1 - \omega_{22}\varsigma = 0
\end{aligned} \tag{37}$$

$$\begin{aligned}
&4x_0^3 x_1 + 16\pi x_0^3 - 96\pi^2 x_0 x_1 + 12\pi\omega_{22}\varsigma x_0^2 - \\
&- 64\pi^3 x_0 - 32\pi^2\omega_{22}\varsigma x_1 = 0.
\end{aligned} \tag{38}$$

From (37-38) it is shown, at $x_0 >> 1$ thermomagnetic wave doesn't exist. Thermomagnetic waves exist at $x_0 << 1$ (26-27)

$$-24\pi\omega_{22}\varsigma x_0 x_1 + 32\pi^2\omega_{22}\varsigma x_0 + 64\pi^3 x_1 - \omega_{22}\varsigma = 0. \tag{39}$$

Then we got

$$-96\pi^2 x_0 x_1 - 64\pi^3 x_0 - 32\pi^2 \omega_{22}\varsigma x_1 = 0. \quad (40)$$

From (40) $x_0 = -\frac{\omega_{22}\varsigma}{2\pi}x_1$, $x_0 < \frac{1}{3\pi}\omega_{22}\varsigma$ was obtained.

Substituting into (39) values of imaginary and real part of the frequency are

$$x_1 = \frac{2\pi}{3}$$
$$\omega_1 = \frac{2\pi}{3}\cdot\frac{1}{\varsigma} \quad (41)$$
$$\omega_0 = -\frac{\omega_{22}}{2\pi}\cdot\frac{2\pi}{3} = -\frac{\omega_{22}}{3}.$$

From (41) it is shown, wave with frequency $\omega_0 = -\frac{\omega_{22}}{3}$ is growing.

$$\frac{\omega_0}{\omega_1} = \frac{\omega_{22}}{3}\cdot\frac{3\varsigma}{2\pi} = \frac{\omega_{22}\varsigma}{2\pi} << 1 \quad (42)$$
$$\omega_{22}\varsigma << 2\pi$$

Conclusion

Thus, thermomagnetic waves with different frequencies are excited in anisotropic conducting media. These waves can be longitudinal $\vec{k} \parallel \vec{\nabla} T$ and transverse $\vec{k} \perp \vec{\nabla} T$. Condition (31) is one of the practically possible conditions for solving systems of equations (27-28) in anisotropic media. The conditions we chose proved that the propagation of thermomagnetic waves significantly depends on the chosen directions. These directions are different for transverse and longitudinal thermomagnetic waves. The characteristic dispersion equations for transverse thermomagnetic waves $\vec{k} \perp \vec{\nabla} T$ (30) and for longitudinal thermomagnetic waves $\vec{k} \parallel \vec{\nabla} T$ (35) under other selected conditions φ and k can change significantly. We studied transverse and longitudinal thermomagnetic waves in specific values of the tensors φ and k. The work theoretically studies the conditions for the excitation of thermomagnetic waves. The excited wave is increasing. The directions of external fields play a significant role in creating growing waves. Thermomagnetic waves are excited in the longitudinal and transverse directions depending on the value of the inverse conductivity tensor and the frequencies of these thermomagnetic waves were calculated in both the longitudinal directions and the transverse directions. The growth increments of these waves are determined. In both cases (longitudinal $\vec{k} \parallel \vec{\nabla} T$ and transverse $\vec{k} \perp \vec{\nabla} T$) the thermomagnetic frequencies are low. With the small value of the electrical conductivity tensor, the frequency of propagation of thermomagnetic waves is different. The theory is constructed at conditions $H_0 = 0$, i.e. without an external magnetic field.

Thus, the excitation of longitudinal $\vec{k} \parallel \vec{\nabla} T$ and transverse $\vec{k} \perp \vec{\nabla} T$ thermomagnetic waves in anisotropic conducting media occurs in selected directions in the media. To experimentally observe thermomagnetic waves, it is sufficient to measure the conductivity of the medium in various directions.

References

1 Chen, Sh., Yang, X., Wu, F., Ma Y., Zhang, G., Yuan, Y., Gui, T., & Ramis, R.E (2023). Electroterminal effects on high-gain magnetized liner inertial fusion. *Plasma Physics and Controlled Fusion*, 63, 115019.

2 Suslov, S.A., Bozhko, A.A., Sidorov, S.A., & Putin, G.F. (2012). Thermomagnetic convective flows in a vertical layer of ferrocolloid: Perturbation energy analysis and experimental study. *Physical Review E - Statistical, Nonlinear, and Soft Matter Physics*, *86*(1), 01630.

3 Muller, M., Dollfus, P., & Schroter, M., (2021) Erratum: 1-D Drift-Diffusion Simulation of Two-Valley Semiconductors and Devices (IEEE Transactions on Electron Devices). *IEEE Transactions on Electron Devices*, 69(10), 5952.

4 Hasanov, E.R., Khalilova, Sh.G., Mansurova, E.O., & Tabatabaei, N.M. (2020). Unstable thermomagnetic waves in anisotropic medium of electronic type of charge carriers. *International Journal on "Technical and Physical Problems of Engineering" (IJTPE) Turkey*, 12, 49–52.

5 Hasanov, E.R., Khalilova, Sh.G., Tagiyeva, Z.A., Hajiyeva, V.M., & Ahadova, S.S. (2021). Excitation of thermomagnetic and recombination waves in impurity with two types of current carriers. *International Journal on "Technical and Physical Problems of Engineering" (IJTPE)*, 13, 57–61.

6 Hasanov, E.R., Khalilova, Sh.G., Mammadova, G.M., & Mansurova, E.O. (2021). Excitation of unstable waves in impurity semiconductors with two types of charge carriers in external electric and weak magnetic fields. *International Journal on "Technical and Physical Problems of Engineering" (IJTPE)*, 13, 94–97.

7 Mains, R.K., El-Gabaly, M.A., & Haddad, G.I. (1985). Finite-difference numerical methods for solving the energy-momentum transport equations in two-valley semiconductors. *Journal of Computational Physics*, *59*(3), 456–467.

8 Mammadova, G.M. (2022). The frequency of current fluctuations In two-valley semiconductors In an external electric and strong magnetic ($\mu h > c$) fields. *Bulletin of the Karaganda University. Physics series*, 4, 65–72.

9 Gurevich L.E. Thermomagnetic Waves And The Excitation Of A Magnetic Field In A Non-Equilibrium Plasma *J. Exptl. Theoret. Phys. (U.S.S.R.)*, 44, 1963, 548–555.

10 Gurevich L.E. & Helmont B.L. Hydrothermomagnetic Waves In Weakly Inhomogeneous Plasma. *JETP*, 46, 1964, 884–901.

Э.Р. Гасанов, Ш.Г. Халилова, Р.К. Мустафаева

Сыртқы магнит өрісі жоқ температура градиенті болған кезде анизотропты өткізгіш ортада көлденең және бойлық термомагниттік толқындардың қозуы

Анизотропты өткізгіш орталарда магнит өрісі мен температура градиентінің әртүрлі бағыттарындағы қозғалған термомагниттік толқындар анизотропты ортаның бағытына айтарлықтай тәуелді. Термомагниттік толқынның жиілігіне байланысты электр өткізгіштік тензорының теориялық есептеулері ғылыми қызығушылық тудырады. Мақалада толқынның жиіліктері табылған, бойлық ($\vec{k} \parallel \vec{\nabla} T$) және көлденең ($\vec{k} \perp \vec{\nabla} T$) бағыттардағы бұл толқындардың жиіліктері мен өсу жылдамдығы сыртқы магнит өрісіне әртүрлі тәуелді болатыны дәлелденді. Авторлар термомагниттік толқындардың қозу жағдайларын теориялық тұрғыдан зерттеді. Үлгіде өсіп келе жатқан толқындардың пайда болуында сыртқы өрістердің бағыты маңызды рөл атқаратыны көрсетілген. Электр өткізгіштік тензорының мәніне байланысты термомагниттік толқындар бойлық (яғни $\vec{k} \parallel \vec{\nabla} T$) және көлденең (яғни $\vec{k} \perp \vec{\nabla} T$) толқындық бағытта қозғалатыны анықталған. Осы термомагниттік толқындардың жиіліктері бойлық және көлденең бағытта да есептелді. Бұл толқындардың өсу жылдамдығы кері электр өткізгіштік тензорының σ_{ik} мәндерімен анықталады. Қозған толқынның табиғаты бойынша негізінен термомагниттік екені дәлелденді. Теориялық тұрғыдан алынған дисперсия теңдеуі тербеліс жиілігіне қатысты алгебралық үлкен қуаттарға ие. Дисперсиялық теңдеудің екі жағдайында (бойлық $\vec{k} \parallel \vec{\nabla} T$ және көлденең $\vec{k} \perp \vec{\nabla} T$ бағыттар) термомагниттік жиіліктер төмен жиілікте болатын мүшелерді қамтиды. Егер электр өткізгіштік тензорының мәні σ_{ik} бірдей болса, термомагниттік толқындардың таралу жиіліктері әртүрлі болатыны дәлелденді. $H_0 = 0$ теориясы сыртқы магнит өрісінсіз құрастырылған. Сыртқы магнит өрісі болған жағдайда термомагниттік толқындардың қозу шарттары және олардың өсу жағдайлары айтарлықтай өзгереді.

Кілт сөздер: жиілік, өсу, термомагниттік толқындар, көлденең толқындар, бойлық толқындар, өсу, электр өткізгіштік тензоры, кері тензор.

Э.Р. Гасанов, Ш.Г. Халилова, Р.К. Мустафаева

Возбуждение поперечных и продольных термомагнитных волн в анизотропных проводящих средах при наличии температурного градиента без внешнего магнитного поля

В анизотропных проводящих средах возбуждаемые термомагнитные волны при различных ориентациях магнитного поля и градиента температуры существенно зависят от направления анизотропной

среды. Научный интерес представляют теоретические расчеты тензора электропроводности σ_{ik} в зависимости от частоты термомагнитной волны. В настоящей статье были найдены частоты термомагнитной волны и доказано, что при продольном ($\vec{k} \parallel \vec{\nabla} T$) и поперечном ($\vec{k} \perp \vec{\nabla} T$) направлениях частоты и скорость роста этих волн по-разному зависят от внешнего магнитного поля. Авторами теоретически исследованы условия возбуждения термомагнитных волн. Указано, что направление внешних полей играет существенную роль в возникновении растущих волн в образце. Показано, что в зависимости от значения тензора электропроводности термомагнитные волны возбуждаются в продольном (то есть $\vec{k} \parallel \vec{\nabla} T$) и поперечном (то есть $\vec{k} \perp \vec{\nabla} T$) направлениях волны. Рассчитаны частоты этих термомагнитных волн как в продольном, так и в поперечном направлении. Скорость роста этих волн определяется значениями обратного тензора электропроводности σ_{ik} . Доказано, что возбуждаемая волна имеет преимущественно термомагнитную природу. Теоретически полученное дисперсионное уравнение имеет алгебраически большие степени относительно частоты колебания. Дисперсионное уравнение в обоих случаях (продольном $\vec{k} \parallel \vec{\nabla} T$ и поперечном $\vec{k} \perp \vec{\nabla} T$ направлениях) содержит члены, в которых присутствуют термомагнитные частоты в низкой степени частоты. Доказано, что если значение тензора электропроводности σ_{ik} одинаковое, то частоты распространения термомагнитных волн различны. Теория построена без внешнего магнитного поля $H_0 = 0$. При наличии внешнего магнитного поля условия возбуждения термомагнитных волн и, конечно, условия их роста существенно меняются.

Ключевые слова: частота, приращение, термомагнитные волны, поперечные волны, продольные волны, рост, тензор электропроводности, обратный тензор.

Information about authors

Hasanov, Eldar — PhD, Associate Professor, Department of Solid State Physics, Baku State University Physics, Leader of Department of Encyclopedia and Terminology, Institute of Physics, Baku, Azerbaijan; e-mail: egasanov065@gmail.com; ORCID ID: https://orcid.org/0009-0009-6900-6148;

Khalilova, Shahla (contact person) — PhD. Leading researcher of Department of Encyclopedia and Terminology, Institute of Physics, Baku, Azerbaijan; e-mail: shahlaganbarova@gmail.com; ORCID ID: https://orcid.org/0000-0002-1032-2746;

Mustafayeva, Ruhiyye — PhD, teacher, Department of Solid State Physics, Baku State University, Baku, Azerbaijan; e-mail: ruhi-qrk@mail.ru; ORCID ID: https://orcid.org/0009-0005-2342-5399

Article

Received: 31.12.2024
Accepted: 04.04.2024

UDC 621.548.9

https://doi.org/10.31489/2024PH2/53-64

A.N. Dyusembaeva[1,2], N.K. Tanasheva[1,2], A.Zh. Tleubergenova[1,2], A.R. Bakhtybekova[1,2*], Zh.B. Kutumova[1], A.R. Tussuphanova[1,2], N.T. Abdirova[1]

[1]Karaganda Buketov University, Karaganda, Kazakhstan;
[2]Scientific Center "Alternative Energy", Karaganda, Kazakhstan
**(Corresponding author's e-mail:asem.alibekova@inbox.ru)*

Optimal choice of the geometric shape rotor blade wind turbine using the numerical method

To increase the energy efficiency of wind turbines, it is necessary to optimize and improve the shape and size of power elements. In this work, in order to improve the output energy indicators, as well as increase the lifting force, a combined blade in the form of a rotating cylinder and a fixed blade was created and numerically studied. The novelty of the work lies in obtaining the results of the influence of a fixed angle of inclination of the blade on the overall aerodynamic characteristics of the entire combined blade at wind speeds from 3 to 12 m/s. Based on three-dimensional modeling, 4 variants of the combined blade with different angles of location are designed. Three-dimensional patterns of the distribution of velocity vectors and pressure fields are obtained. Linear graphs of the dependence of aerodynamic coefficients on the Reynolds number are shown. It was found that at an angle of 0 degrees, the combined blade has a maximum lift coefficient of 10 and a minimum drag coefficient of 4.5 at Reynolds $1 \cdot 10^4$. The numerical results obtained will be useful in the development of wind power plants with combined blades operating on the basis of Magnus.

Keywords: wind turbine, combined blade, cylinder, Magnus effect, geometric shape, aerodynamic force, three-dimensional modeling, Reynolds number.

Introduction

When designing and creating a wind turbine, the main goal is to achieve maximum output power under specified atmospheric weather conditions. From a physical point of view, this is achieved by creating blades with optimal parameters and shapes. Changing the shape and linear dimensions of the blades affects the aerodynamic coefficients of a blade wind turbine. In the making of the blade, about 15–20% of the total cost of production of a wind turbine is spent. Nevertheless, the profit received from improving the structural model of the blade is tangible [1-2].

The selection and finding of a suitable blade shape and its material is a difficult task because the mathematical description of aerodynamic behavior is a complex process and requires several actions.

Currently, there are 3 types of wind turbine design (Fig. 1).

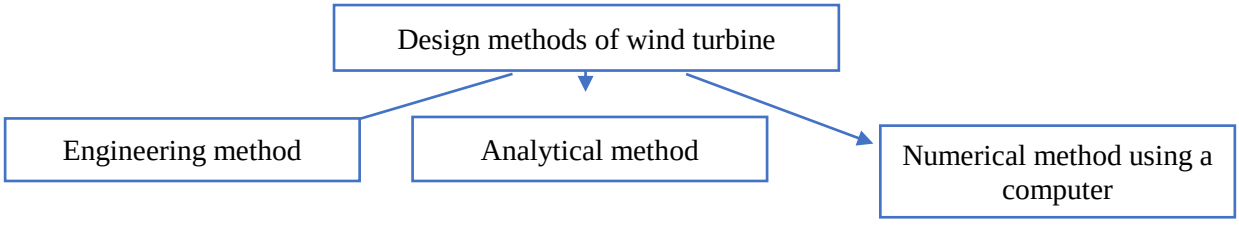

Figure 1. Design methods of wind turbine

Figure 1 shows that the first and third methods are often used in engineering practice when creating elements and wind turbines themselves. The analytical method can determine the characteristics of wind turbines, such as torque, shaft power, etc. The engineering method allows you to create a wind turbine with the best electrical characteristics. A numerical method can be used to obtain a picture of the airflow around wind turbines.

One of the most popular wind turbines in the world is the blade wind turbine. Nevertheless, in addition to the undeniable benefits, the wind generator has a major disadvantage in the form of a direction to the

wind. Designers and producers purposely hide this fact from consumers and only inform them about the benefits of the setup. But in practice, it turns out this way: the power of the wind turbine is defined on the basis that the wind direction always corresponds to the axis of rotation of the wind turbine, that is, the wind blows directly on the calculated surface of the blade. As a result, the calculated power of the wind turbine is received but in real life, the wind direction is not known to be constant [3].

Another type of wind turbine is installed with cylindrical blades, working based on the Magnus effect. Compared with vane wind turbines, these installations have the advantage of generating energy at low wind speeds ranging from 2-3 m/s, and there is no need for wind orientation. Thanks to the cylindrical blades, the wind potential of the air is captured, both from the windward side and the windward side, so there is no need for orientation in the wind direction [4].

The work's authors [5] modified the blade, which is a combination of blades in which an ordinary model in the shape of a circle is combined with a concave elliptical model. It was found that thanks to the combined blade, the power factor of the wind turbine (C max) increases to 11%, thereby improving the characteristics of the wind turbine.

It was determined in the work that after a certain length of the separation plate, a secondary vortex appears on the tail edge. It is determined that the rotation of the vortex is opposite to the main vortex and affects the formation of the primary vortex, as well as the formation of the shear layer [6]. However, these studies were conducted at low Reynolds numbers equal to 485.

The authors also found [7] that the longer the plate, a large value of the initial jump velocity is observed, the reason for this is a jump in the amplitude of vibration and fluctuations in lift. With the introduction of an upstream plate, boundary layers are formed along the plate before attaching to the surface of the cylinder.

In the work, the authors [8] investigated a cylinder equipped with three different separation plates and capable of oscillating across the incoming flow, with a range of Reynolds numbers from 1,500 to 16,000. The conducted studies confirm that the transverse jump mechanism is responsible for bringing cylinders with separation plates into high-amplitude vibrations.

The work [9] is devoted to the experimental study of the aerodynamic characteristics of round cylinders with small end plates and elongation in the critical range of Reynolds numbers. However, it is necessary to perform numerical control of the two-dimensional flow in the subcritical range.

Also, many works are devoted to the numerical study of cylinders of various shapes, such as square, rectangular and triangular [10–12]. In [13], the proposed approach allows us to quantitatively study the unsteady behavior of lifting force on vertical bodies with a complex shape.

Nevertheless, many works are devoted to the study of the flow around a cylinder with a plate, with the influence of the length and width of the plate [14–16]. But the works devoted to the study of the angle of the plate relative to the circular rotating cylinder at high Reynolds numbers are not enough.

Based on this, using design methods, the creation of a combined blade containing a cylinder and a traditional fixed blade, thereby combining two lifting forces, a fixed and cylindrical blade, and reducing the dependence of the cylinder rotation speed on wind speed, with subsequent investigation of the influence of the plate angular arrangement is an urgent issue [17–20].

There are known data on the effect of the relative length of the cylinder on the values of lift and drag. It is established that with the transverse flow of the cylinders, the influence of cylinder elongation on the coefficient of drag and lift is sufficiently exerted [17]. In this paper by the authors [18-19], if L/D=40, the value of the aerodynamic coefficient differs by 18% from the date of the infinite cylinder. Based on this, it can be concluded that to design optimal blade sizes, it is necessary to select optimal values of the length and diameter of the cylinder, and the angle of the fixed blade, based on previous work.

This article presents the results of a numerical study, focusing on the representation of aerodynamic coefficients depending on the Reynolds number and wind speed for 4 variants of the fixed blade relative to the cylinder.

The aim of the work is to conduct a numerical study of a combined blade containing a rotating cylinder and a fixed blade.

In accordance with the purpose of the study, the following tasks are formulated:

– development and creation of 4 versions of blades with tilt angles of 0, 30, 45 and 60 degrees;

– creation of computational domains with the setting of boundary conditions;

– obtaining the results of the pressure distribution fields and velocity vectors around the studied layout;

– obtaining dependencies of aerodynamic coefficients on the Reynolds number.

Geometry features

Based on the existing works of well-known authors and engineers, 4 numerical models of blades with different angles of fixed blade arrangements were created using numerical modeling (Fig. 2). Focusing on the highly effective results of the well-known works of such several authors as N.K.Tanasheva and Dyusembaeva [19, 21-22], an optimal cylindrical blade with a diameter of 50 mm and a length of 300 mm was created. The width of the fixed blade was 33 mm, and the length was 300 mm.

A numerical simulation was carried out to find the optimal angle of the fixed blade relative to the cylinder in the ANSYS WORKBENCH software. Using the three-dimensional modeling system, 4 variants of blades with angles of 0, 30, 45, and 60 degrees were designed. The airflow velocity varied from 3 to 12 m/s [19].

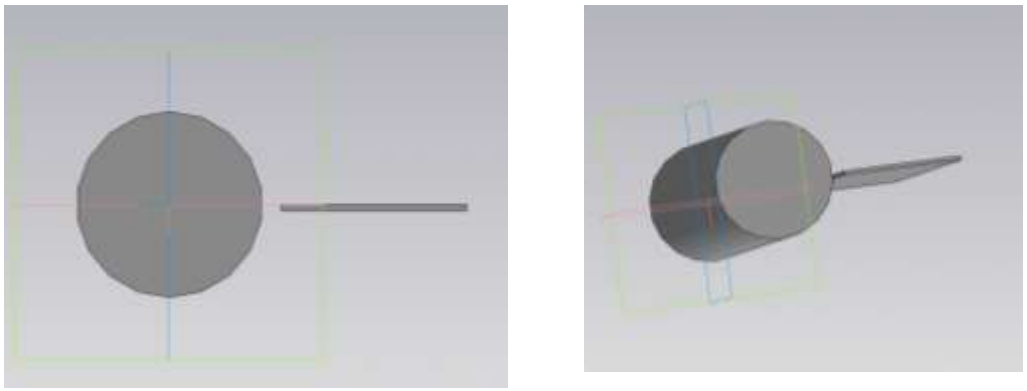

a) 0 degree

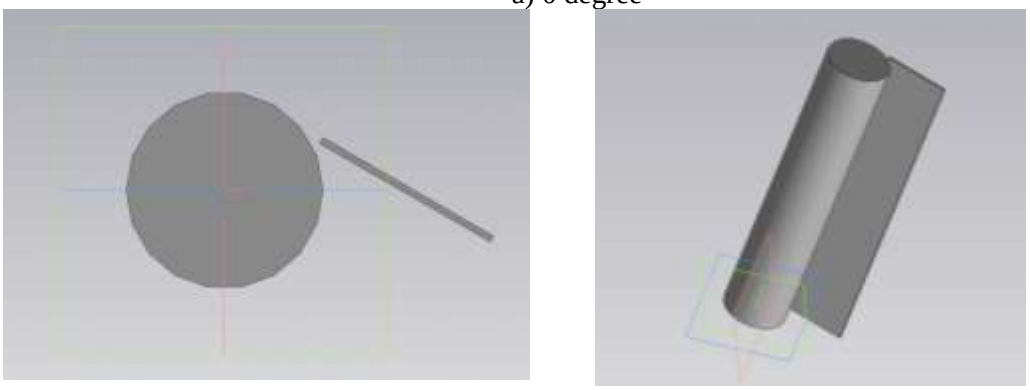

b) 30 degree

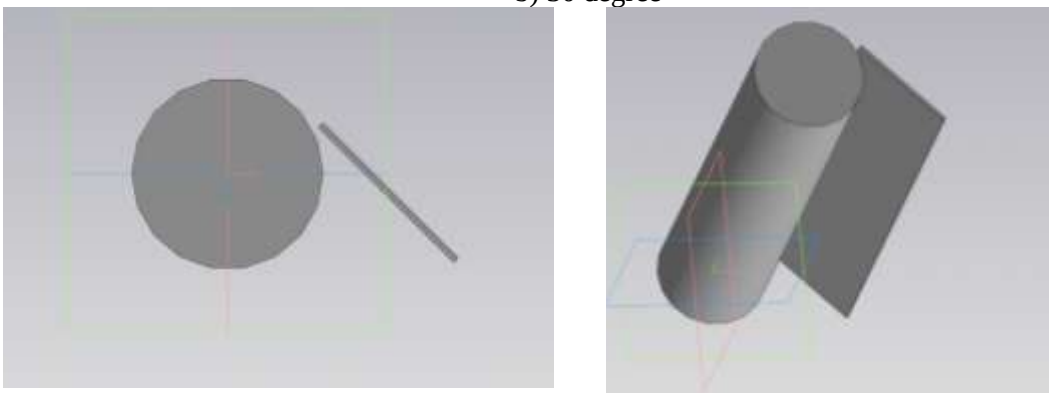

c) 45 degree

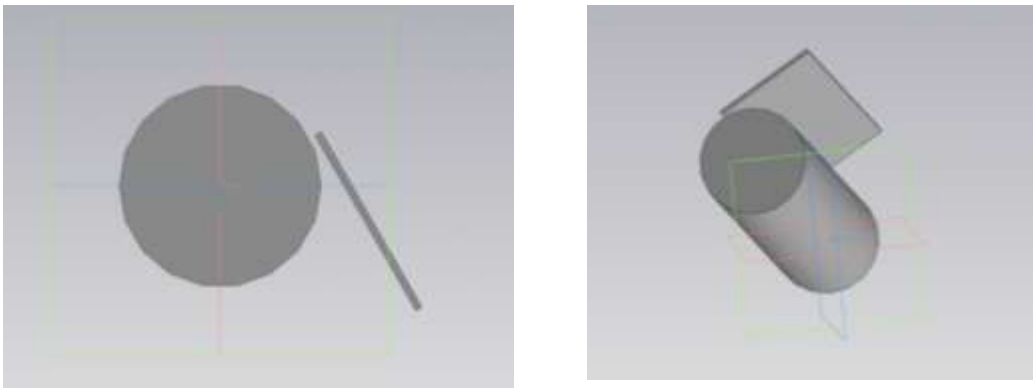

d) 60 degree

Figure 2. Options for the location of the fixed blade relative to the cylinder

Numerical study

Computing area

The authors used a method for modeling turbulent flows based on solving averaged Navier Stokes equations (RANS).

With the help of the Enclosure program, a cylindrical computational subdomain was created around the combined blade, with a radius of 0.05 m to set the rotation conditions around the y-axis. To set the boundary conditions around the swept space, a subdomain was created that simulates a wind tunnel in the form of a parallelepiped with dimensions of 1m; 1m; 1.5 m; 1;1;2 m minus the cylindrical subdomain [19] (Fig. 3).

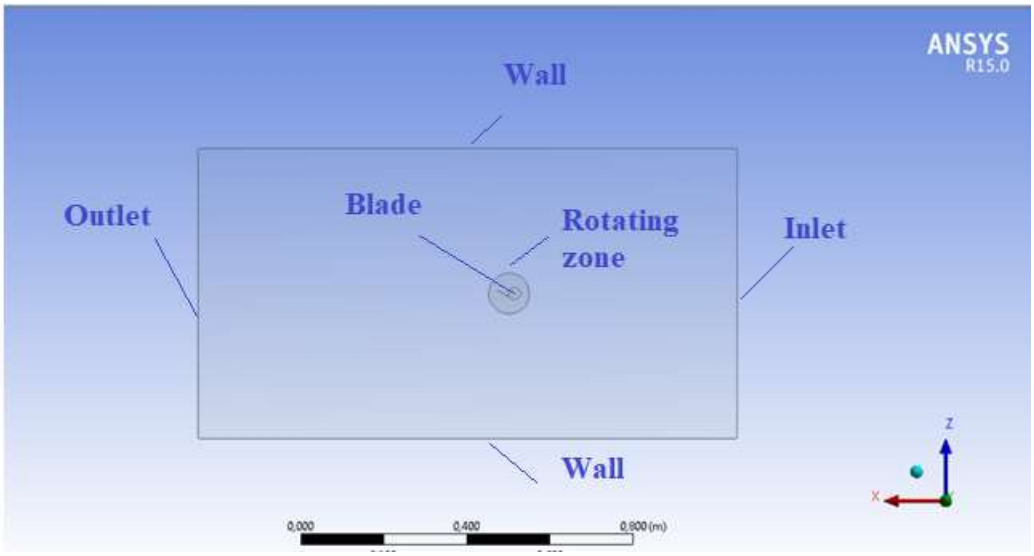

Figure 3. Calculation area

Boundary conditions

The following boundary conditions were used in the model [19]:

Wall (no-slip). The boundary conditions of the wall (BC) are used to bind the liquid and the solid area. In our case, it will be the surface of the blade and atmospheric air.

The speed at the entrance. It is used to determine the set airflow velocity, and it will (3, 5, 7, 10, 12 m/s) together with all the corresponding scalar properties of the flow, as a turbulent model at the entrance to the flow. The total pressure is not fixed but will rise to any value necessary to ensure the necessary velocity distribution.

Rotation of the blade. Is a periodic boundary condition, and is equal to 300, 500, and 700 rpm.

Turbulence model

The problem was solved in a stationary setting. To solve the problem of computer modeling, three-dimensional Reynolds-averaged Navier-Stokes equations were numerically integrated. To close the

equations of motion, the Realizable k-ε turbulence model, which proved itself well on a wide class of problems, was taken, and a viscous incompressible gas (air) was used as a working medium.

Aerodynamic coefficients

An indicator of the efficiency of an aerodynamic element is the aerodynamic coefficients. Using formulas (1) and (2), the aerodynamic coefficients are calculated by numerical method [4].

The drag coefficient is calculated by the formula (1):

$$C_x = \frac{2F_x}{\rho u^2 S}. \quad (1)$$

The lift coefficient is calculated by the formula (2):

$$C_y = \frac{2F_y}{\rho u^2 S}, \quad (2)$$

where, F_x is the drag force, H; F_y — lifting force, H; ρ — air density, kg/m^3; u — flow rate, m/s; S — the area of the midsection, m^2.

Results and Discussion

As a result of numerical simulation, the results of the distribution pattern of velocity vectors around the combined blade at u =7 m/s, n=500 rpm are obtained (Fig. 4).

In the upper left corner, there is a color gradation from blue (minimum) to red (maximum), which is a panel of symbols.

From Figure 4 defined, the angle of inclination of the fixed blade has a great influence on the overall picture of the time-averaged velocity vectors. As the angle of inclination of the blade increases, the turbulence between the cylinder and the blade increases. The so-called closed space is created, which, with increasing angle, becomes more closed and gives more resistance when flowing around the airflow. It is determined that when the fixed blade is positioned at an angle of 0 degrees to the cylinder, a maximum flow velocity of about 11.71 m/ s is observed, which is an assumption about the most effective location of the fixed blade.

Figure 5 shows the results of the static pressure distribution field ($p_{st} = p - p_{atm}$) around the combined blade at u =7 m/s, n=500 rpm.

From the Figure 5 defined, when the angle of the fixed blade is 0 degrees, the so-called additional repulsion of the entire combined blade occurs, due to the formation of high pressure behind the fixed blade. Thus, an additional lifting force of the most stationary blade is formed.

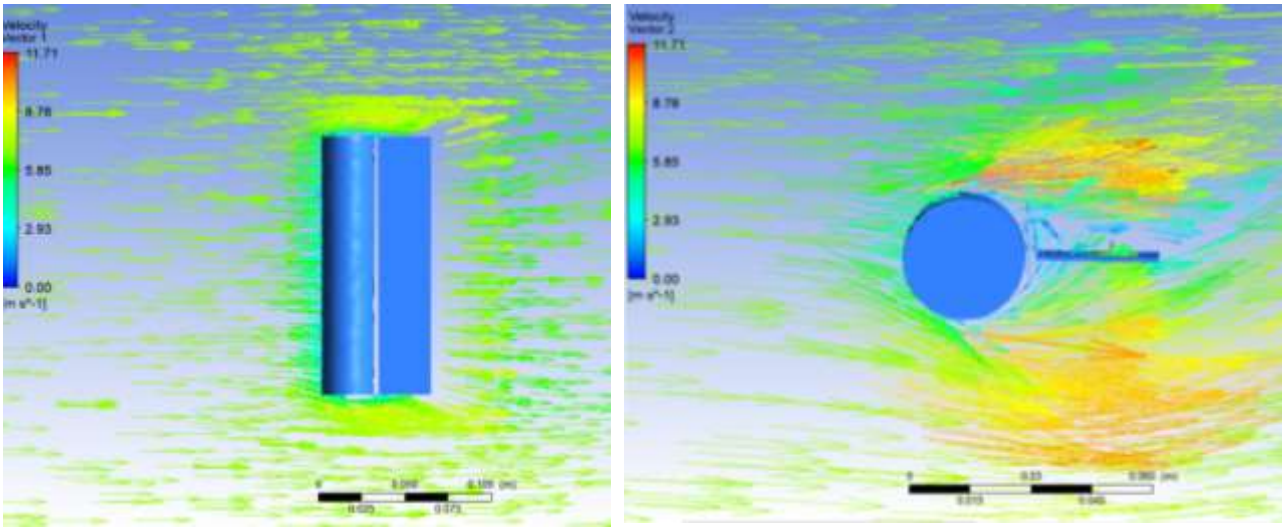

a) 0 degrees

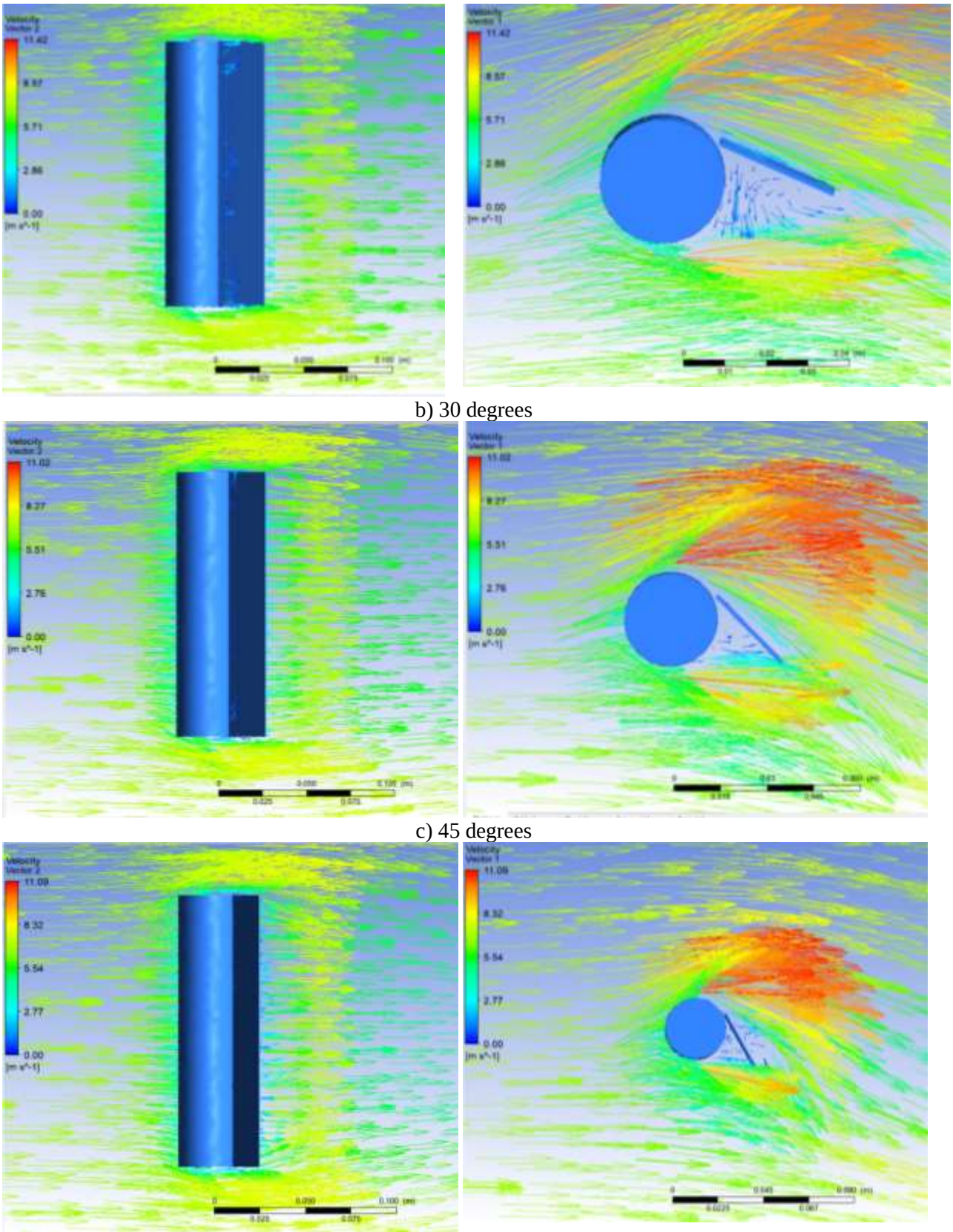

b) 30 degrees

c) 45 degrees

d) 60 degrees

Figure 4. Time-averaged velocity vectors around the combined blade at u =7 m/s, n=500 rpm

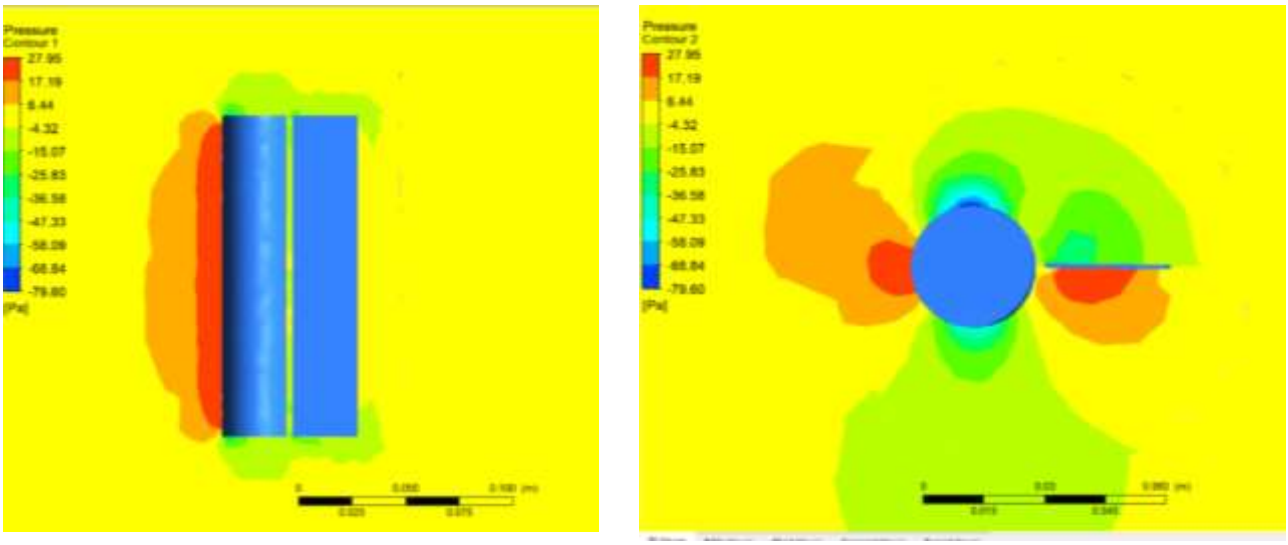

0 degrees

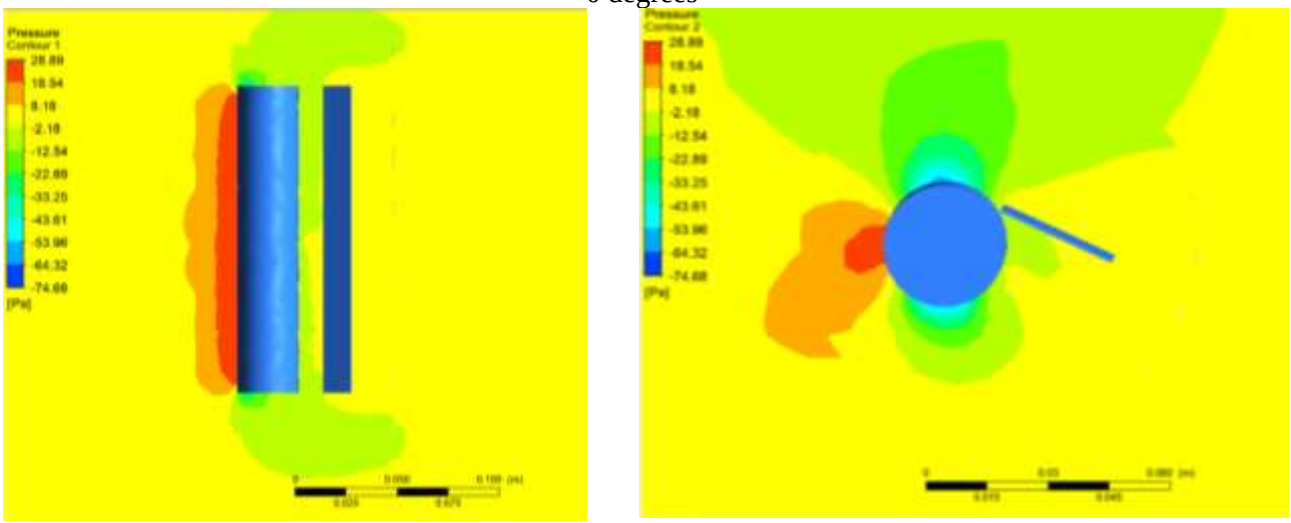

30 degrees

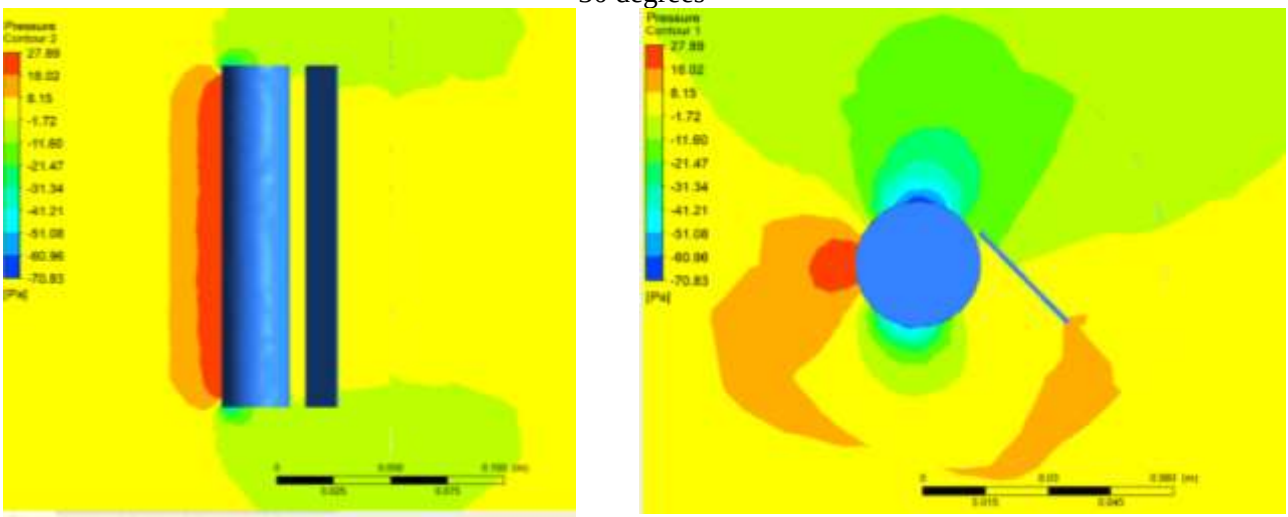

45 degrees

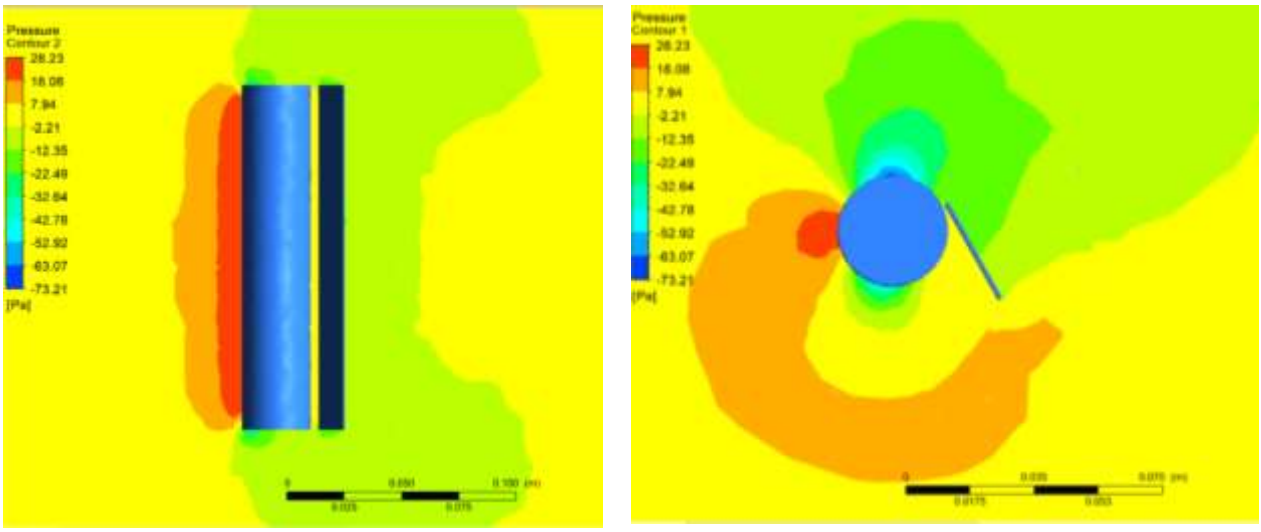

60 degrees

Figure 5. Pressure fields around the combined blade at u =7 m/s, n=500 rpm

Figures 6 and 7 present the results of the numerical calculation of the lift coefficient and drag force from the Reynolds number for various variants of the fixed blade relative to the cylinder.

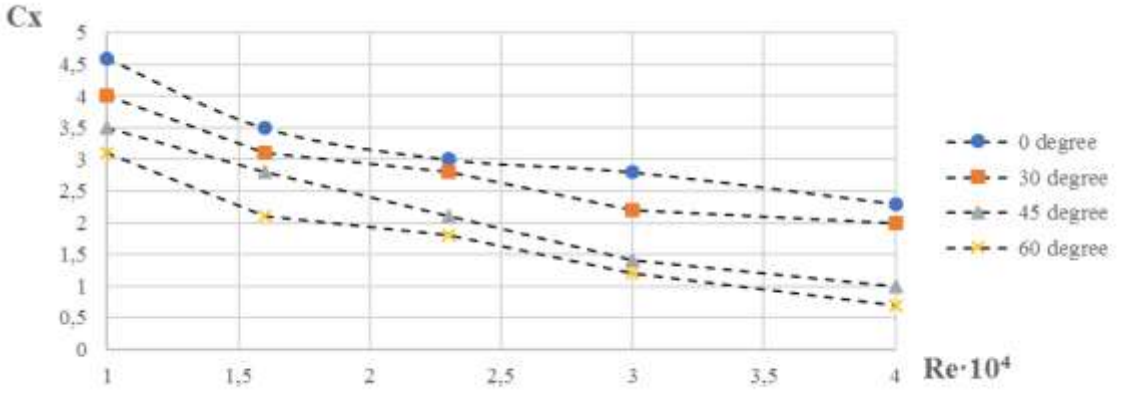

Figure 6. Line graph showing the change in drag coefficient from Reynolds

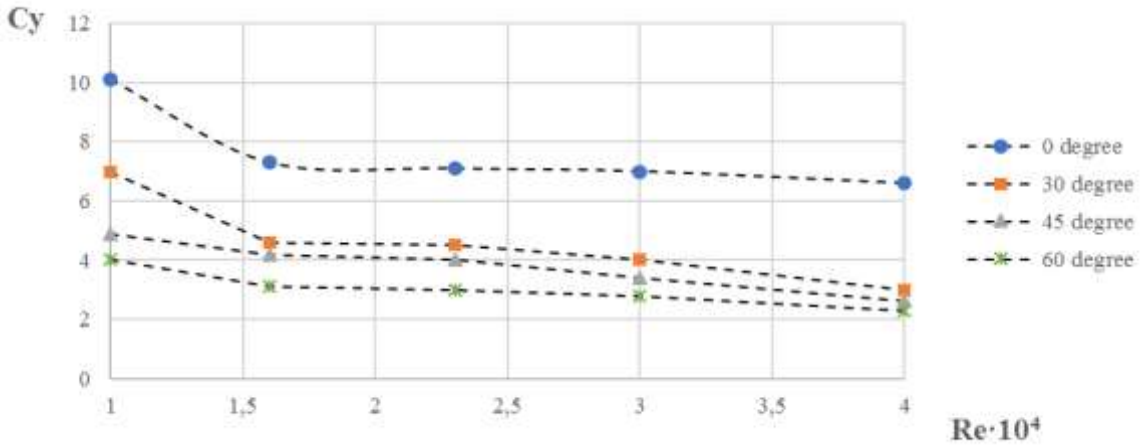

Figure 7. Line graph showing the change in lift coefficient from Reynolds

From the Figures 6 and 7 it is set, when the fixed blade is positioned relative to the cylinder at 0 degrees, the optimal values of the lift and drag coefficients are obtained: 10 and 4.5 with a Reynolds number of $1 \cdot 10^4$. Compared with the other three samples at 30^0, 45^0 and 60^0, at 0^0, the combined blade produces maximum lift and minimum drag force. Compared with the experimental results of cylinders of different shapes (with a porous surface, with a deflector) [21-22] the obtained numerical data of the lift coefficient is almost 2 times higher, which makes it possible to assert that a combined blade is much more efficient than a single cylindrical blade and a blade from a cylinder with a deflector. Below is the dependence of the number of revolutions of the blade on the wind speed at different angles of attack (Fig. 8).

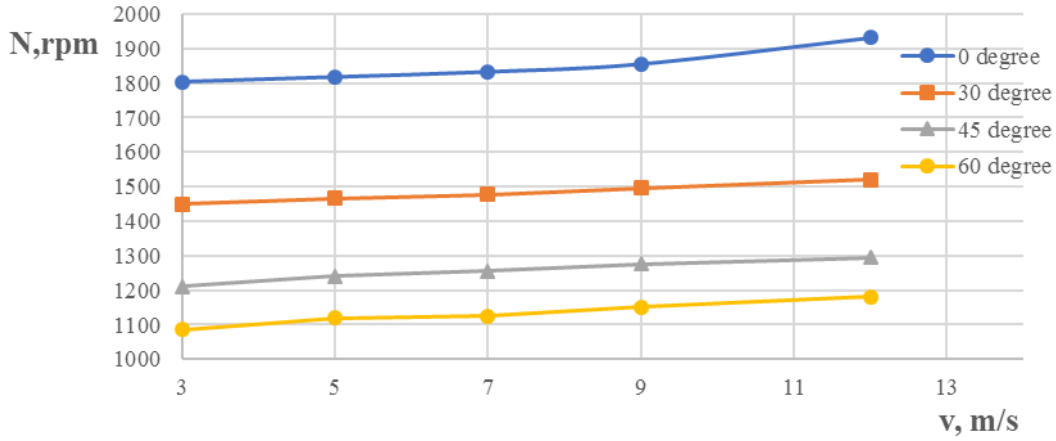

Figure 8. Dependence of rotation speed on wind speed

As can be seen from Figure 8, the number of revolutions of the combined blade is much higher than the number of revolutions of a single cylinder, this is because, during its rotation, the blade carries away adjacent layers of air as a result, the surrounding air receives, in addition to translational motion, rotation around the cylinder, thereby increasing the number of revolutions of rotation.

Conclusion

The authors of the article conducted numerical studies using the ANSYS program to determine the optimal location of the fixed blade to the cylinder.

Based on the conducted numerical research:

- the geometry of the combined blade with different angles of the fixed blade: 0º; 30º; 45º and 60º have been created. The Realizable k-ε model was used as a turbulence model. The flow rate varied from 3–12 m/s;
- three-dimensional pictures of the velocity distribution and the static pressure field around the blade are obtained. It is established that with an increase in the angle of the fixed blade, the turbulence between the cylinder and the blade increases. It is determined that as the angle increases, the pressure in the space between the cylinder and the blade disappears, which is also an additional lifting force;
- from the dependence of the coefficient of lift and drag force on the Reynolds number, it was found that at an angle of 0 ° degrees, there is a maximum lifting force of 10 and a minimum drag force of 4.5 at Re $= 1 \cdot 10^4$.
- It is established that at a wind speed of 12 m/s and an angle of attack of 0 degrees, the number of revolutions of the blade is 1932 rpm.
- It was found that with the angle of the fixed blade 0 ° degrees, the indicators of the entire combined blade are the most effective.

Acknowledgments

The work was carried out with the financial support of the Science Committee of the Ministry of Science and Higher Education of the Republic of Kazakhstan (IRN AP14972704 “Numerical study of a new design of wind turbine blades with a horizontal axis of rotation”).

References

1 Jureczko, M., Pawlak, M., & Mężyk, A. (2005). Optimization of wind turbine blades. *Journal of materials processing technology, 167*(2-3), 463–471.

2 Balat, M. (2009). A review of modern wind turbine technology. *Energy Sources, Part A, 31*(17), 1561–1572.

3 Saad, M.M.M., & Asmuin, N. (2014). Comparison of horizontal axis wind turbines and vertical axis wind turbines. *IOSR Journal of Engineering (IOSRJEN), 4*(08), 27–30.

4 Tanasheva, N.K., Bakhtybekova, A.R., Shaimerdenova, G.S., Sakipova, S.E., & Shuyushbaeva, N. (2022). Modeling aerodynamic characteristics of a wind energy installation with rotating cylinder blades on the basis of the ansys suite. *Journal of Engineering Physics and Thermophysics, 95*(2), 457–463.

5 Sanusi, A., Soeparman, S., Wahyudi, S., & Yuliati, L. (2016). Experimental study of combined blade savonius wind turbine. *International Journal of Renewable Energy Research (IJRER), 6*(2), 614–619.

6 Chauhan, M.K., Dutta, S., More, B.S., & Gandhi, B.K. (2018). Experimental investigation of flow over a square cylinder with an attached splitter plate at intermediate Reynolds number. *Journal of Fluids and Structures, 76*, 319–335.

7 Zhu, H., Li, G., & Wang, J. (2020). Flow-induced vibration of a circular cylinder with splitter plates placed upstream and downstream individually and simultaneously. *Applied Ocean Research, 97*, 102084.

8 Assi, G.R.S., & Bearman, P.W. (2015). Transverse galloping of circular cylinders fitted with solid and slotted splitter plates. *Journal of Fluids and Structures, 54*, 263–280.

9 Zeng, L., Zhao, F., Wang, H., Liu, Y., & Tang, H. (2023). Control of flow-induced vibration of a circular cylinder using a splitter plate. *Physics of Fluids, 35*(8).

10 Wu, B., Li, S., Li, K., & Zhang, L. (2020). Numerical and experimental studies on the aerodynamics of a 5: 1 rectangular cylinder at angles of attack. *Journal of Wind Engineering and Industrial Aerodynamics, 199*, 104097.

11 Neelapu, T.R., Neelapu, K.A., & Kumar, S.A. (2022). Influence of Wake Splitter Plate on Flow Over a Triangular Cylinder at a Low Reynolds Number: A Numerical Study. In *Biennial International Conference on Future Learning Aspects of Mechanical Engineering* (pp. 517–527). Singapore: Springer Nature Singapore.

12 An, B., Bergadà, J.M., Mellibovsky, F., Sang, W.M., & Xi, C. (2020). Numerical investigation on the flow around a square cylinder with an upstream splitter plate at low Reynolds numbers. *Meccanica, 55*, 1037–1059.

13 Li, S., Li, M., Wu, B., Li, K., & Yang, Y. (2023). Three-dimensional aerodynamic lift on a rectangular cylinder in turbulent flow at an angle of attack. *Journal of Fluids and Structures, 118*, 103859.

14 Pfister, J.L., & Marquet, O. (2020). Fluid–structure stability analyses and nonlinear dynamics of flexible splitter plates interacting with a circular cylinder flow. *Journal of Fluid Mechanics, 896*, A24.

15 Sun, X., Suh, C.S., Ye, Z.H., & Yu, B. (2020). Dynamics of a circular cylinder with an attached splitter plate in laminar flow: A transition from vortex-induced vibration to galloping. *Physics of Fluids, 32*(2).

16 Sharma, K.R. & Dutta, S. (2020). Flow control over a square cylinder using attached rigid and flexible splitter plate at intermediate flow regime. *Physics of Fluids, 32*(1).

17 Zhu, H., Chen, Q., Tang, T., Alam, M.M., & Zhou, T. (2023). Flow structures around a circular cylinder with bilateral splitter plates and their dynamic characteristics. *Ocean Engineering, 269*, 113547.

18 Tanasheva, N.K., Bakhtybekova, A.R., Shuyushbayeva, N.N., Tussupbekova, A.K., & Tleubergenova, A.Z. (2022). Calculation of the aerodynamic characteristics of a wind-power plant with blades in the form of rotating cylinders. *Technical Physics Letters, 48*(2), 51–54.

19 Dyusembaeva, A.N., Tleubergenova, A.Z., Tanasheva, N.K., Nussupbekov, B.R., Bakhtybekova, A.R., & Kyzdarbekova, S.S. (2023). Numerical investigation of the flow around a rotating cylinder with a plate under the subcritical regime of the Reynolds number. *International Journal of Green Energy*, 1–15.

20 Oh, G., Park, H., & Choi, J.I. (2022). Drag, lift, and torque coefficients for various geometrical configurations of elliptic cylinder under Stokes to laminar flow regimes. *AIP Advances, 12*(6).

21 Tanasheva, N.K., Shuyushbayeva, N.N., & Mussenova, E.K. (2018). Studying the dependence of the aerodynamic characteristics of rotating cylinders on the rake angle of air flow. *Technical Physics Letters, 44*, 787–789.

22 Bakhtybekova, A.R., Tanasheva, N.K., Minkov, L.L., Shuyushbayeva, N.N., & Dyusembaeva, A.N. (2022). Aerodynamic features of a rotating cylinder with a deflector. *Journal of Applied Mechanics and Technical Physics, 63*(5), 833–842.

А.Н. Дюсембаева, Н.К. Танашева, А.Ж. Тлеубергенова, А.Р. Бахтыбекова,
Ж.Б. Кутумова, А.Р. Тусупханова, Н.Т. Абдирова

Сандық әдісті қолдана отырып жел энергетикалық қондырғысының ротор қалақшасының геометриялық пішінін оңтайлы таңдау

Жел турбиналарының энергия тиімділігін арттыру үшін қалақтар түріндегі күштік элементтерінің пішіні мен өлшемдерін оңтайландыру және жақсарту қажет. Жұмыста алынған энергетикалық және шығу көрсеткіштерін жақсарту және үлкейту, сондай-ақ көтеру күшін арттыру мақсатында айналмалы

цилиндр және қозғалмайтын қалақша түріндегі құрамалы қалақша жасалды және сандық түрде зерттелді. Жұмыстың жаңалығы 3-тен 12 м/с-қа дейінгі ауа ағынының жылдамдығы кезінде барлық біріктірілген қалақтың (цилиндр және қозғалмайтын қалақша) жалпы аэродинамикалық сипаттамаларына көлбеу бекітілген қалақ бұрышының әсерінің сандық нәтижелерінің алынуында. Үш өлшемді сандық модельдеу негізінде қозғалмайтын қалақшаның әртүрлі орналасу бұрыштары бар құрамалы қалақшаның 4 нұсқасы жобаланған. Турбуленттілік моделі ретінде *Realizible k-ε* моделі қолданылды, ол есептердің кең класында өзін дәлелдеді, ал жұмыс ортасы ретінде тұтқыр сығылмайтын газ (ауа) қолданылды. Жылдамдық векторлары мен қысым өрістерінің таралуының үш өлшемді суреттері алынды. Нәтижелерден қозғалмайтын қалақша 0° бұрышта орналасқан кезде құйындылардың ең аз түзілуі байқалатыны айқындалды. Аэродинамикалық коэффициенттердің Рейнольдс санына тәуелділігінің сызықтық графиктері көрсетілген. 0 градус бұрыш кезінде құрамалы қалақшаның ең жоғары көтеру күшінің коэффициенті 10 және Рейнольдс $1 \cdot 10^4$ кезінде ең төмен маңдайлық кедергі коэффициенті 4,5 болатыны анықталды. Алынған сандық нәтижелер Магнус эффектісі негізінде жұмыс істейтін құрамалы қалақшалары бар жел энергетикалық қондырғыларын әзірлеуде пайдалы болады.

Кілт сөздер: жел энергетикалық қондырғы, құрамалы қалақша, цилиндр, Магнус эффектісі, геометриялық пішін, аэродинамикалық күш, үш өлшемді модельдеу, Рейнольдс саны.

А.Н. Дюсембаева, Н.К. Танашева, А.Ж. Тлеубергенова, А.Р. Бахтыбекова, Ж.Б. Кутумова, А.Р. Тусупханова, Н.Т. Абдирова

Оптимальный выбор геометрической формы лопасти ротора ветроэнергетической установки с использованием численного метода

Для повышения энергоэффективности ветряных турбин необходимо оптимизировать и улучшить форму и размеры силовых элементов в виде лопастей. В данной работе с целью улучшения и увеличения получаемых энергетических и выходных показателей, а также роста подъемной силы была создана и численно исследована комбинированная лопасть в виде вращающегося цилиндра и неподвижной лопасти. Новизна работы заключается в получении численных результатов влияния фиксированного угла наклона лопасти на общие аэродинамические характеристики всей комбинированной лопасти (цилиндра и неподвижной лопасти) при скоростях воздушного набегающего потока от 3 до 12 м/с. На основе трехмерного численного моделирования спроектированы 4 варианта комбинированной лопасти с разными углами расположения неподвижной лопасти. В качестве модели турбулентности использовалась *Realizible k-ε* модель, которая хорошо зарекомендовала себя в широком классе задач, и в качестве рабочей среды использовался вязкий несжимаемый газ (воздух). Получены трехмерные картины распределения векторов скорости и полей давления. Из результатов установлено, что при расположении неподвижной лопасти под углом 0° наблюдается наименьшее образование вихрей. Показаны линейные графики зависимости аэродинамических коэффициентов от числа Рейнольдса. Было обнаружено, что при угле 0 градусов комбинированная лопасть имеет максимальный коэффициент подъемной силы 10 и минимальный коэффициент лобового сопротивления 4,5 при Рейнольдсе $1 \cdot 10^4$. Полученные численные результаты будут полезны при разработке и создании ветроэнергетических установок с комбинированными лопастями, работающих на основе Магнус.

Ключевые слова: ветроэнергетическая установка, комбинированная лопасть, цилиндр, эффект Магнуса, геометрическая форма, аэродинамическая сила, трехмерное моделирование, число Рейнольдса.

Information about authors

Dyusembaeva, Ainura — PhD, Associate professor, Department of Engineering Thermophysics, Karaganda Buketov University, Karaganda, Kazakhstan; e-mail: aikabesoba88@mail.ru. ORCID ID: https://orcid.org/0000-0001-6627-7262;

Tanasheva, Nazgul — PhD, Associate professor, Department of Engineering Thermophysics, Karaganda Buketov University, Karaganda, Kazakhstan; e-mail: nazgulya_tans@mail.ru, ORCID ID: https://orcid.org/0000-0003-4273-0960;

Tleubergenova, **Akmaral** —3 rd year doctoral student, Department of Engineering Thermophysics, Karaganda Buketov University, Karaganda, Kazakhstan; e-mail: akmaral.tzh7@mail.ru, ORCID ID: https://orcid.org/0000-0003-0316-4222;

Bakhtybekova, **Assem** (corresponding author) — PhD, Department of Engineering Thermophysics, Karaganda Buketov University, Karaganda, Kazakhstan; e-mail: asem.alibekova@inbox.ru, ORCID ID: https://orcid.org/0000-0002-2018-8966;

Kutumova, Zhibek — Master of natural sciences, Senior lecturer, Department of physics and nanotechnology, Karaganda Buketov University, Karaganda, Kazakhstan; e-mail: zhibek_kutumova@mail.ru;

Tussuphanova, **Aigerim** — Master of natural sciences, Lecturer, Department of Engineering Thermophysics, Karaganda Buketov University, Karaganda, Kazakhstan; e-mail: aigera_aigerim@mail.ru;

Abdirova, **Nurgul** — Master of pedagogical sciences, Lecturer, Department of Engineering Thermophysics, Karaganda Buketov University, Karaganda, Kazakhstan; e-mail: abdirova_nurgul@mail.ru.

Article

Received: 26.01.2024
Accepted: 17.04.2024

UDC 539.12-17

https://doi.org/10.31489/2024PH2/65-71

N. Beissen[1,2*], M. Abishev[1,2], S. Toktarbay[1,2,3],
T. Yernazarov[2], M. Khassanov[1,2], D. Utepova[4], M. Alimkulova[2], A. Abduali[2]

[1]*Institute of Experimental and Theoretical Physics, Al-Farabi Kazakh National University, Almaty, Kazakhstan;*
[2]*Department of Theoretical and Nuclear Physics, Al-Farabi Kazakh National University, Almaty Kazakhstan;*
[3]*Department of Physics, Kazakh National Women's Teacher Training University, Almaty, Kazakhstan;*
[4]*Abai Kazakh National Pedagogical University, Almaty, Kazakhstan*
[*]*(Corresponding author's e-mail: nurzada.beissen@kaznu.edu.kz)*

An overview of light ray deflection calculation by magnetars in nonlinear electrodynamics

Due to the lack of experimental confirmation of the effects of nonlinear electrodynamics (NED) of vacuum on the electromagnetic wave, it remains the most pressing issue. One of the most optimal media for studying these effects, occurring in astrophysics, are magnetars. Various methods of studying the bending of a wave passing through the magnetospheres of magnetars play a key role in a deeper understanding of vacuum NED. This article reviews modern methods for determining the angle of bending of the electromagnetic wave under the effect of NED of vacuum and gravity, with special attention paid to NED of vacuum in intense electromagnetic fields, which is a characteristic feature of magnetars. The article discusses various methods and techniques used to measure these angles, as well as their potential astrophysical applications.

Keywords: nonlinear electrodynamics of vacuum, magnetic dipole field, magnetars, gravitational and magnetic lensing.

Introduction

NLED are divided into two different fields: nonlinear optics, which deals with nonlinear electrodynamic phenomena on the surface of materials, and vacuum nonlinear electrodynamics, which examines similar phenomena in vacuums influenced by strong electromagnetic fields. Presently, nonlinear optics and its resultant effects are extensively employed in a multitude of theoretical and empirical investigations across diverse branches of physics. Instruments that leverage these effects have been integrated into practical applications. On the contrary, the nonlinear electrodynamics of the vacuum have been comparatively less explored and understood. Maxwell's electrodynamics within a vacuum, as is widely acknowledged, functions as a linear theory. The predictions of this theory, which span a wide array of topics, are continually validated with increasing precision. Indeed, the exploration of Maxwellian electrodynamics laid the groundwork for the formulation of the special theory of relativity, which revolutionized existing notions of space and time that prevailed in Newtonian mechanics. Yet, a series of foundational physical considerations indicate that Maxwell's electrodynamics merely constitutes an initial approximation of a more expansive, nonlinear electrodynamics of the vacuum. This approximation is true in scenarios of weak electromagnetic fields, specifically when the intensities of electromagnetic fields $\vec{B}$ and $\vec{E}$ are considerably lower than the characteristic quantum electrodynamical threshold $B_q = m_0^2 c^3/e\hbar = 4.41 \cdot 10^{13}$G. Here, m_0 denotes the mass of the electron, e its charge magnitude, and $\hbar$ represents Planck's constant. Werner Heisenberg and Hans Heinrich Euler pioneered the concept of NLED in a vacuum, an advance based on the fundamental electromagnetic principles originally established by Gustav Mie. As high-power laser technology has advanced, numerous experiments have been designed to investigate these effects and have shown that the electrodynamics of the vacuum is definitely a nonlinear theory [1]. Despite such numerous ground laboratory experiments aimed at observing non-linearity in the presence of a strong magnetic field, conclusive evidence remains elusive.

An alternative method to explore is to study the effects on a cosmic scale, where celestial occurrences could shed more light on this phenomenon. Consequently, it is not surprising that the past decade has seen a wealth of proposals for NLED. Models such as rational, arcsin, arctangent, Mod-Max, and others [2], have unique features and implications that are worth further investigation. The main properties of non-linear vacuum electrodynamics and its recently proposed theories, as well as studies of light coupling, which is one of its phenomena, are reviewed [3]. Observationally, currently identified galactic pulsars and the characteristics of their magnetic fields are also obtained [4]. Identification of magnetars, possessing magnetic fields be-

tween 10^{10} and 10^{11} Tesla, was a result of the 1979 discovery of a massive flare from SGR 0526-66. This finding was instrumental in introducing the term "magnetar", credited to Duncan and Thompson, and is further elaborated in various studies [5]. There are also studies of the formation of virtual particles in the magnetosphere of growth symmetric pulsars using the global kinetic model [6]. The study of nonlinear electrodynamics in vacuum, particularly within the strong magnetic fields of magnetars, is often conducted in conjunction with an examination of gravitational effects due to their similar scales [7]. In compact astronomical bodies such as magnetars and black holes, non-linear electrodynamics provides fresh perspectives on astrophysical events. These studies delve into the interplay between electromagnetic and gravitational forces, contributing to black hole theories similar to the Reissner-Nordstrom model and addressing singularities in electric fields at their cores [1].

Research in the field of nonlinear electrodynamics of vacuum encompasses various aspects, including photon self-interaction and quantum electrodynamics considering loop corrections, leading to nonlinear electrodynamics. Special attention is paid to the phenomenon of vacuum birefringence in an external magnetic field, which finds experimental confirmation in various models of NLED. Research on vacuum birefringence sheds light on the relationship between the refractive indices and the phase velocity of electromagnetic waves, which influences our interpretation of black hole imagery, shadows, and rotational dynamics [8], thus enhancing our comprehension of these extreme cosmic conditions. An important aspect is also the study of pair-creation effects and polarization of the vacuum of particles of arbitrary spin with electric dipole and magnetic moments in a constant electromagnetic field, leading to nonlinear corrections in the Maxwell Lagrangian [9]. The work dedicated to Born-Infeld-type electrodynamics presents a new NLED model, which also considers the phenomenon of vacuum birefringence in an external magnetic field. Another study discusses various aspects of nonlinear electrodynamics, including its influence on phenomena in vacuum, underscoring the importance and diversity of emerging effects [2]. The spectral and polarization properties of magnetar radiation are also examined, considering models of condensed surface and magnetized atmosphere. The primary focus is on the influence of vacuum birefringence on polarization characteristics observable at infinity. There is considerable interest in exploring how nonlinear electrodynamics in vacuum behaves around strong-field astrophysical objects like pulsars and magnetars [10]. One of the significant discoveries in the study of nonlinear electrodynamics of the vacuum, particularly in the context of strong magnetic fields characteristic of neutron stars and magnetic white dwarfs, is the confirmation of vacuum birefringence. Investigation of the neutron star RX J1856.5-3754 using the Very Large Telescope (VLT) provided convincing evidence of this phenomenon, which is an important testament to quantum electrodynamics (QED) in strong fields and improves our understanding of the processes that occur under extreme astrophysical conditions. In addition to birefringence, considerable attention is paid to the effects of vacuum polarization. In strong magnetic fields, the vacuum behaves like an anisotropic medium, influencing the propagation of electromagnetic radiation and altering its spectrum. Particularly interesting is the change in the shape of cyclotron lines and the emergence of "vacuum lines" in X-ray spectra [10]. These studies broaden our understanding of physical processes in strong magnetic fields and provide important experimental data for the development of theoretical models in the field of QED.

Moving on to another significant aspect of nonlinear electrodynamics in vacuum, it is important to consider the phenomenon of electromagnetic beam deflection in the magnetosphere of magnetars. This effect, associated with the influence of the strong magnetic fields of magnetars on the propagation of electromagnetic waves, represents a crucial manifestation of the non-linear electrodynamical properties of the vacuum and is key to understanding electromagnetic phenomena under extreme astrophysical conditions. In-depth studies and observations on the birefringence and polarization of light in compact celestial bodies [10] focus on examining the deflection angles and the time delays of polarized light during gravitational lensing [10]. This research includes both detailed analytical and comprehensive numerical calculations of the deflection angles in the weak electric and magnetic field regimes, mainly focusing on the equatorial plane of the magnetosphere by using both the geometrical optics and one-loop effective action methods. Utilizing the principles of geometrical optics, the research has determined the deflection angles of rays passing through magnetic and electric fields and compared these findings with similar measurements in gravitational fields [11]. Furthermore, by applying the effective geodesic equation for individual photons, the study has analytically determined the impact parameter values for different ratios of this parameter to the radius of a magnetar, comparing them in the context of both gravitational and magnetic fields [12]. Also, there is the work [13-14] of studying the effective potential and deflection angles on the equatorial plane by using the polynomial Maxwell Lagrangian of some models. Additionally, analytical calculations of deflection angles of light have been

carried out using the optical medium methods used in the Gauss-Bonnet theorem [10]. In these studies, the deflection of a beam passing through the strong magnetic fields of compact objects is calculated within the framework of the generalized Born-Infeld theory in the equatorial plane. Nevertheless, there are works where the deflection angles of the electromagnetic wave fronts coming to the magnetar are numerically calculated for different impact parameter values using the Newman–Penrose (NP) formalism [15] for the Euler-Heisenberg theory, without birefringence. These studies have defined the spatial distribution of the deflection of deflection angles for various values of the dipole magnetic field of magnetars.

However, analytical and numerical calculations of the angle of light deflection in cases where regions outside the equatorial plane of compact objects in a vacuum under the influence of strong electromagnetic and gravitational fields and light birefringence are considered remain a difficult task. However, the study of these problems plays a significant role in predicting and understanding the effects NLEDof vacuum. Thus, in this article we are going to review the latest methods for obtaining the deflection angles of an electromagnetic beam passing through compact objects, taking into account the NLED of vacuum and gravity.

Methods

Numerous techniques are available to determine both the approximate and precise angles of light deflection. These include methods like the null geodesics approach, which employs either perturbation techniques or directly integrates the null geodesic equations. In a study by Jusufi et al. [16], a different computational approach was presented.

This method incorporates the notion of refractive index in optical materials alongside the Gauss-Bonnet theorem applied to isotropic optical metrics. This combination yields a precise determination of the deflection angle in both Kerr and Teo wormhole geometries. This approach has proven effective across various studies, even in scenarios involving diverse spacetime characteristics. When a gradient in refractive index is present, geometric optics techniques can be utilized to ascertain the extent of deflection angle. This approach allows for highly accurate descriptions of how the light's direction changes in various spacetimes [13, 17]. As a result, we can effectively assign a refractive index to the surrounding field.

Effective geodesic motion

As described in contemporary theoretical astrophysics, magnetars possess a magnetic dipole field, characterized by properties related to quantum electrodynamics induction $B_q = 4.41 \cdot 10^{13}$ G. In strong magnetic fields, vacuum non-linear electrodynamics becomes significant, influenced by various physical phenomena [10], described by the corresponding Lagrangians. By using polynomial Maxwell Lagrangians of the arbitrary model, it can be shown that the photon follows the null geodesic of its effective geometry:

$$g_{eff}^{\mu\nu} = \mathcal{L}_{\mathcal{F}} g^{\mu\nu} - 4\mathcal{L}_{\mathcal{F}\mathcal{F}} F_{\alpha}^{\mu} g F^{\alpha\nu}. \tag{1}$$

For weak electromagnetic wave fronts in strong external fields F_{ik}, the eikonal equation is used, as previously defined in literature [18]. It is demonstrated that these waves in nonlinear electrodynamics follow the geodesics of an effective pseudo-Riemannian space-time, influenced by the metric tensor g_{nk} and external electromagnetic field. The effective spacetime metric tensor G_{nk} is dependent on g_{nk} and the electromagnetic field tensor $F_{ni}g^{im}F_{mk}$. With different η_1 and η_2, non-linear electrodynamics induces two types of polarization. Effective metric tensors for each normal wave polarization are defined as [19]:

$$G_{nk}^{(1)} = g_{nk} - 4\eta_1 \xi F_{ni} g^{im} F_{mk}, \tag{2}$$

$$G_{nk}^{(2)} = g_{nk} - 4\eta_2 \xi F_{ni} g^{im} F_{mk}. \tag{3}$$

According to the Lagrange-Charpy theorem, to determine the paths of weak electromagnetic wave momentum in external fields and their motion, the isotropic geodesic equations in the effective spacetime with metric tensor $G_{nk}^{(1,2)}$ must be solved:

$$\begin{aligned} \frac{dK^i}{d\Sigma} + \Gamma_{mn}^{i} K^m K^p &= 0, \\ G_{nm}^{(1,2)} K^n K^m &= 0. \end{aligned} \tag{4}$$

Here, Γ^{i}_{mn} are the connection coefficients of space-time with effective metrics $G^{(1)}_{nk}$ or $G^{(2)}_{nk}$, depending on the polarization modes, Σ is an affine parameter and $K^i = dx^i/d\Sigma$ is a four-vector tangent.

Initially, the components of the effective pseudo-Riemannian space-time metric tensors $G^{(1,2)}_{nk}$ for the problem are determined as follows:

$$G^{(1,2)}_{00} = 1,$$
$$G^{(1,2)}_{\alpha\beta} = -\delta_{\alpha\beta}\left[1 - 4\eta_{\alpha\beta}\xi B^2(r)\right] + 4\eta_{1,2}\xi B_\alpha(r)B_\beta(r). \quad (5)$$

The magnetic dipole field vector B in these equations is approximated by Maxwellian precision Figure. These effective geodesic equations are solvable by selecting the coordinate z as an independent variable instead of the affine parameter. Under this approach, the geodesic equations can be expressed as follows:

$$\begin{aligned} \frac{d^2ct}{dz^2} &= -\{\Gamma^0_{mp} - \frac{dct}{dz}\Gamma^3_{mp}\}\frac{dx^p}{dz}\frac{dx^m}{dz}, \\ \frac{d^2x}{dz^2} &= -\{\Gamma^1_{mp} - \frac{dx}{dz}\Gamma^3_{mp}\}\frac{dx^p}{dz}\frac{dx^m}{dz}, \\ \frac{d^2y}{dz^2} &= -\{\Gamma^2_{mp} - \frac{dy}{dz}\Gamma^3_{mp}\}\frac{dx^p}{dz}\frac{dx^m}{dz}. \end{aligned} \quad (6)$$

The system's first integral is represented as [16]:

$$G^{(1,2)}_{np}\frac{dx^n}{dz}\frac{dx^p}{dz} = 0. \quad (7)$$

Geodesic equation (6) is independently solved, and the deflection angles of the light front are determined using an expression that is defined as the ratio of velocities:

$$\phi = \frac{180\cdot\arcsin\left(\sqrt{\frac{v_x^2+v_y^2}{c}}\right)}{\pi} = \frac{180\cdot\arcsin\left(\sqrt{\frac{\left(\frac{dx}{dz}\frac{dz}{dt}\right)^2+\left(\frac{dy}{dz}\frac{dz}{dt}\right)^2}{c}}\right.}{\pi}, \quad (8)$$

where c is the speed of light. By applying this equation, the distribution of the deflection angles of the electromagnetic ray front was obtained throughout the region by solving effective geodesic equations numerically [19], as well as specifically for the equatorial plane, was obtained. Additionally, the results were compared with previous works [17].

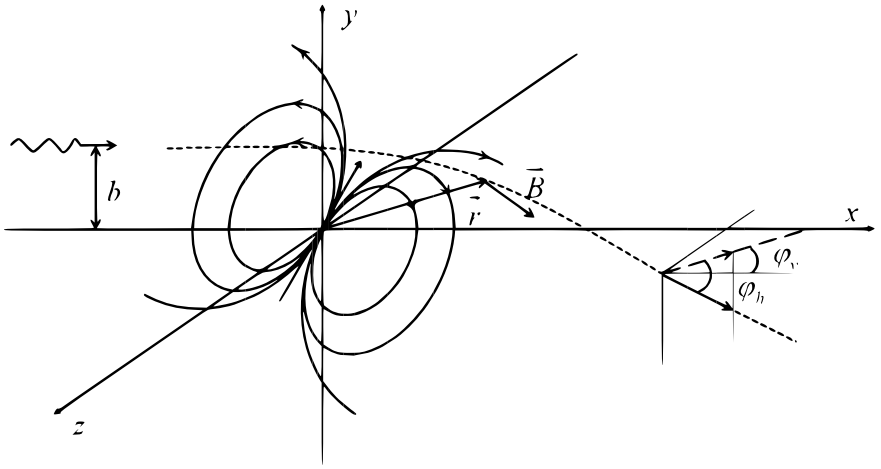

Figure. Diagram depicting the deflection of light by a magnetic dipole

The magnetic dipole is situated at the coordinate center. The photon's path is shown as a dotted line, while the projection of the outgoing photon's trajectory onto the xz-plane is illustrated with a dashed line. The angles of deflection in the horizontal (ϕ_h) and vertical (ϕ_v) directions are also indicated [22, 24-25].

Optical medium approach

Another method to compute the deflection angle of light is the optical medium. The process of deriving the equation for the light deflection angle in an arbitrary space-time through the refractive index encompasses multiple stages. This refractive index, denoted as (n(r)), can be interconnected with the corresponding

arbitrary metric parameters, notably, for example, the black hole mass (M) and its angular momentum parameter (a) as for Kerr spacetime. Using this refractive index, the Gaussian optical curvature *K* is then determined [20]:

$$\mathcal{K} = -\frac{1}{f(r^{\star})}\frac{\mathrm{d}^2 f(r^{\star})}{\mathrm{d}r^{\star 2}} = -\frac{1}{f(r^{\star})}\left[\frac{\mathrm{d}\rho}{\mathrm{d}r^{\star}}\frac{\mathrm{d}}{\mathrm{d}\rho}\left(\frac{\mathrm{d}\rho}{\mathrm{d}r^{\star}}\right)\frac{\mathrm{d}f}{\mathrm{d}\rho} + \left(\frac{\mathrm{d}\rho}{\mathrm{d}r^{\star}}\right)^2\frac{\mathrm{d}^2 f}{\mathrm{d}\rho^2}\right]. \quad (9)$$

Moreover, the concluding equation can be articulated using the refractive index it yields:

$$\mathcal{K} = -\frac{n(\rho)n''(\rho)\rho - \left(n'(\rho)\right)^2\rho + n(\rho)n'(\rho)}{n^4(\rho)\rho}. \quad (10)$$

One can derive for the Kerr spacetime metric the following Gaussian optical curvature as [3]:

$$\mathcal{K} \simeq -\frac{2M}{r^2} + \frac{18aMb}{r^5} + \mathcal{O}(M^2, a^2). \quad (11)$$

In addition, for the Born-Infeld Generelized NLED mode, the Gaussian curvature can be derived as [14]:

$$\mathcal{K} = \frac{18\mu^2}{\beta^2 r^8}. \quad (12)$$

The deflection angle of the ray, in addition to being found using equation (10), can also be applied for calculation and comparison using the effective metric method derived from the Newman-Penrose formalism [15]. Therefore, the equation for the bending angle in generalized Born-Infeld electrodynamics is defined as [14, 21–25]:

$$\Delta\theta = -\frac{15\pi}{16}\frac{\mu^2}{\beta^2 b^6}, \quad (13)$$

here, b represents the impact parameter, and the negative sign signifies that the bending is directed towards the magnetic dipole.

Discussion and summary

This review focuses on investigating the behavior of vacuum NLED, specifically in relation to the deflection of light around compact celestial objects like magnetars. The importance of studying NLED of vacuum in an astrophysical context is emphasized, highlighting its relevance in understanding such environments. The paper presents a comparative analysis of different theoretical frameworks of nonlinear electrodynamics, including the optical medium and the Newman-Penrose formalism. This analysis demonstrates the wide range and complexity of theoretical approaches needed to comprehend light deflection in strong electromagnetic fields. At the same time, scientific works presents that both calculations are reduced to the same value of deflection angles. Although this depends on the limitation of calculations. The conclusions drawn from these models enhance our understanding of electromagnetic phenomena in extreme settings and make significant contributions to the field of quantum electrodynamics. Understanding these interactions is crucial for understanding the behavior and characteristics of such entities. Additionally, the article highlights the importance of observational astrophysics in validating theoretical predictions and establishing a foundation for future astronomical observations and experiments. By connecting theoretical principles with their potential real-world applications, this review bridges theoretical physics with observational astronomy. It represents a significant advancement in unraveling complex phenomena in the universe and stimulates further research and discovery. The exploration of nonlinear electrodynamics in a vacuum and its implications for our understanding of the universe offers a fresh perspective in the field of astrophysics. As a result, this review contributes substantially to astrophysics by presenting innovative approaches to studying nonlinear electrodynamics in a vacuum and its implications for the cosmos. The authors advocate for further research and validation of the complex dynamics of astrophysical environments, particularly around magnetars, using both theoretical and empirical methods. This review serves as evidence of the ongoing evolution of our understanding of the cosmos, driven by the interplay between theory and empirical data.

Acknowledgments

This research was funded by the Ministry of Science and Higher Education of the Republic of Kazakhstan (Grant No. AP14869524). KhM acknowledges the support through the postdoctoral fellowship program of the Ministry of Science and Higher Education of the Republic of Kazakhstan (Grant No. AP14972943).

References

1 Mailliet, A.M., et al. (2024). Performance of a sagnac interferometer to observe vacuum optical nonlinearity. arXiv preprint arXiv:2401.13720

2 Kruglov, S.I. (2017). Born-Infeld-type electrodynamics and magnetic black holes. *Annals of Physics, 383,* 550–559.

3 Beissen, N., et al. (2023). The exploring nonlinear vacuum electrodynamics beyond maxwell's equations. *International Journal of Mathematics and Physics, 14*(1), 61–70.

4 Beloborodov, A.M. (2022). Scattering of ultrastrong electromagnetic waves by magnetized particles. *Physical Review Letters, 128*(25), 255003.

5 Kaspi, V.M., et al. (2003). Major Soft Gamma Repeater-like Outburst and Rotation Glitch in the No-longer-so- anomalous X-Ray Pulsar 1E 2259+586. *The Astrophysical Journal, 588*(2), L93–L96.

6 Rui, Hu & Beloborodov, A.M. (2022). Axisymmetric pulsar magnetosphere revisited. *The Astrophysical Journal, 939*(1), P. 42.

7 Vasili'ev, M.I., et al. (2017). The Effects of Vacuum Nonlinear Electrodynamics in an Electric Dipole Field. *Moscow University Physics Bulletin, 72*(6), 513–517.

8 Muratkhan, A., et al. (2023). Ashadows from the static black hole mimickers. *International Journal of Mathematics and Physics, 13*(2), 44–49.

9 Kruglov, S.I. (2001). Pair production and vacuum polarization of arbitrary spin particles with EDM and AMM. *Annals of Physics, 293*(2), 228–239.

10 Gnedin, Yu.N. (1990). Effect of vacuum polarization in a strong magnetic field and spectral features of x-ray source emission. *In International Astronomical Union Colloquium, 115,* 78–84.

11 Abishev, M., et al. (2016). Some astrophysical effects of nonlinear vacuum electro- dynamics in the magnetosphere of a pulsar. *Astroparticle Physics, 73,* 8–13.

12 Abishev, M.E., et al. (2018). Effects of non-linear electrodynamics of vacuum in the magnetic quadrupole field of a pulsar. *Monthly Notices of the Royal Astronomical Society, 481*(1), 36–43.

13 Beissen, N., et al. (2023). Gravitational Refraction of Compact Objects with Quadrupoles. *Symmetry, 15*(3), P. 614.

14 Beissen, N., et al. (2024). Bending of light by magnetars within generalized born–infeld electrodynamics: Insights from the gauss–bonnet theorem. *Symmetry, 16*(1), P. 132.

15 Newman, E., & Penrose, R. (1962). An approach to gravitational radiation by a method of spin coefficients. *Journal of Mathematical Physics, 3,* 566–578.

16 Beissen, N., et al. (2023). Nonlinear electrodynamical lensing of electromagnetic waves on the dipole magnetic field of the magnetar. *International Journal of Modern Physics D, 32*(6), 2350106.

17 Jusufi, K. (2018). Gravitational deflection of relativistic massive particles by Kerr black holes and Teo wormholes viewed as a topological effect. *Physical Review D, 98*(6), 064017.

18 Toktarbay, S., et al. (2022). Gravitational field of slightly deformed naked singularities. *European Physical Journal C, 82*(4), P. 382.

19 Denisov, V.I., Denisova, I.P., & Svertilov, S.I. (2001). Nonlinear Electrodynamic Effect of Ray Bending in the Magnetic-Dipole Field. *Physics — Doklady, 46*(10), 705–707.

20 Okyay, M. & Ovgun, A. (2022). Nonlinear electrodynamics effects on the black hole shadow, deflection angle, quasinormal modes and greybody factors. *Journal of Cosmology and Astroparticle Physics, 2022*(01), P. 009.

21 Jin, Young Kim. (2021). Deflection of light by a Coulomb charge in Born-Infeld electrodynamics. *European Physical Journal C, 81*(6), P. 508.

22 Jin, Young Kim. (2012). Bending of electromagnetic wave in an ultra-strong magnetic field. *Journal of Cosmology and Astroparticle Physics, 10,* P. 056.

23 Jin, Young Kim. (2022). Deflection of light by magnetars in the generalized Born-Infeld electrody- namics. *European Physical Journal C, 82*(5), P. 485.

24 Denisov, V.I., Denisova, I.P., & Sokolov, V.A. (2017). Nonperturbative QED vacuum birefringence. *Journal of High Energy Physics,* (5), P. 105.

25 Denisov, V.I., et al. (2016). Pulsar radiation in post — Maxwellian vacuum nonlinear electrodynamics. *Physical Review D, 94*(4), 045021.

Н. Бейсен, М. Әбішев, С. Тоқтарбай,
Т. Ерназаров, М. Хасанов, Д. Утепова, М. Алимкулова, А. Абдуали

Сызықтыемес электрдинамикалық магнетарлардағы жарық сәулелерінің бұрылу бұрыштарын есептеуге шолу

Вакуумның сызықтыемес электрдинамикасының (СЕЭД) электрмагниттік сәулеге әсерінің эксперименталды расталмауына байланысты ол ең өзекті мәселе болып саналады. Астрофизикадағы осы әсерлерді зерттеудің ең оңтайлы ортасының бірі — магнетарлар. Магнетарлардың магнитсфералары арқылы өтетін сәуленің қисаюын зерттеудің әртүрлі әдістері вакуумдық СЕЭД-ны тереңірек түсінуде шешуші рөл атқарады. Мақалада магнетарларға тән қасиет болып табылатын қарқынды электрмагниттік өрістерде вакуумдық СЕЭД-ға ерекше назар аудара отырып, вакуумдық СЕЭД және ауырлық күшінің әсерінен электрмагниттік сәуленің қисық бұрышын анықтаудың заманауи әдістеріне шолу жасалған. Авторлар осы бұрыштарды өлшеу үшін қолданылатын әртүрлі әдістер мен тәсілдерді қарастырған және олардың потенциалды астрофизикалық қолданбаларын талқылаған.

Кілт сөздер: вакуумның сызықтыемес электрдинамикасы, магниттік диполь өрісі, магнетарлар, гравитациялық және магниттік бұрмалану.

Н. Бейсен, М. Абишев, С. Токтарбай,
Т. Ерназаров, М. Хасанов, Д. Утепова, М. Алимкулова, А. Абдуали

Обзор расчета отклонения лучей света магнетарами в нелинейной электродинамике

Из-за отсутствия экспериментального подтверждения эффектов нелинейной электродинамики (НЭД) вакуума на электромагнитный луч он является самым актуальным вопросом. Одной из самых оптимальных сред для изучения этих эффектов, происходящих в астрофизике, являются магнетары. Различные методы изучения искривления луча, проходящего через магнетосферы магнетаров, играют ключевую роль в более глубоком понимании вакуумной НЭД. Настоящая статья представляет собой обзор современных методов определения угла искривления электромагнитного луча под эффектом НЭД вакуума и гравитации, особое внимание уделяя НЭД вакуума в интенсивных электромагнитных полях, что является характерной чертой магнетаров. Авторами рассмотрены различные методы и техники, используемые для измерения этих углов, а также обсуждены их потенциальные астрофизические применения.

Ключевые слова: нелинейная электродинамика вакуума, магнитное дипольное поле, магнетары, гравитационное и магнитное линзирование.

Information about authors

Beissen, Nurzada — Candidate of physical and mathematical sciences, Associate Professor, Dean of the Faculty of Physics and Technology, Al-Farabi Kazakh National University, Institute of Experimental and Theoretical Physics, Almaty, Kazakhstan; e-mail: nurzada.beissen@kaznu.edu.kz;

Abishev, Medeu — Doctor of physical and mathematical sciences, professor, Department of Theoretical and Nuclear Physics, Al-Farabi Kazakh National University, Almaty Kazakhstan; e-mail: abishev-me@gmail.com;

Toktarbay, Saken — PhD, Department of Theoretical and Nuclear Physics, Al-Farabi Kazakh National University, Almaty Kazakhstan Department of Physics, Kazakh National Women's Teacher Training University, Almaty Kazakhstan; e-mail: Saken.Toktarbay@kaznu.edu.kz;

Yernazarov, Tursynbek — Research fellow, Department of Theoretical and Nuclear Physics, Al-Farabi Kazakh National University, Institute of Experimental and Theoretical Physics, Almaty, Kazakhstan; e-mail: ernazarovt@gmail.com;

Khassanov, Manas — PhD, Department of Theoretical and Nuclear Physics, Al-Farabi Kazakh National University, Almaty Kazakhstan; e-mail: Manas.Khassanov@kaznu.edu.kz;

Utepova, Daniya — PhD student, Abai Kazakh National Pedagogical University, Almaty, Kazakhstan;

Alimkulova, Madina — PhD student, Department of Theoretical and Nuclear Physics, Al-Farabi Kazakh National University, Almaty Kazakhstan; e-mail: m.alimkulova2911@gmail.com;

Abduali, Aidana — PhD student, Department of Theoretical and Nuclear Physics, Al-Farabi Kazakh National University, Almaty Kazakhstan; e-mail: abduali_aidana@kaznu.edu.kz.

Article

Received: 20.12.2023
Accepted: 20.02.2024

UDC 536.24

https://doi.org/10.31489/2024PH2/72-81

N.Zh. Jaichibekov*, D.Y. Kurmanova, A.S. Zhumanbayeva

L.N. Gumilyov Eurasian National University, Astana, Kazakhstan
**(Corresponding author's e-mail: jaich@mail.ru)*

Mathematical model and numerical calculation of the movement of oil products in helicoidal heat exchangers

Heating of oil and oil products is widely used to reduce energy losses during transportation. An approach is developed to determine the effective length of the heat exchanger and the temperature of the cold coolant (oil) at its outlet in the case of a strong dependence of oil viscosity on temperature. The method of the log-mean temperature difference, modified for the case of variable viscosity, and the methods of computational fluid dynamics (CFD) are used for calculations. The results of numerical calculations are compared with the data obtained on the basis of a theoretical approach at a constant viscosity. When using a theoretical approach with a constant or variable viscosity, the heat transfer coefficients to cold and hot coolants are found using criterion dependencies. The Reynolds-averaged Navier-Stokes (RANS) and a turbulence model that takes into account the laminar-turbulent transition are applied. In the case of variable oil viscosity, a transition from the laminar flow regime to the turbulent one is manifested, which has a significant effect on the effective length of the heat exchanger. The obtained results of CFD calculations are of interest for the design of heat exchangers of a new type, for example, helicoidal ones.

Keywords: heat transfer, numerical calculation, helical heat exchanger, oil, hydrodynamics, coolants, heat flow, laminar-turbulent transition, Navier-Stokes equation, flow turbulization.

Introduction

Helicoidal heat exchangers are designed with profiled pipes and fans with a screw profile, which improves the conditions for heat exchange. In works [1-2], modeling and calculation of the hydrodynamics of heat carriers (water, oil) flowing through smooth pipes are given. The obtained results of numerical calculations are used to find optimal ways to intensify the heat transfer process [3–5]. Research shows that the influence of the viscosity of the pumped oil on the hydraulic properties of the pipeline decreases when pumping in a developed turbulent regime.

Heat exchangers are used in many applications, with efficient heat exchangers being a basic requirement of the industry. Efforts to increase heat transfer, increase heat transfer rates, reduce the size of heat exchangers and improve efficiency since the beginning of global industrialization. The higher heat transfer potential of spiral coils is of interest to many researchers who study the fluid dynamics inside the spiral tubes of the heat exchanger they serve. The bending of the pipe causes the application of centrifugal force, which leads to the formation of a secondary flow due to the curvature of the pipe. The centrifugal force is controlled by the centrifugal force, which is determined by the curvature of the coil, and the twisting caused by the liquid is affected by the pitch or angle of the coil. Liquids arising from the outside of the pipe move at a higher speed than those flowing inside the pipe, which is caused by the curvature affecting the speed of movement [6]. In work [7], spiral coils in heat exchangers of various shapes and operating conditions were analyzed and compared with straight-tube heat exchangers, and their performance and

efficiency were analyzed by studying factors affecting the performance and efficiency of a spiral heat exchanger, such as the coefficient of curvature and other factors. The helical coil in heat exchangers (HCHE) provides higher heat transfer speeds and efficiency than straight pipes and other heat exchangers due to the development of secondary flow inside the spiral tube, while the heat transfer coefficient increases with increasing curvature coefficient (HCHE) at the same flow rates.

This article discusses the numerical calculation of a helicoidal heat exchanger. Exactly, the results of calculating the oil temperature and heat flow at the outlet of the pipe winding on the surface are presented. When solving this problem, the number of twists N, the heat transfer coefficient, the flow velocity and the temperature of the oil at the pipe inlet varied as input parameters.

Calculation method

The problem is solved in the Ansys Fluent software package, which uses stationary Navier-Stokes equations averaged by Reynolds (Navier–Stokes equations averaged by Reynolds).

The numerical calculation was carried out by the finite Volume method FVM (Finite Volume Method) using an uneven grid in the computational domain. Schematically, the calculated pipe with windings and the calculated grid on it is shown in Figure 1.

Figure 1. Calculation grid of the pipe with windings

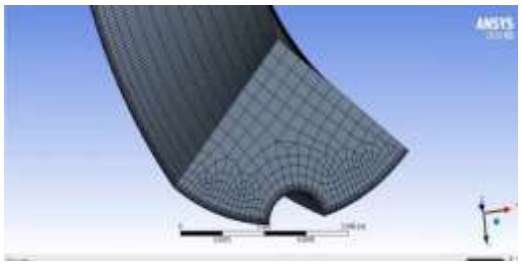

Figure 2. Calculation grid for a quarter of a pipe

To save computing resources (time and memory), the calculation was carried out on the fourth part of the pipe, since the pipe is axisymmetric. Figure 2 shows a quarter of the calculated grid, which shows the thickening of the grid at the pipe boundary, where there are the greatest gradients of flow parameters. More details about unstructured grids are described in [8].

The basic Navier-Stokes equations and the k-ω SST equations were used for the calculation [9-10].

The continuity equation:

$$\frac{\partial v_j}{\partial x_j} = 0. \tag{1}$$

The equation of momentum:

$$v_j \frac{\partial v_i}{\partial x_j} = -\frac{1}{\rho}\frac{\partial p}{\partial x_i} + \frac{\partial}{\partial x_i}\left[(\nu + \nu_t)\frac{\partial v_i}{\partial x_j}\right]. \tag{2}$$

The energy equation:

$$v_j \frac{\partial T}{\partial x_j} = \frac{\partial}{\partial x_i}\left[(\frac{\nu}{Pr} + \frac{\nu_t}{Pr_t})\frac{\partial T}{\partial x_j}\right]. \tag{3}$$

Here ρ is the density, and v_i is the component of velocity in the direction of coordinates — x_i, p — pressure, T — temperature, ν, ν_t — molecular and turbulent viscosity of liquid, Pr, Pr_t — Prandtl number for laminar and turbulent, respectively.

The k-ω turbulence model takes into account two more transport equations. The Reynolds number $Re_{\theta t}$ and the momentum of the transition beginning are two equations written for it, and the second one is obtained for the flow regime intermittency γ of the transformation process. Transmission equation for pulse thickness and Reynolds number and intermittency transport equation are as follows:

Transmission equation for pulse thickness and Reynolds number:

$$v_j \frac{\partial Re_{\theta t}}{\partial x_j} = P_{\theta t} + \frac{\partial}{\partial x_j}\left[\sigma_{\theta t}(\nu + \nu_t)\frac{\partial Re_{\theta t}}{\partial x_j}\right]. \tag{4}$$

Intermittency transport equation:

$$v_j \frac{\partial \gamma}{\partial x_j} = P_\gamma - \mathrm{E}_\gamma + \frac{\partial}{\partial x_j}\left[(\nu + \frac{\nu_t}{\sigma_\gamma})\frac{\partial \gamma}{\partial x_j}\right]. \quad (5)$$

Here $P_{\theta t}$ — time derivative of the Reynolds number with respect to the momentum loss thickness, P_γ and E_γ — time-specific formation and dissipation of intermittency conditions, $\sigma_{\theta t}$ and σ_γ are constants of the model.

Results of calculations and discussions

Since the system of initial equations is nonlinear, an iterative approach was used for their numerical solution, in which the linearized Navier-Stokes equations were solved. According to the results of calculations, the average mass temperature and heat flow of oil at the outlet of the pipe are obtained. To solve this problem, the following initial parameters were used: the radius of the pipe $R_1 = 0{,}006\,m$, the radius of the groove $R_2 = 0{,}001\,m$, the length of the pipe $L_1 = 1m$, the heat transfer coefficient $\alpha_1 = 1000\,W/(m^2 \cdot K)$, the temperature of the washing liquid (water) $\mathrm{T}_2 = 423K$, the speed oil flow $v_1 = 4\,m/s$, oil temperature at the pipe inlet $T_{in_1} = 313K$.

Boundary conditions of the third type were applied (heat transfer coefficients and the washing liquid's temperature were measured on the pipe's surface). The number of windings on the pipe surface is determined by the number of twists N, which in this problem ranged from 1 to 40 with an interval of 5.

A graph illustrating the relationship between the number of twists N and the average mass temperature of oil at the pipe's exit is presented in Figure 3. The image illustrates how the temperature of the oil at the outlet rises as the number of twists increases, intensifying the heat exchange between the heat carriers.

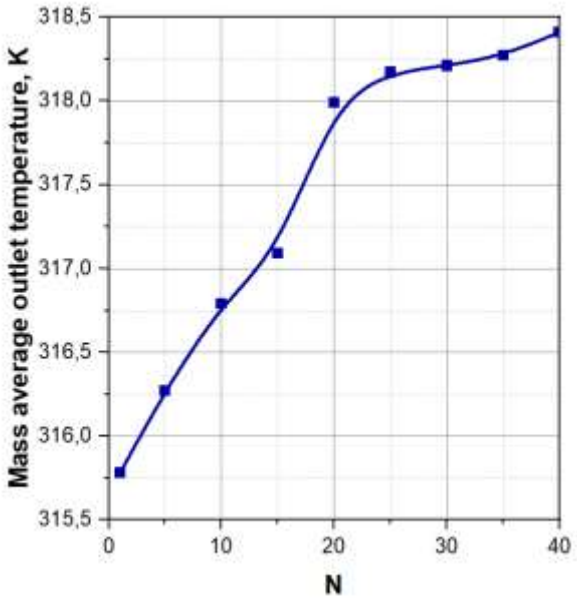

Figure 3. Dependence of the average mass temperature at the outlet of the heat exchanger on the twist N

A graph illustrating the relationship between the number of twists N and the heat flow Q through the pipe's surface from the side of the washing liquid is displayed in Figure 4. Here, the amount of heat flow also increases with an increase in the number of twists on the pipe.

The increase in the average mass temperature of oil at the outlet of the heat exchanger (Fig. 3) and the increase in the value of the heat flow (Fig. 4) with an increase in the number of twists of the N tube is explained by turbulence of the flow due to its twisting. When the flow is turbulated, the process of diffusion of liquid particles intensifies and the heat exchange between particles intensifies. This process will occur the more intensively, the more the number of twists of the tube.

Further, heat transfer coefficients α were set in the range from 1000 $\mathrm{W}/(m^2 \cdot K)$ to 6000 $W/(m^2 \cdot K)$ with a constant number of twists equal to 10.

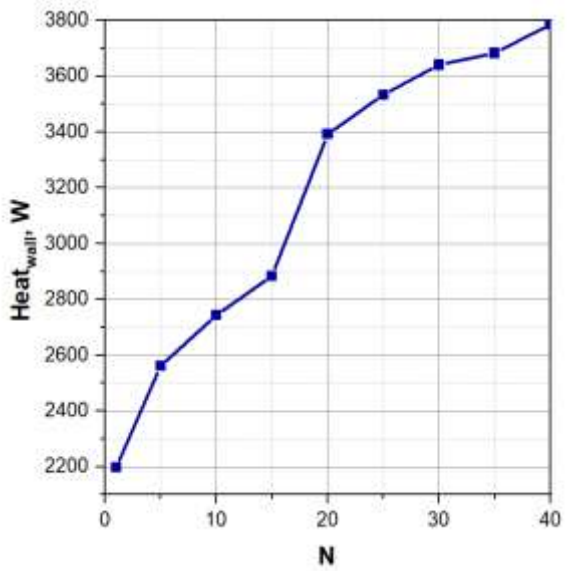

Figure 4. The dependence of the heat flow Q on the twist N

Consequently, Figure 5 displays a graph that illustrates how the heat transfer coefficient α and the average mass temperature of oil at the heat exchanger's outlet rely on each other. The graphic illustrates how the average mass temperature at the outlet climbs dramatically as the heat transfer coefficient rises. This is explained by the natural process of increasing the temperature of the liquid (oil) with increasing heat transfer from the external washing liquid (water) to the surface of the inner tube, and from it to the inner liquid, which increases its average mass temperature.

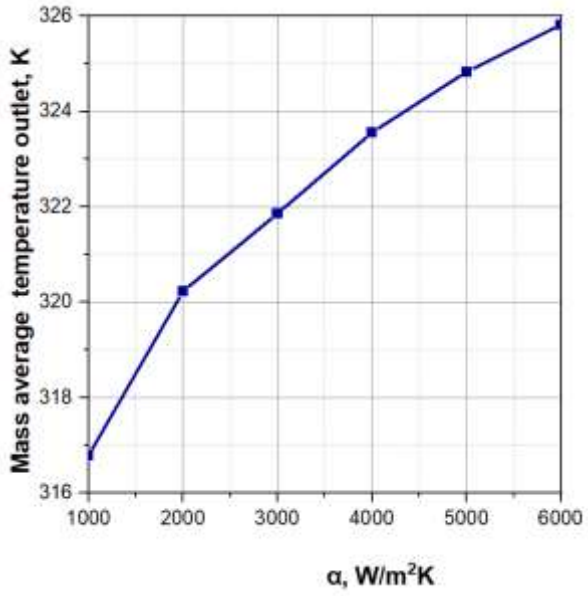

Figure 5. Dependence of the average mass temperature at the outlet of the heat exchanger on the heat transfer coefficient α

The influence of the heat flow through the pipe surface on the heat transfer α is shown in Figure 6. A rise in the heat transfer coefficient causes the heat flow to increase three times from its starting value. The intensification of heat transfer between heat carriers is well described by this process. This happens in a similar way to the previous case, i.e. with an increase in heat transfer from the external washing fluid (water) to the surface of the inner tube, the heat flow towards the oil increases.

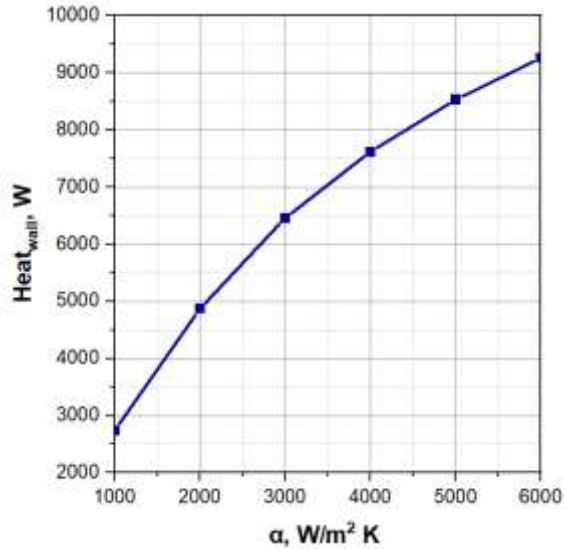

Figure 6. The dependence of the heat flow on the heat transfer coefficient

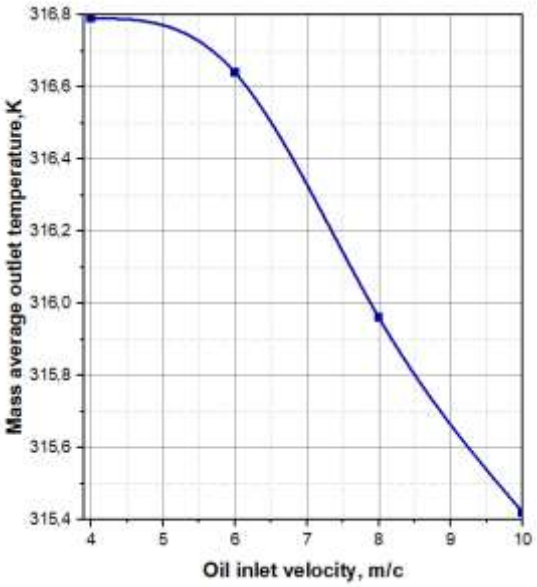

Figure 7. Dependence of the average mass temperature at the outlet of the heat exchanger on the oil flow rate at the inlet

Figures 7 and 8 show graphs of the dependences of the average mass temperature and heat flow through the surface on the oil flow velocity v at the inlet. With an increase in the oil flow rate at the inlet to the pipe, the diffusion process decreases, and, as a result, the main flow rate will increase compared to the fluctuation component at a given number of turns N. This in turn leads to a decrease (slightly) in the flow velocity along the tube, including at the outlet of the tube (Fig. 7). Based on the above, the heat flow will, on the contrary, increase depending on the increase in the flow rate of oil at the inlet (Fig. 8). Both figures show that at approximately a speed of $v = 6\,m/s$, there is a sharp change in the graph. This is due to the fact that at a velocity of $v = 6\,m/s$, the Reynolds number *Re* reaches 2880, where a laminar-turbulent transition mode occurs.

The oil temperature at the heat exchanger's outlet increases when the temperature at the pipe's input is changed from 313 K to 363 K. Figure 9 displays the dependence diagram for this change. The graph indicates that this dependence is linear. This is physically explained very simply — with a higher oil temperature at the inlet, we get a higher oil temperature at the outlet.

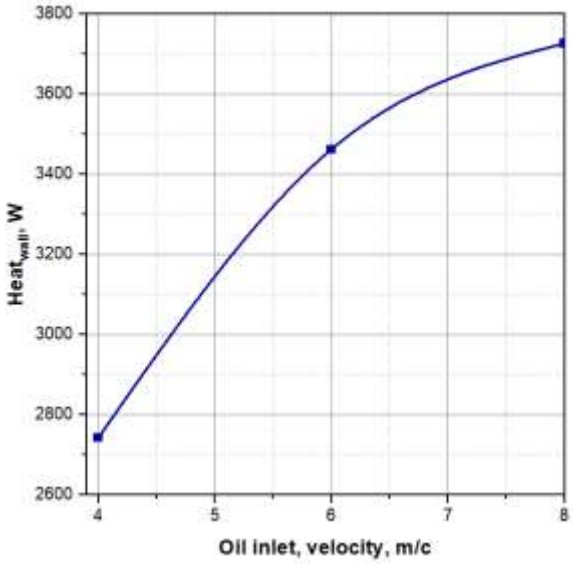

Figure 8. Dependence of the heat flow on the oil flow velocity at the inlet

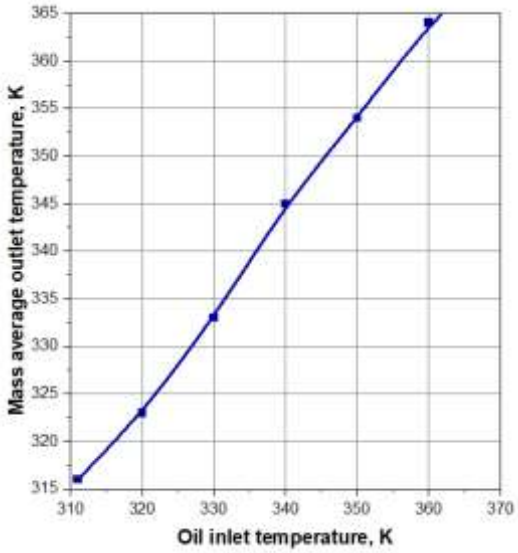

Figure 9. Dependence of the average mass temperature at the outlet of the heat exchanger on the temperature at the inlet

Figure 10 illustrates the opposite situation by demonstrating how the inlet temperature affects the heat flow on the pipe surface. It is evident that when the oil inlet temperature rises, the heat flows the difference between the oil's temperature and the washing liquid's temperature decreases. Since the heat flow is determined by the temperature difference of the media, with an increase in the temperature of the oil at the inlet, the temperature difference between the two liquids decreases (at a constant water temperature), which leads to a decrease in the heat flow on the surface of the tube.

Figure 11 shows comparative graphs of the dependence of the mass-average temperature of oil at the outlet for a tube with a smooth [11] and helicoidal surface with a number of twists N from 10 to 40 with a step of 10. It can be seen from the figure that the temperature of oil in a tube with coils is higher along its entire length compared to a tube with a smooth surface, while reaching a maximum temperature difference of up to 9.5%, which is explained by turbulence of the flow, as well as with an increase in heat flow through the surface due to a slight increase in the surface of the tube due to recesses.

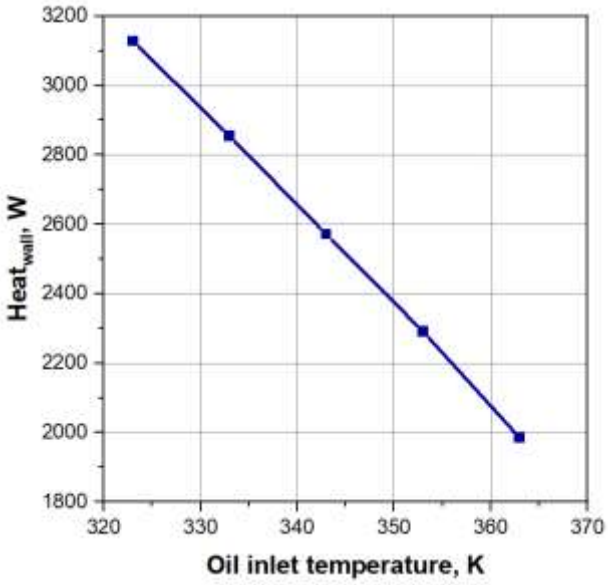

Figure 10. Dependence of the heat flow on the pipe surface on the inlet temperature

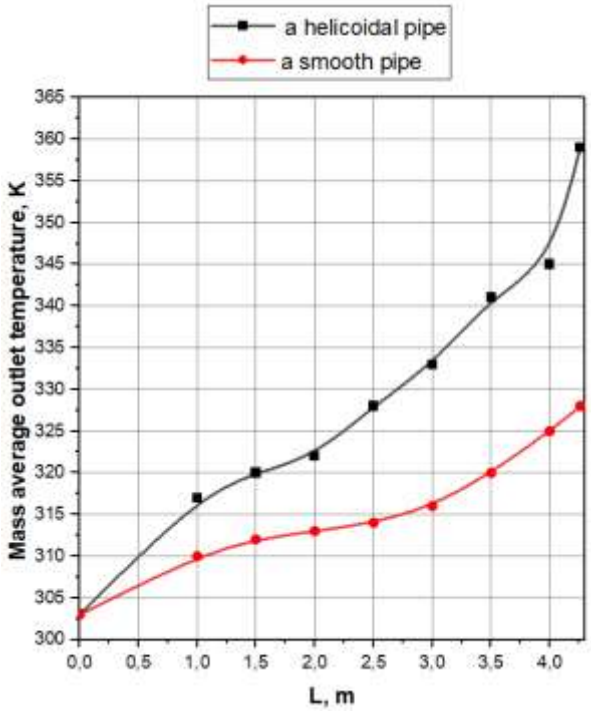

Figure 11. Comparison of the dependence of the average mass temperature of oil at the outlet for a tube with a smooth and helicoid surface with a number of twists N =10-40.

Conclusion

After using a coiled tube as an example, we can thus deduce from the foregoing facts that heat exchangers with helicoid geometries have superior heat transfer capabilities than heat exchangers with smooth tubes. This is because the turbulence caused by twisted windings in the oil flow increases the heat exchange between liquid layers as a result of the diffusion process. Moreover, the oil temperature may rise as a result of a tiny rise in the tube's surface brought on by recesses, which enhances heat transfer through the surface. It can also be noted here that with variable viscosity of oil, the transition from laminar to turbulent mode is manifested, while this effect is not taken into account when calculating for constant viscosity.

References

1 Курманова Д.Е. Численный расчет гидродинамики теплоносителей с учетом зависимости вязкости от температуры / Д.Е. Курманова, Н.Ж. Джайчибеков, К.Н. Волков, А.Г. Карпенко // Вестн. Евраз. нац. ун-та им. Л.Н. Гумилева. Математика. Компьютерные науки. Механика. — 2022. — Т. 141. — №4. — С. 28–41. https://doi.org/10.32523/2616-7182/bulmathenu.2022/4.2.

2 Курманова Д.Е. Распределение температуры теплоносителей вдоль теплообменного аппарата / Д.Е. Курманова // сб. материалов XVII Междунар. науч. конф. студентов и молодых ученых «Gylym jáne bilim — 2022». — 2022. — С. 1603–1607. https://smart.enu.kz/api/serve?path=/general/files/6c96824d-24df-4d98-83a3-67dddf36551e.pdf

3 Osley W.G. et al. CFD investigation of heat transfer and flow patterns in tube side laminar flow and the potential for enhancement / W.G. Osley, P. Droegemueller, P. Ellerby // Chemical Engineering Transactions. — 2013. — Vol. 35. — P. 997–1002. DOI: 10.3303/CET1335166.

4 Karar O. Experimental and numerical investigation on convective heat transfer in actively heated bundle-pipe / O. Karar, S. Emani, S.M. Gounder, M.M. Myo Thant, H. Mukhtar, M. Sharifpur, M. Sadeghzadeh // Engineering Applications of Computational Fluid Mechanics. — 2021. — Vol. 15. — No. 1. — P. 848–864. https://doi.org/10.1080/19942060.2021.1920466.

5 Rana S. et al. CFD approach for the enhancement of thermal energy storage in phase change material charged heat exchanger / S. Rana, M. Zunaid, R. Kumar // Case Studies in Thermal Engineering. — 2022. — Vol. 33. — P. 101921. https://doi.org/10.1016/j.csite.2022.101921.

6 Borse D. A Review on Helical Coil Heat Exchanger / D. Borse, J.V. Bute // International Journal for Research in Applied Science & Engineering Technology. — 2018. — 6. — P. 492–497. https://doi.org/10.22214/ijraset.2018.2070

7 Inyang U. Heat Transfer in Helical Coil Heat Exchanger / U. Inyang, I. Uwa // Advances in Chemical Engineering and Science. — 2022. — 12. — P. 26–39. doi: 10.4236/aces.2022.121003.

8 Волков К.Н. Вычислительные технологии в задачах механики жидкости и газа: учеб. пос. / К.Н. Волков, В.Н. Емельянов. — М.: ФИЗМАТЛИТ, 2012. — 468 с.

9 Coder J.G. Computational fluid dynamics compatible transition modeling using an amplification factor transport equation / J.G. Coder, M.D. Maughmer // AIAA Journal. — 2014. — Vol. 52. — No. 11. — P. 2506–2512. https://doi.org/10.2514/1.J052905.

10 Kurmanova, D. et al. Modelling and Simulation of Heat Exchanger with Strong Dependence of Oil Viscosity on Temperature / D. Kurmanova, N. Jaichibekov, A. Karpenko, & K. Volkov // Fluids. — 2023. — 8. — 95. — P. 1–18. https://doi.org/10.3390/fluids8030095.

11 Kurmanova D.E. et al. Numerical modeling and calculation of heat transfer between heat carriers in heat exchangers / D.E. Kurmanova, N.J. Jaichibekov, A.G. Karpenko, K.N. Volkov // Bulletin of the Karaganda university. Physics series. — 2023. — No. 1 (109). — P. 59–70. DOI:10.31489/2023PH1/59-70.

Н.Ж. Жәйшібеков, Д.Е. Құрманова, А.С. Жұманбаева

Геликоидты жылу алмастырғыштардағы мұнай өнімдері қозғалысының математикалық моделі және сандық есебі

Мақала геликоидты жылу алмастырғыштағы жылу алмасу процестерін сандық есептеуге арналған. Жылу беруді жақсарту үшін геликоидты жылу алмастырғыштар профильді құбырларды және бұрандалы қырлы профильді пайдаланады. Тасымалдау кезінде энергия шығынын азайту үшін мұнай мен мұнай өнімдерін қыздыру кеңінен қолданылады. Мұнай тұтқырлығының температураға қатты тәуелділігі жағдайында жылу алмастырғыштың тиімді ұзындығын және оның шығуындағы суық салқындатқыштың (мұнайдың) температурасын анықтауға арналған тәсіл әзірленді. Есептеулер үшін тұтқырлықтың өзгермелі жағдайына өзгертілген температураның орташа айырмашылығының логарифмдік әдісі және есептеу гидродинамикасы (CFD) әдістері пайдаланылған. Сандық есептеулердің нәтижелері тұрақты тұтқырлық кезінде теориялық тәсіл негізінде алынған мәліметтермен салыстырылған. Тұрақты немесе өзгермелі тұтқырлығы бар теориялық тәсілді қолданған кезде суық және ыстық салқындатқыш сұйықтықтардың жылу беру коэффициенттері критериалды тәуелділіктерді қолдану арқылы анықталады. Рейнольдс бойынша орташа Навье-Стокс әдісі (RANS) және ламинарлы-турбулентті ауысуды ескеретін турбуленттілік моделі қолданылған. Майдың өзгермелі тұтқырлығы жағдайында ламинарлы ағын режимінен турбулентті режимге ауысу көрінеді, бұл жылу алмастырғыштың тиімді ұзындығына айтарлықтай әсер етеді. Алынған CFD есептеулерінің нәтижелері жылу алмастырғыштардың жаңа түрін, мысалы, геликоидты жобалауға қызығушылық тудырады. Жұмыста ағынның параметрлеріне, сондай-ақ түтіктің бұралу санына байланысты түтіктің шығуындағы мұнайдың массалық-орташа температурасы, кіріс және шығыс температурасы, жылдамдығы, құбыр бетіндегі жылу ағынының есептеу нәтижелері берілген.

Кілт сөздер: жылу беру, сандық есептеу, геликоидты жылу алмастырғыш, май, гидродинамика, салқындатқыш сұйықтықтар, жылу ағыны, ламинарлы-турбулентті ауысу, Навье-Стокс теңдеуі, ағынның турбулизациясы.

Н.Ж. Джайчибеков, Д.Е. Курманова, А.С. Жуманбаева

Математическая модель и численный расчет движения нефтепродуктов в теплообменных аппаратах геликоидной формы

Статья посвящена численному расчету теплообменных процессов в теплообменнике геликоидной формы. В геликоидных теплообменниках использованы профилированные трубки и ребра винтового профиля, что улучшает теплообмен. Нагрев нефти и нефтепродуктов широко применяется для снижения потерь энергии при транспортировке. Разработан подход для определения эффективной длины теплообменника и температуры холодного теплоносителя (масла) на его выходе в случае сильной зависимости вязкости масла от температуры. Для расчетов используются метод логарифмической средней разности температур, модифицированный для случая переменной вязкости, и методы вычислительной гидродинамики (CFD). Результаты численных расчетов сравниваются с данными, полученными на основе теоретического подхода при постоянной вязкости. При применении теоретического подхода с постоянной или переменной вязкостью коэффициенты теплоотдачи холодным и горячим охлаждающим жидкостям определяются с использованием критериальных зависимостей. Используются усредненный по Рейнольдсу метод Навье-Стокса (RANS) и модель турбулентности, учитывающая ламинарно-турбулентный переход. В случае переменной вязкости масла проявляется переход от ламинарного режима течения к турбулентному, что оказывает существенное влияние на эффективную длину теплообменника. Полученные результаты CFD-расчетов представляют интерес для проектирования теплообменников нового типа, например геликоидальных. В работе приведены результаты расчетов среднемассовой температуры нефти на выходе и теплового потока на поверхности трубки в зависимости от параметров потока, а также от числа закруток трубки.

Ключевые слова: теплопередача, численный расчет, геликоидный теплообменник, масло, гидродинамика, охлаждающие жидкости, тепловой поток, ламинарно-турбулентный переход, уравнение Навье-Стокса, турбулизация потока.

References

1 Kurmanova, D.Ye., Jaichibekov, N.Zh., Volkov, K.N., & Karpenko, A.G. (2022). Chislennyi raschet gidrodinamiki teplonositelei s uchetom zavisimosti viazkosti ot temperatury [Numerical calculation of fluid dynamics of heat carriers taking into account the dependence of viscosity on temperature]. *Vestnuk Evraziiskogo natsionalnogo universiteta imeni L.N. Gumilyova. Matematika. Kompiuternye nauki. Mekhanika — Bulletin of L.N. Gumilyov Eurasian National University. Mathematics. Computer science. Mechanics series, 141*(4), 28–41. https://doi.org/10.32523/2616-7182/bulmathenu.2022/4.2 [in Russian].

2 Kurmanova, D.Ye. (2022). Raspredelenie temperatury teplonositelei vdol teploobmennogo apparata [Temperature distribution of heat carriers along the heat exchanger]. *Sbornik materialov XVII Mezhdunarodnoi nauchnoi konferentsii studentov i molodykh uchenykh «Gylym zháne bilim — 2022» — Collection of materials of the XVII International Scientific Conference of Students and Young Scientists "Gylym zháne bilim — 2022",* 1603–1607. https://smart.enu.kz/api/serve?path=/general/files/6c96824d-24df-4d98-83a3-67dddf36551e.pdf [in Russian].

3 Osley, W.G., Droegemueller, P., & Ellerby, P. (2013). CFD investigation of heat transfer and flow patterns in tube side laminar flow and the potential for enhancement. *Chemical Engineering Transactions, 35,* 997–1002. DOI: 10.3303/CET1335166.

4 Karar, O., Emani, S., Gounder, S.M., Myo, Thant, M.M., Mukhtar, H., Sharifpur, M., & Sadeghzadeh, M. (2021). Experimental and numerical investigation on convective heat transfer in actively heated bundle-pipe. *Engineering Applications of Computational Fluid Mechanics, 15*(1), 848–864. https://doi.org/10.1080/19942060.2021.1920466.

5 Rana, S., Zunaid, M., & Kumar, R. (2022). CFD approach for the enhancement of thermal energy storage in phase change material charged heat exchanger. *Case Studies in Thermal Engineering, 33,* 101921. https://doi.org/10.1016/j.csite.2022.101921.

6 Borse, D., & Bute, J.V. (2018). A Review on Helical Coil Heat Exchanger. *International Journal for Research in Applied Science & Engineering Technology, 6,* 492–497. https://doi.org/10.22214/ijraset.2018.2070.

7 Inyang, U., & Uwa, I. (2022). Heat Transfer in Helical Coil Heat Exchanger. *Advances in Chemical Engineering and Science, 12,* 26–39. doi:10.4236/aces.2022.121003.

8 Volkov, K.N., & Emelyanov, V.N. (2012). Vychislitelnye tekhnologii v zadachakh mekhaniki zhidkosti i gaza [Computational technologies in fluid and gas mechanics problems]. Moscow: *Fizmatlit,* 468 [in Russian].

9 Coder, J.G. & Maughmer, M.D. (2014). Computational fluid dynamics compatible transition modeling using an amplification factor transport equation. *AIAA Journal, 52*(11), 2506–2512. https://doi.org/10.2514/1.J052905.

10 Kurmanova, D., Jaichibekov, N., Karpenko, A, & Volkov, K. (2023). Modelling and Simulation of Heat Exchanger with Strong Dependence of Oil Viscosity on Temperature. *Fluids, 8*(95), 1–18. https://doi.org/10.3390/fluids8030095.

11 Kurmanova D.E., Jaichibekov N.J., Karpenko A.G., & Volkov, K.N. (2023). Numerical modeling and calculation of heat transfer between heat carriers in heat exchangers. *Bulletin of the Karaganda University. Physics series, 1 (109),* 59–70. DOI: 10.31489/2023PH1/59-70.

Information about authors

Jaichibekov, Nurbolat — Doctor of physical and mathematical sciences, Professor, Department of Mechanics, L.N. Gumilyov Eurasian National University, Astana, Kazakhstan; e-mail: jaich@mail.ru; ORCID ID: https://orcid.org/0000-0002-3053-8288;

Kurmanova, Dinara — Postdoctoral fellow, Department of Mechanics, L.N. Gumilyov Eurasian National University, Astana, Kazakhstan; e-mail: dikonya89_29@mail.ru; ORCID ID: https://orcid.org/0009-0009-9787-7426;

Zhumanbayeva, Aizhan — Doctoral student, Department of Mechanics, L.N. Gumilyov Eurasian National University, Astana, Kazakhstan; e-mail: aizhanzhumanbayeva347@gmail.com; ORCID ID: https://orcid.org/0009-0007-2725-3672.

Article

Received: 27.12.2023
Accepted:: 16.02.2024

UDC 666.56

https://doi.org/10.31489/2024PH2/82-93

Z. Sattinova[1], B. Assilbekov[2], U. Zhapbasbayev[2], G. Ramazanova[2], G. Sagindykova[1*]

[1]*L.N. Gumilyov Eurasian National University, Astana, Kazakhstan;*
[2]*Satbayev University, Almaty, Kazakhstan*
[*]*(Corresponding author's e-mail: gibrat75@mail.ru)*

Evaluation of influence of thermoplastic slurry flow conditions on heat transfer coefficient during beryllium ceramic formation

The article presents the results of calculation of the influence of thermoplastic slurry flow conditions on the total heat transfer coefficient when forming ceramic products. Methods of detailed description of casting processes and thermal calculations have been developed to ensure reliable correspondence of calculated data and experimental results implemented on the basis of calculational experiment. The modeling of physical processes occurring during the formation of products allows you to discover new opportunities for improving the quality of castings by allowing you to more closely track the change in the temperature-phase fields of the process and clearly present the solidification kinetics depending on the casting modes. The speed of heat removal from the casting during the solidification period determines the rate of movement of the slurry, along with the temperature field on which the width of the transition region depends. These factors have a direct influence on the formation of the structure of beryllium ceramics.

The study of the heat exchange process in the formation of ceramic products depending on temperature, heat at phase transition is the main task, since they largely determine the technological and operational characteristics of beryllium ceramics. The design data allows to determine the optimal conditions of the ceramic casting process and to obtain a solidified product with a uniform structure at the outlet.

Keywords: thermoplastic slurry, beryllium oxide, hydrodynamics, heat exchange, casting process, formation, solidification process, ceramics.

Introduction

High-density ceramics made of beryllium oxide are widely used in various fields of modern technology due to a number of valuable properties and, above all, unique thermal conductivity. The slurry used to make MIM (Metal injection molding) ceramics is a dispersion system in which one phase is a solid mineral powder and the other is a thermoplastic binder [1]. The high thermal conductivity of the beryllium oxide powder during the molding step results in increased "rigidity" of the casting systems, which makes it difficult to control structure formation during slurry movement. The complexity of the process under study is that consideration should take into account factors such as the dependence of thermophysical properties on temperature, the phase transformations of liquid suspensions into a solid state, the heat of crystallization, and a sharp change in the temperature boundary conditions on the cooling circuits [2].

Creation of an effective method of controlling the process of forming thermoplastic slurry from beryllium oxide with uniform properties is a fundamental problem of foundry [3, 4]. The relevance of the problem lies in determining the optimal conditions for obtaining high-quality ceramic products in the casting process by mathematical modeling. The use of a mathematical model of physical processes occurring during the formation of products makes it possible to discover a new resource for improving the quality of castings due to the possibility of more detailed tracking of changes in temperature-phase fields during cooling [4] and to clearly present the kinetics of solidification depending on casting modes and casting configuration features.

In this regard, the tasks of evaluating the effect of the thermoplastic slurry flow *conditions* on the total heat transfer coefficient from the hot slurry to the cooling agent have been considered, in particular, heat transfer coefficients of external and internal convective flows have been determined for calculating the total heat transfer coefficient.

Mathematical description of the concentric cylinder molding process

The flow and heat exchange of beryllium oxide thermoplastic slurry in the space between two concentric cylinders with radii r_1 and r_2 is considered (Fig. 1). Liquid slurry with initial temperature of 80℃ flows into forming cavity, moving along annular gap, is cooled by water washing spinneret from outside [5]. Spinneret cooling circuit is divided into two parts, hot circuit temperature is indicated by t_1, cold circuit t_2. As it

moves, the slurry mass begins to gradually solidify, and at the exit from the cavity it acquires a structural shape in the form of a tube.

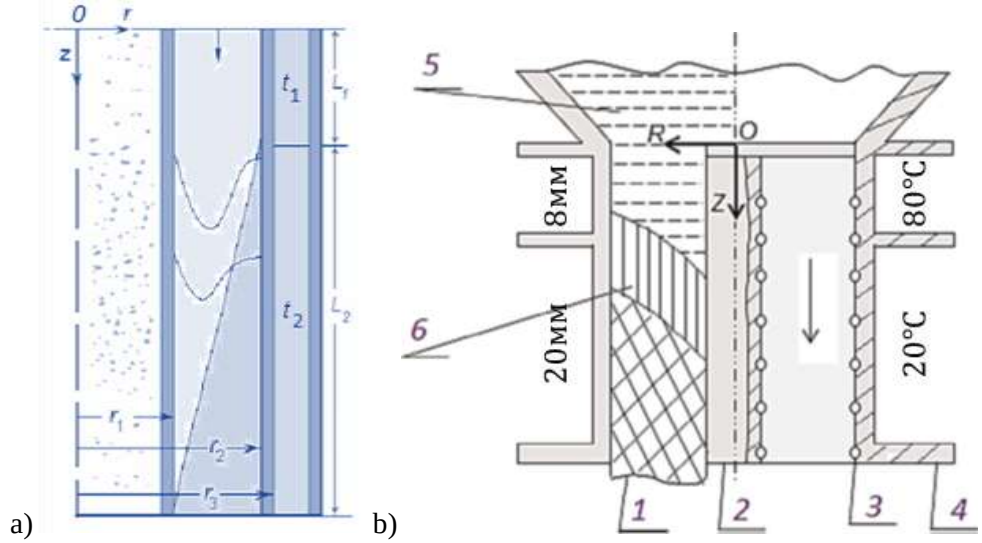

Figure 1. a) diagram of the slurry flow in the annular cavity of the casting unit
b) external diagram of the experimental installation: 1 – solidified slurry; 2 – mandrel;
3 – thermocouples; 4 – cooling circuit; 5 – hot slurry; 6 – solidification zone

The problem is investigated in a cylindrical coordinate system with $z$and$r$ axes. Axis OZ is directed along axis of cavity, and axis OR is directed radially to it. The casting speed is directed vertically down the OZaxis. The transverse component of the speed arises from the heat exchange of the liquid slurry with the walls of the annular cavity. Heat exchange with the inner wall of the annular cavity is determined by the thermal conductivity of the mandrel material. Heat exchange with external wall of annular cavity is determined by heat transfer between slurry and cooling water in circuits through the spinneret wall [5]. In cooling circuits there is intensive circulation of water at the specified flow rate.

The rheological properties of the slurry depend on the temperature. During the solidification of the slurry, the heat of the phase transition is released [6-7]. Cooling of the slurry can lead to unequal temperature profile and rheological properties of the extruded casting. Solidification will begin on the side of the walls of the annular cavity, while in the central part of the cavity the slurry may be in a liquid state. As a result, the liquid slurry may be fed to compensate for the internal shrinkage of the volume in the cooled zone of the forming cavity. The following is a mathematical model of the process of forming the slurry in the annular cavity.

The movement of the slurry in the annular cavity is considered stationary, and a system of equations of hydrodynamics closed by the Bingham model of non-Newtonian fluid in a narrow channel is used to study it [5].

$$\rho u\frac{\partial u}{\partial z}+\rho v\frac{\partial u}{\partial r}=-\frac{dp}{dz}+\frac{1}{r}\frac{\partial}{\partial r}\left(r\mu\frac{\partial u}{\partial r}\right)+\frac{1}{r}\frac{\partial}{\partial r}(r\tau_0), \tag{1}$$

$$\frac{\partial \rho u}{\partial z}+\frac{1}{r}\frac{\partial r\rho v}{\partial r}=0. \tag{2}$$

In the limit of the solid plastic state of the slurry, the equation of motion (1) expresses the extrusion of the casting from the cavity and takes the form:

$$-\frac{dp}{dz}=\frac{1}{r}\frac{\partial}{\partial r}(r\tau_0).$$

In the steady-state process of slurry solidification, the energy equation is as follows:

$$\rho u c_p\frac{\partial t}{\partial z}+\rho v c_p\frac{\partial t}{\partial r}=\frac{\partial}{\partial z}\left(\lambda\frac{\partial t}{\partial z}\right)+\frac{1}{r}\frac{\partial}{\partial r}\left(r\lambda\frac{\partial t}{\partial r}\right) \tag{3}$$

In equations (1)–(3), the following designations are taken: $z,\ r$ — axial and radial coordinates; $u,$ u are speed vector components; $p,\ \rho,\ t,\ \tau_0,\ c_p,\ \mu,\ \lambda$ — pressure, density, temperature, shear stress, apparent

heat capacity, viscosity and thermal conductivity coefficients of the slurry, respectively [6]. The condition for maintaining the mass flow rate determines the pressure gradient for extruding the slurry from the annular cavity [7]:

$$2\pi \int_{r_1}^{r_2} \rho u r dr = \pi(r_2^2 - r_1^2)\rho_0 u_0, \tag{4}$$

where r_1, r_2 — radii of mandrel and spinneret, respectively.

Distribution of speed and temperature at the inlet of the annular cavity are taken as constant over the section, accordingly, all thermophysical properties of the slurry will be constant [5].

$$\text{at } z = 0: \ u = u_0, \ v = 0, \ t = t_0. \tag{5}$$

On the walls of the cavity in the area of the liquid state of the slurry for speed, the sticking conditions are set:

$$\text{at } z > 0, r = r_i: u_i = v_1 = 0, \ i = 1,2 \tag{6}$$

and in the area of the solid plastic state — conditions of non-flow and sliding:

$$\text{at } z > 0, r = r_i: v_1 = 0, \left(\frac{\partial u}{\partial r}\right)_{r_i} = 0. \tag{7}$$

It is considered that heat from the hot slurry is transferred to the walls of the spinneret and mandrel. Then the adiabatic condition can be set on the wall of the mandrel:

$$\text{at } z > 0, \quad r = r_1, \quad \frac{\partial t}{\partial r} = 0. \tag{8}$$

Indicating the temperature of water in the hot and cold circuits through the t_1, t_2 boundary conditions can be set on the wall of the spinneret in the form of:

$$\text{at } z > 0, \quad r = r_2, \quad -\lambda \frac{\partial t}{\partial r} = k(t - t_i), \ i = 1,2, \tag{9}$$

where k — coefficient of heat transfer on the spinneret wall [8–11].

At the outlet section of the cavity for temperature the condition is set:

$$\text{at } z = l, \quad \frac{\partial t}{\partial z} = 0 \tag{10}$$

The rheological properties of the slurry at the content of the binding$\omega = 0{,}117$ depend on temperature, and are expressed by empirical formulas [6-7]. The heat of the phase transition to the energy equation (3) is determined by the method of apparent heat capacity:

$$c_p = c_s \cdot (1 - \alpha(\bar{t})) + c_l \cdot \alpha(\bar{t}) + H_{1\to 2} \frac{d\alpha}{dt}, \tag{11}$$

where c_s — heat capacity of the slurry in solid state, c_l — heat capacity of the slurry in liquid state, $\alpha(\bar{t}) = 0$ for the slurry in solid state and $\alpha(\bar{t}) = 1$ for the slurry in liquid state, $\bar{t}$ — dimensionless temperature of the slurry [9].

According to the experimental data of a slurry of oxide of beryllium the function $\alpha(\bar{t})$ has an appearance $\alpha(\bar{t}) = 5.714 \cdot \bar{t} - 2.857$. The method of apparent heat capacity allows taking into account the heat of the phase transition, and is convenient for calculations, since the positions of the transition zone are unknown in advance, and are determined as a result of calculations [7, 12].

Equations (1)–(4) were solved by fully coupled finite element method using commercial software COMSOL Multiphysics version 5.6. The area in question is divided into unit cells with $\Delta z_i, \Delta r_j$ sides [13-14]. The pressure gradient is determined by splitting to maintain mass flow (4). To obtain a finite difference analogue of the system of equations of transition (1) and energy (3), an implicit Crank-Nicolson difference scheme has been used, approximating differential equations with a second order of accuracy [14]. Difference

analogue of continuity equation (2) is solved by two-layer scheme of the second order of accuracy. When switching to differential analogues for a circuit channel, the following designations are used:

$$\Delta z = z_{n+1} - z_n, \quad \Delta r = r_{j+1} - r_{j-1}, \quad \Delta r_+ = r_{j+1} - r_j, \quad \Delta r_- = r_j - r_{j-1},$$

where $\Delta z,\ \Delta r$ change within the $0 \le \Delta \le 1$ interval. System of linear equations is presented in vector-matrix form and is solved by run-through method [13–15].

Results and discussion: One of the important goals of numerical modeling of the process under consideration is to determine the optimal conditions for creating beryllium oxide products by hot casting. In practice, this process is mainly controlled by the casting speed and hot slurry temperature [6]. The results of numerical calculations of the solidification zone of the slurry and the flow velocity profile at different casting speeds are given in Figure 2. The process of molding beryllium ceramics itself occurs in the temperature range of 80÷20℃, i.e., a thermoplastic slurry — a suspension with an initial temperature of 80℃ — flows in and moves into the forming cavity. As it moves, the slurry mass cools and hardens, acquiring a structural shape at the outlet of the pipe. Generalization of the experimental results take into account the dependence of the rheological and thermophysical properties of the thermoplastic slip on temperature in the required range of the hot casting method from 80℃ to 20℃.

As can be seen from Figure 2, the slurry flow is fully developed in the hot circuit, in which the slurry is practically not cooled, and the speed has a parabolic profile. As the slurry cools intensively in the cold path of the spinneret, the speed profile becomes rectangular in shape corresponding to the sliding speed on the wall, and the flow of the slurry becomes a solid mass motion at a constant speed.

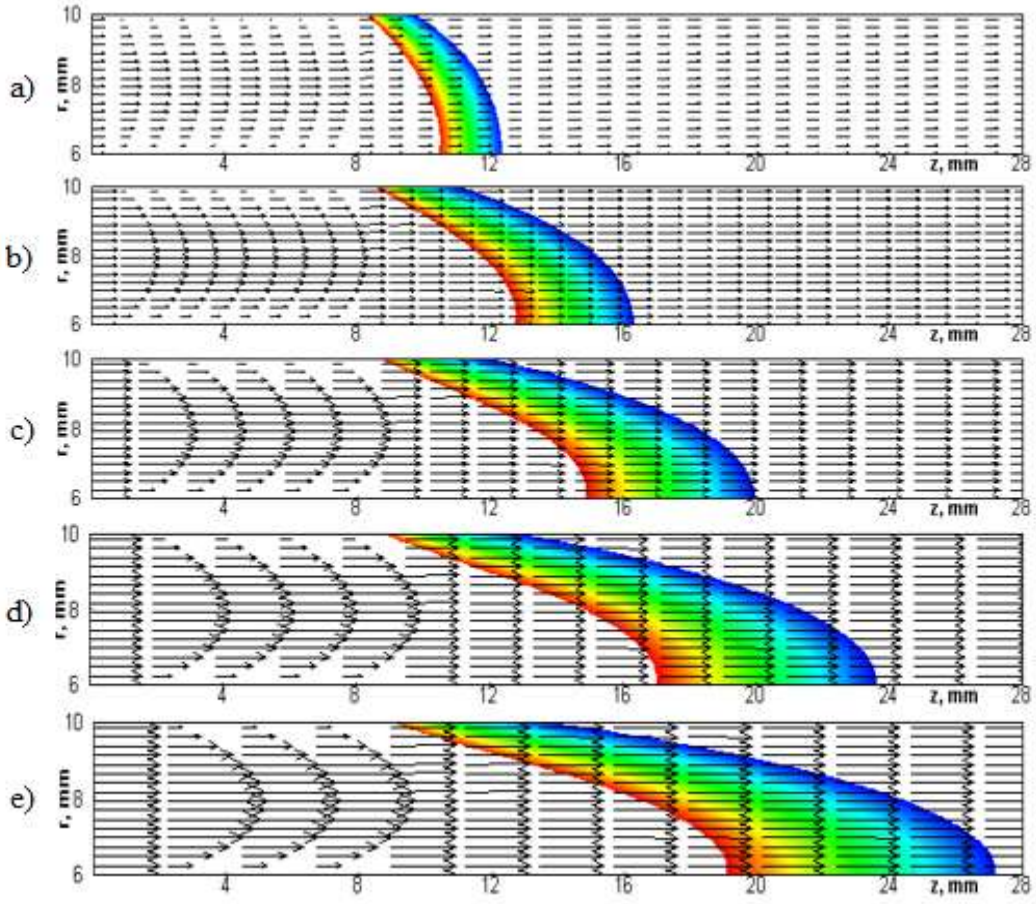

Figure 2. Slurry solidification zone and flow rate profile at different casting rates: a) u=20 mm/min; b) u=40 mm/min; c) u=60 mm/min; d) u=80 mm/min; e) u=100 mm/min.

The graphs show the solidification zone of the hot slurry as a function of the casting speed. The zone of solidification of the slurry is defined as the zone between two isochores — the lower (40°C) and upper (54°C) boundaries of crystallization of the slurry [6, 7]. The slurry is still liquid at temperatures above 54°C, and becomes solid at temperatures below 40°C, so more accurate determination of the solidification zone depending on the casting conditions is an important task. As can be seen from Figure 2, the position of the

solidification zone is transferred (extended) by the flow of the slurry. It becomes wider, especially near the inner wall of the spinneret with an increase in casting speed (Fig. 2, a-e). The results of the calculations show that an increase in the casting speed of more than 100 mm/min is not optimal, since part of the solidification zone can leave the spinneret, which leads to incomplete solidification of the slurry [16-17].

Analysis of influence of thermoplastic slurry flow conditions on total heat transfer coefficient from hot slurry to cooling agent has been performed. An important step in hot casting beryllium ceramics is to cool the hot slurry with a layer of circulating water [18-19]. When simulating the hot slurry flow, cooling can be mathematically described by the following equation of the heat flow from the slurry to the cooling agent (water)

$$q = kA_i(T_h - T_c),$$

whereA_i — the area of the inner wall of the spinneret with a length of L, T_hиT_c — the temperature of the hot slurry and cooling water, respectively, k — the total heat transfer coefficient from the hot slurry to cooling water, which according to Figure 1 is calculated by the following formula [8–11, 20]

$$k = \frac{1}{\frac{1}{h_i}+\frac{r_i}{\lambda}ln\frac{r_o}{r_i}+\frac{r_i}{r_o}\frac{1}{h_o}}, \quad (12)$$

Where h_i and h_o — internal and external coefficients of convective heat exchange, respectively, r_i, r_o — internal and external radii of the spinneret, λ — thermal conductivity of the material of the spinneret wall. The h_i and $h_o$coefficients are usually determined experimentally for a particular system and are calculated using different empirical formulas for internal and/or external fluid flow conditions. The thermal conductivity of the wall material of the spinneret λ, made of steel, grade 12X18H10T, is 15 $\frac{\text{Вт}}{\text{м*К}}$at 20°C. Like other oxide materials, the thermal conductivity of beryllium oxide decreases sharply with increasing temperature. The thermal conductivity of thermoplastic beryllium oxide slurry at temperatures of 40 and 60 ℃ are 254.3 and 181.5 W/(m·K), respectively.

Thus, in order to calculate the total heat transfer coefficient k, it is necessary to determine the convective heat exchange coefficients. To this end, consider the inner and external flows for the circular spinneret — the cooling water flow (external) in the shell by the inner and external radii $r_o r_w$ and r_i, respectively, and the hot slurry flow of beryllium oxide in the spinneret by the radius of r_i. Heat is first transferred from the hot slurry to the inner wall of the spinneret due to internal convection, then it is transferred to the external wall of the spinneret, only then enters the cooling water (Fig. 3). It is believed that there is no thermal contact layer with a certain thermal resistance between the slurry and the inner wall, external wall and water.

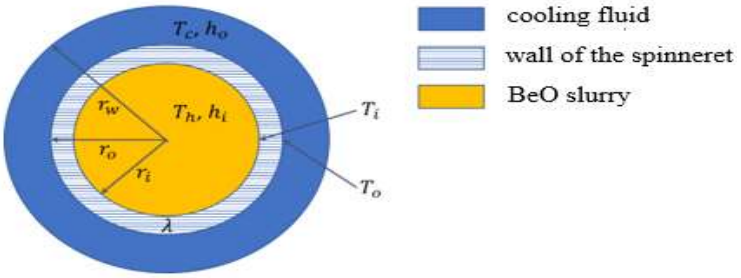

Figure 3. Schematic representation of heat flow from hot slurry to cooling water

The coefficient of external convective heat exchange can be calculated from the condition of cooling water flow in the external casing of the spinneret, which is the external flow for the spinneret. To do this, we will use the known empirical formulas for the Nusselt number $Nu_o = \frac{h_o D_o}{\lambda}$ when cooling the cylinder with an external stream of water, where the external diameter of the spinneret D_o Empirical formulas for calculating the Nusselt number are usually searched as dependencies on the Reynolds and Prandtl numbers [18].

In most cases in hot casting, all parameters except the temperature and flow rate of the circulating water are constant values. The temperature and flow rate of the circulating water (Reynolds and Prandtl numbers, respectively) may vary from series to series of experiments, but they remain constant during each series of experiments. Figures 4, 5 show the dependence of the average coefficient of external convective heat exchange on the Reynolds and Prandtl numbers. Design and physical data from experiments given in [1] have been taken as data for calculation of average coefficient of external convective heat exchange. This paper

examines an experiment to study the solidification of a hot slurry in a concentric cylinder cooled by the circulation of water in two circuits with temperatures of 20 and 80°C, respectively (Fig. 1). These temperatures are maintained by changing the hot and flow of coldwater. The height of the circuits is 8 and 20 mm, respectively, and the slurry casting speed varied from 20 to 100 mm/min, and the cold circuit water flow rate varied from 250 to 1500 l/hr., while the hot circuit water flow rate was maintained at a constant value of 500 l/hr.

In Figures 4 and 5, the coefficients of external convective heat exchange for cold and hot circuits depending on the Reynolds number have been calculated using the first and third formulas of the Nusselt number at $Pr(20℃) = 7.02$ and $Pr(80℃) = 2.22$. Note that the Reynolds number corresponds to the flow rate of cold water of 1000 to 1900 ml/min, and hot water from 100 to 1000 ml/min. As shown in Figures 4 and 5, the coefficients of external convective heat exchange calculated by both formulas increase with the Reynolds number, that is, the flow rate of water in two circuits.

Three empirical formulas are considered — Hilpert's (Nu_{o1}), Zukauskas (Nu_{o2}) and Churchill-Bernstein (Nu_{o3}) formulas Table 1 [18]. As can be seen from Table 1, the first two formulas work in limited intervals of Reynolds and Prandtl numbers, while the third formula works in a wide range of these numbers. The coefficients C_1, C_2, and the indicators m, n are functions of the numberRe_D, and are shown in Tables 2 and 3.

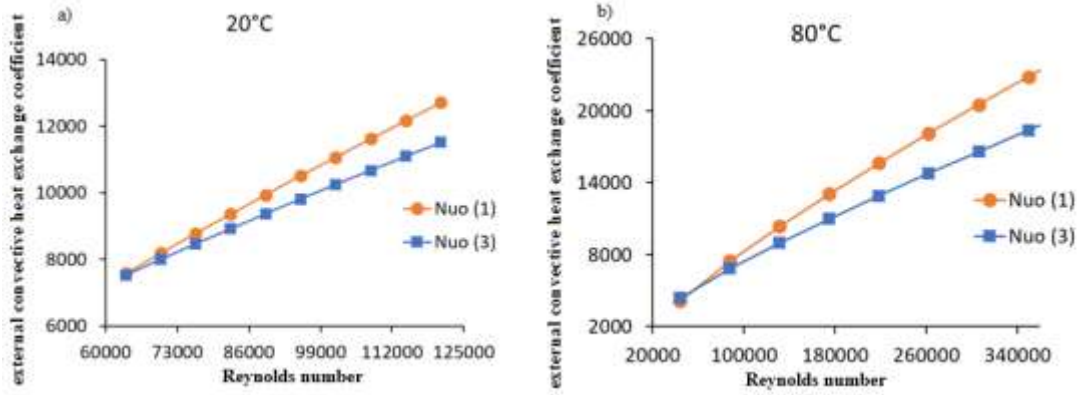

Figure 4. Dependence of external convective heat exchange coefficient h_o for a) cold circuit ($Pr(20℃) = 7.02$) and b) hot circuit $Pr(80℃) = 2.22$ on Reynolds number calculated from formulas 1 and 3 of Nusselt number

Table 1

Empirical correlations of Nusselt number for cylinder

Empirical formula	Note
$Nu_{o1} = C_1 Re_D^m Pr^{1/3}$	$0.4 \lesssim Re_D \lesssim 4 \cdot 10^5$, $Pr \gtrsim 0.7$
$Nu_{o2} = C_2 Re_D^n Pr^q \left(\frac{Pr}{Pr_s}\right)^{1/4}$	$1 \lesssim Re_D \lesssim 10^6$, $0.7 \lesssim Pr \lesssim 500$
$Nu_{o3} = 0.3 + \frac{0.62 Re_D^{1/2} Pr^{1/3}}{\left[1 + \left(\frac{0.4}{Pr}\right)^{2/3}\right]^{1/4}} \left[1 + \left(\frac{Re_D}{282000}\right)^{5/8}\right]^{4/5}$	$Re_D Pr \gtrsim 0.2$

Tab. 2. Values of C_1 and m for the formula Nu_{01}

Re_D	C_1	m
0.4-4	0.989	0.330
4-40	0.911	0.385
40-4000	0.683	0.466
4000-40000	0.193	0.618
40000-400000	0.027	0.805

Tab. 3. Values of C_2 and n for the formula Nu_{02}

Re_D	C_2	n
1-40	0.750	0.4
40-1000	0.510	0.5
1000-200000	0.260	0.6
200000-1000000	0.076	0.7

In addition, the difference in the coefficients of external convective heat exchange increases with an increase in the Reynolds number, and the maximum difference is 10 and 25% at 20 and 80℃, respectively. This shows that both formulas (the Hilpert and Churchill-Bernstein formulas) are suitable for calculating the coefficient of external convective heat exchange, but it is preferable to use the third formula (Churchill-Bernstein) as it operates over a wide range of changes in Reynolds and Prandtl numbers.

In the case of internal flow, the Reynolds, Prandtl and Nusselt numbers are determined by the following formulas

$$Re_D = \frac{U_{cast} D_o}{\nu_{sl}};\ Pr = \frac{\mu_{sl} c_{psl}}{\lambda_{sl}};\ Nu_i = \frac{h_i D_i}{\lambda_{sl}}.$$

U_{cast} — casting speed, D_i — inner diameter of the spinneret, ν_{sl},μ_{sl} — kinematic and dynamic viscosity of slurry, c_{psl},λ_{sl} — heat capacity and thermal conductivity of slurry.

In the internal flow of the fluid, correlation dependencies of the Nusselt number are used, as in the case of external flow. There are various dependencies of the Nusselt number on the Reynolds and Prandtl number for laminar and turbulent currents. Works [18–21] give empirical formulas for calculation of Nusselt number at flow of various liquids between concentric cylinders (coaxial tube). In this case, we will confine ourselves to calculating the coefficient of internal convective heat exchange based on the Nusselt number on the flow of the thermoplastic slurry in the cylindrical tube.

As it is known, in the case of a fully developed laminar flow with a uniform heat flow on the cylinder wall and a uniform distribution of the wall temperature, the Nusselt number is constant and equals 4.36 and 3.66, respectively [18]. But, when the thermoplastic slurry flows in the cylindrical tube, its intensive cooling takes place, moreover, uneven, through the wall, which leads to a possible change in the speed profiles along the cylinder, which dictates the use of a non-constant Nusselt number, at least along the length of the tube. Since the slurry is a highly viscous liquid, its flow in the cylinder differs with a large Prandtl number, which leads to the choice of empirical formulas for calculating Nusselt, working for such a flow. For the case in question, i.e. for a course with Prandtl number $Pr \gtrsim 5$ the following Nusselt equation is suitable

$$Nu_{i4} = 3.66 + \frac{0.0668 \frac{D_i}{L} Re_D Pr}{1 + 0.04 \left(\frac{D_i}{L} Re_D Pr\right)^{2/3}}. \quad (13)$$

Slurry casting occurs when the temperature changes from 80 to 20℃, which corresponds to the Prandtl number of 1300–22000. Casting speed varies from 20 to 100 mm/min [1], which corresponds to Reynolds number on the order of ~10^{-4}-10^{-3}. Figure 6 shows the change in the internal convective heat exchange coefficient of h_i, calculated from the Nusselt number Nu_{i4}, according to the Reynolds number at$Pr(50℃) = 5700$ and $Pr(60℃) = 3584$. The coefficient of internal convective heat exchange increases with an increase in Reynolds number and a decrease in Prandtl number, but it is significantly lower than the coefficient of external convective heat exchange (Fig. 4 a-b). Figure 7 shows the dependence of the Nusselt number for the inner current on the Reynolds number for $Pr(50℃) = 5700$ and $Pr(60℃) = 3584$. The Nusselt number calculated using the last formula (13) varies around the Nusselt number values for a fully developed laminar flow with uniform heat flow on the cylinder wall and uniform wall temperature distribution.

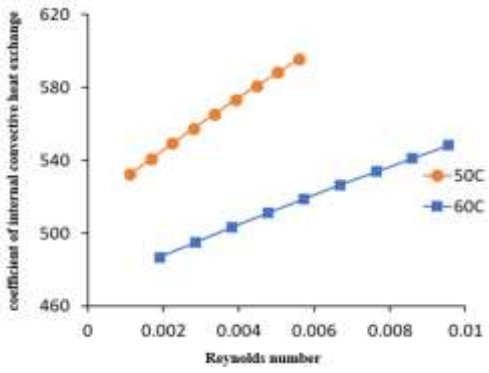

Figure 5. Dependence of the coefficient of internal convective heat exchange h_0 on the Reynolds number for $Pr(50℃) = 5700$and$Pr(60℃) = 3584$

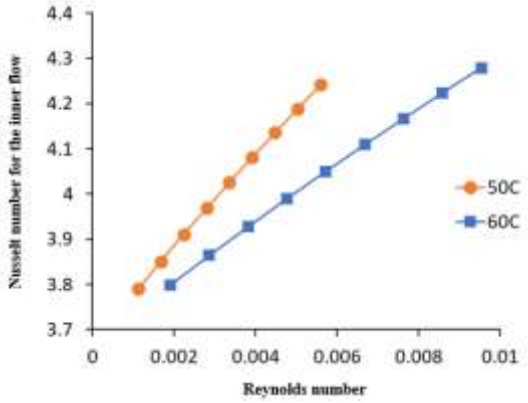

Figure 6. Dependence of the Nusselt number for the inner flow on the Reynolds number for

$$Pr(50℃) = 5700 \text{ and } Pr(60℃) = 3584.$$

The dependence of the total heat transfer coefficient k on the hot slurry to cold water on the Reynolds number of the internal flow at different Reynolds numbers of the water flow in the cold circuit, calculated using the formula (13), is presented. This factor is used in modeling the flow of a hot slurry that cools through the walls when the temperature changes in the spinneret wall material is neglected, which is not always a correct assumption. This means that in some cases, especially when the heat transfer rate through the wall material is of the same order with the heat transfer rate in the layers near the wall, or when the spinneret wall is not thin.

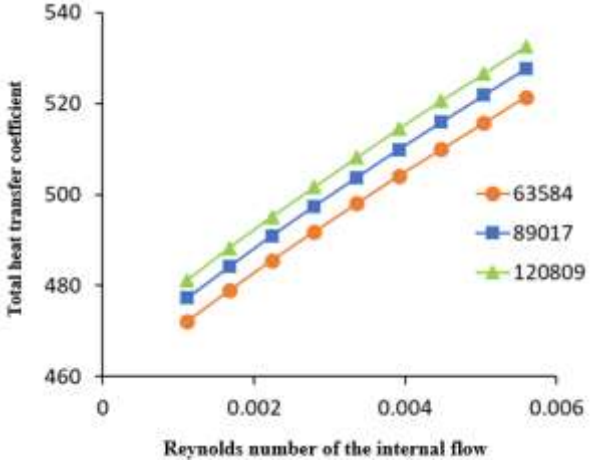

Figure 7. The dependence of the total coefficient on hot slurry to cold water on the Reynolds number of the internal flow at different Reynolds numbers of the water flow in the cold circuit

As shown in Figure 6, the heat transfer coefficient k increases as the Reynolds number of internal and external flows increases. It is also noted that k is mainly controlled by internal convective heat exchange, for which the coefficient of heat exchange is significantly lower than the coefficient of external heat exchange.

Conclusions

Thermal calculations of the laminar flow of the slurry in the cavity formed by two concentrically arranged pipes during the formation of beryllium ceramics have been carried out. From analysis of experimental data and calculations having obtained during movement of viscoplastic slurry in concentric circular channel, it is established that with increase of cooling water flow rate in two circuits, external convective heat exchange coefficients increase. Heat exchange and heat transfer coefficients on the walls of the annular cavity have been estimated according to special criterion relationships.

Experimental data having obtained from the study of hydrodynamics and heat exchange of the casting process of ceramic products have been analyzed and generalized using a mathematical model. The system of equations of the laws of conservation of impulse, mass and energy of non-Newtonian fluid is considered

together with the Shvedov-Bingham rheological model. Rheological and thermophysical properties of the slurry have been found on the basis of experimental data, and express dependence on temperature.

Zones of solidification of hot slurry depending on casting speed have been identified. The zone of solidification of the slurry is defined as the zone between two isochores — the lower (40°C) and upper (54°C) boundaries of crystallization of the slurry. The structure of the slurry crystallization front shows that the crystallization rate depends on the mode parameters and channel design data. The use of constructive and experimental data for calculating the average coefficient of external convective heat exchange and the Nusselt number in dependence on the Reynolds and Prandtl numbers makes it possible to obtain temperature and speed profiles explaining the physical essence of the phenomenon, i.e. the process of solidification of the thermoplastic slurry in the annular cavity.

Acknowledgements.

This work is supported by the Science Committee of the Ministry of Science and Higher Education of the Republic of Kazakhstan (Grant number AP19680086 for 2023–2025)

References

1 Шахов С. Применение ультразвука в производстве керамических изделий с высокой теплопроводностью / С. Шахов, Г. Бицоев. — Усть-Каменогорск: ВКТУ, 1999.

2 Akishin G. et al. Composition of beryllium oxide ceramics / G. Akishin, S. Turnaev, V. Vaispapir et al. // Refractories and Industrial Ceramics. — 2011. — Vol. 51. — P. 377–381. https://doi.org/10.1007/s11148-011-9329-6

3 Shakhov S. Controlling the deformation behavior of thermoplastic slips with ultrasound / S. Shakhov // Glass and Ceramics. 2007. — Vol. 64. — P. 354–356. https://doi.org/10.1007/s10717-007-0088-2

4 Shakhov S.A. Mechanism for compensating slip volume changes during hot casting of ceramic / S.A. Shakhov // Glass Ceram. — 2007. — Vol. 64. — P. 229–231. https://doi.org/10.1007/s10717- 007-0057-9

5 Zhapbasbayev U. Modeling of the beryllia ceramics formation process / U. Zhapbasbayev, G. Ramazanova, Z. Sattinova, A. Shabdirova // Journal of the European Ceramic Society. — 2013. — Vol. 33. — Issue 8. — P. 1403–1411. https://doi.org/10.1016/j.jeurceramsoc.2013.01.010

6 Zhapbasbayev U. et al. Experimental and calculated data of the beryllium oxide slip solidification / U. Zhapbasbayev, G. Ramazanova, B. Kenzhaliyev et al. // Appl. Therm. Eng. — 2016. — Vol. 96. — P. 593–599. https://doi.org/10.1016/j.applthermaleng.2015.11.114

7 Sattinova Z.K. Mathematical modeling of the rheological behavior of thermoplastic slurry in the molding process of beryllium ceramics / Z.K. Sattinova, T.N. Bekenov, B.K. Assilbekov, G.I. Ramazanova, U.K. Zhapbasbayev, Zh.T. Nussupbek // Ceramics International. — 2022. — Vol. 48. — Issue 21. — P. 31102–31110. https://doi.org/10.1016/j.ceramint.2022.07.178

8 Cebeci T. Physical and Computational Aspects of Convective Heat Transfer / T. Cebeci, P. Bradshaw. — 1988. https://doi.org/10.1007/978-1-4612-3918-5.

9 Shulman Z.P. Convective Heat and Mass Transfer of Rheologically Complex Liquids / Z.P. Shulman // Energy. Moscow, 1975.

10 Kiiko V.S. Thermal conductivity and prospects for application of BeO ceramic in electronics / V.S. Kiiko, V.Y. Vaispapir // Glass Ceram. — 2015. — Vol. 71. — P. 387–391. https://doi.org/10. 1007/s10717-015-9694-6.

11 Vajdi M. et al. Numerical assessment of beryllium oxide as an alternative material for micro heat exchangers / M. Vajdi, M. Shahedi Asl, S. Nekahi, F.S. Moghanlous, Jafargholinejad, M. Mohammadi // Ceram. Int. — 2020.— Vol. 46. — P. 19248–19255. https:// doi.org/10.1016/j.ceramint.2020.04.263.

12 Smolsky M. et al. Rheodynamics and Heat Transfer of Nonlinear Viscous Plastic Materials / M. Smolsky, Z.P. Shulman, V.M. Gorislavets. — Minsk: Science and technology. — 1970. — P. 443.

13 Patankar S. Numerical Methods for Solving Problems of Heat Transfer and Fluid. Mechanics / S. Patankar. M.: Energoatomizdat, 1984.

14 John C. Tannehill et al. Computational Fluid. Mechanics and Heat Transfer / C. John Tannehill, A. Dale Anderson, H. Richard Pletcher. — 2012. — 763 p.

15 Samarskii A.A. The Theory of Difference Schemes / A.A. Samarskii // Marcel Dekker, Inc. — New York, 2001. — p. 762, https://doi.org/10.1201/9780203908518

16 Miura A. et al. Observing and Modeling the Sequential Pairwise Reactions that Drive Solid-State Ceramic Synthesis / A. Miura, C.J. Bartel, Y. Goto, Y. Mizuguchi, C. Moriyoshi, Y. Kuroiwa, … W. Sun // Advanced Materials. — 2021. — Vol. 33(24). — P. 2100312. doi:10.1002/adma.202100312

17 Sattinova Z.K. Development of the algorithm for calculating the optimal molding modes of the BeO slurry using various rheological models / Z.K. Sattinova, T.N. Bekenov, B.K. Assilbekov, G.I. Ramazanova, K.M. Dyusenov // Bulletin of the University of Karaganda – Physics. — 2021. — Vol. 4 (104). doi 10.31489/2021PH4/85-93.

18 Incropera, P.F. et al. Fundamentals of Heat and Mass Transfer (6th ed.) / P.F. Incropera, P.D. Dewitt, L.T. Bergman, S.A. Lavine // John Wiley & Sons, Inc. — 2007.

19 Bennon, W.D. A continuum model for momentum, heat and species transport in binary solid-liquid phase change systems- I. Model formulation / W.D. Bennon, F.P. Incropera // Int. J. Heat Mass Trans. — 1987. — Vol. 30. — P. 2161–2170. https://doi.org/10.1016/0017-9310(87) 90094-9.

20 Davis E.S. Heat Transfer and Pressure Drop in Annuli / E.S. Davis // Journal of Fluids Engineering. — 1943. — Vol. 65(7). — P. 755–759. https://doi.org/10.1115/1.4018918

21 Stein R.P. Heat transfer to water in turbulent flow in internally heated annuli / R.P. Stein, W. Begell // AIChE Journal. — 1958. — Vol. 4(2). — P. 127–131. https://doi.org/10.1002/aic.690040203

З. Сатинова, Б. Асилбеков, У. Жапбасбаев, Г. Рамазанова, Г. Сагындыкова

Бериллий керамикасын формалау процесінде термопласт шликерін ағыс шарттарының жылу тасымалдау шамасына әсерін бағалау

Мақалада керамикалық бұйымдарды қалыптау кезінде термопластикалық шликер ағыны жағдайларының жалпы жылу беру коэффициентіне әсерін бағалау нәтижелері келтірілген. Есептеу эксперименті негізінде жүзеге асырылатын есептеу деректері мен эксперименттік нәтижелердің сенімді сәйкестігін қамтамасыз ететін құю процестері мен жылу есептеулерінің егжей-тегжейлі сипаттау әдістері әзірленді. Өнімдерді қалыптау кезінде пайда болатын физикалық процестерді модельдеу процестің температуралық-фазалық өрістерінің өзгеруін егжей-тегжейлі бақылау мүмкіндігі арқылы құйма сапасын жақсартудың жаңа мүмкіндіктерін анықтауға және құю режимдеріне байланысты қатаю кинетикасын көрнекі түрде пайдалануға мүмкіндік береді. Қатаю кезеңінде қалыптаудан жылудың бөліну жылдамдығы суспензия қозғалысының жылдамдығын, сонымен қатар өтпелі аймақтың ені тәуелді болатын температура өрісін анықтайды. Бұл факторлар бериллий керамикасының құрылымын қалыптастыруға тікелей әсер етеді. Фазалық ауысу кезінде температура мен жылуға байланысты керамикалық бұйымдарды қалыптау кезінде жылу алмасу процесін зерттеу негізгі міндет болып табылады, өйткені олар бериллий керамикасының технологиялық және пайдалану сипаттамаларын айтарлықтай анықтайды. Есептік деректер керамиканы қалыптау процесінің оңтайлы шарттарын анықтауға және біртекті құрылымы бар қатайтылған өнімді шығаруға мүмкіндік береді.

Кілт сөздер: термопластикалық шликер, бериллий оксиді, гидродинамика, жылу алмасу, құю процесі, қалыптау, қатаю.

З. Сатинова, Б. Асилбеков, У. Жапбасбаев, Г. Рамазанова, Г. Сагындыкова

Оценка влияния условий течения термопластичного шликера на коэффициент теплопередачи при формовании бериллиевой керамики

В статье представлены результаты расчетов оценки влияния условий течения термопластичного шликера на общий коэффициент теплопередачи при формовании керамических изделий. Разработаны методы детального описания процессов литья и тепловых расчетов, обеспечивающие достоверное соответствие расчетных данных и экспериментальных результатов, реализуемых на основе вычислительного эксперимента. Моделирование физических процессов, происходящих при формовании изделий, позволяет обнаружить новые возможности повышения качества отливок за счет возможности более детального отслеживания изменения температурно-фазовых полей процесса и наглядно представить кинетику затвердевания в зависимости от режимов литья. Скорость отвода тепла от формовки в период затвердевания определяет скорость движения суспензии, наряду с этим и температурное поле, от которого зависит ширина переходной области. Эти факторы оказывают непосредственное влияние на формирование структуры бериллиевой керамики. Исследование процесса теплообмена при формовании керамических изделий в зависимости от температуры, теплоты при фазовом переходе является основной задачей, поскольку они во многом определяют технологические и эксплуатационные характеристики бериллиевой керамики. Расчетные данные позволяют определить оптимальные условия процесса формования керамики и получить на выходе затвердевшее изделие с однородной структурой.

Ключевые слова: термопластичный шликер, оксид бериллия, гидродинамика, теплообмен, процесс литья, формования, затвердевания.

References

1 Shakhov, S., & Bitsoev, G. (1999). Primenenie ultrazvuka v proizvodstve keramicheskikh izdelii s vysokoi teploprovodnostiu [Application of Ultrasound in the Manufacture of High Thermal Conductivity Ceramic Articles]. Ust-Kamenogorsk: Vostochno-Kazakhstanskii tekhnicheskii universitet [in Russian].

2 Akishin, G., Turnaev, S., Vaispapir, V., et al. (2011). Composition of beryllium oxide ceramics. *Refractories and Industrial Ceramics, 51*, 377–381. https://doi.org/10.1007/s11148-011-9329-6

3 Shakhov, S. (2007). Controlling the deformation behavior of thermoplastic slips with ultrasound. *Glass and Ceramics, 64*, 354–356. https://doi.org/10.1007/s10717-007-0088-2

4 Shakhov, S.A. (2007). Mechanism for compensating slip volume changes during hot casting of ceramic. *Glass Ceram, 64* 229–231. https://doi.org/10.1007/s10717- 007-0057-9

5 Zhapbasbayev, U., Ramazanova, G., Sattinova, Z., & Shabdirova, A. (2013). Modeling of the beryllia ceramics formation process. *Journal of the European Ceramic Society, 33*(8), 1403–1411. https://doi.org/10.1016/j.jeurceramsoc.2013.01.010

6 Zhapbasbayev, U., Ramazanova, G., Kenzhaliyev, B., et al. (2016). Experimental and calculated data of the beryllium oxide slip solidification. *Appl. Therm. Eng., 96*, 593–599. https://doi.org/10.1016/j.applthermaleng.2015.11.114

7 Sattinova, Z.K., Bekenov, T.N., Assilbekov, B.K., Ramazanova, G.I., Zhapbasbayev, U.K., & Nussupbek, Zh.T. (2022). Mathematical modeling of the rheological behavior of thermoplastic slurry in the molding process of beryllium ceramics. *Ceramics International, Vol. 48, Issue 21, 31102–31110.* https://doi.org/10.1016/j.ceramint.2022.07.178

8 Cebeci, T. & Bradshaw, P. (1988). *Physical and Computational Aspects of Convective Heat Transfer*. https://doi.org/10.1007/978-1-4612-3918-5.

9 Shulman, Z.P. (1975). Convective Heat and Mass Transfer of Rheologically Complex Liquids. *Energy*. Moscow.

10 Kiiko, V.S., & Vaispapir, V.Y. Thermal conductivity and prospects for application of BeO ceramic in electronics. *Glass Ceram., 71*, 387–391, https://doi.org/10. 1007/s10717-015-9694-6.

11 Vajdi, M., Shahedi Asl, M., Nekahi, S., Moghanlous, F.S., Jafargholinejad, & Mohammadi, M. (2020). Numerical assessment of beryllium oxide as an alternative material for micro heat exchangers. *Ceram. Int., 46*, 19248–19255. https://doi.org/10.1016/j.ceramint.2020.04.263.

12 Smolsky, M., & Shulman, Z.P., & Gorislavets, V.M. (1970). *Rheodynamics and Heat Transfer of Nonlinear Viscous Plastic Materials.* Minsk: Science and technology, p. 443.

13 Patankar, S. (1984). *Numerical Methods for Solving Problems of Heat Transfer and Fluid. Mechanics*. Moscow: Energoatomizdat.

14 John, C. Tannehill, Dale A. Anderson, & Richard, H. Pletcher. (2012). *Computational Fluid. Mechanics and Heat Transfer*. 763 p.

15 Samarskii, A.A. (2001). The Theory of Difference Schemes, Marcel Dekker, Inc., New York, p. 762, https://doi.org/10.1201/9780203908518

16 Miura, A., Bartel, C.J., Goto, Y., Mizuguchi, Y., Moriyoshi, C., Kuroiwa, Y., … & Sun, W. (2021). Observing and Modeling the Sequential Pairwise Reactions that Drive Solid-State Ceramic Synthesis. *Advanced Materials, 33*(24), 2100312. doi:10.1002/adma.202100312

17 Sattinova, Z.K., Bekenov, T.N., Assilbekov, B.K., Ramazanova, G.I., & Dyusenov, K.M. (2021). Development of the algorithm for calculating the optimal molding modes of the BeO slurry using various rheological models. *Bulletin of the University of Karaganda – Physics, 4* (104). doi 10.31489/2021PH4/85-93.

18 Incropera, P.F., Dewitt, P.D., Bergman, L.T., & Lavine, S.A. (2007). Fundamentals of Heat and Mass Transfer (6th ed.). John Wiley & Sons, Inc.

19 Bennon, W.D. & Incropera, F.P. (1987). A continuum model for momentum, heat and species transport in binary solid-liquid phase change systems- I. Model formulation. *Int. J. Heat Mass Trans., 30*, 2161–2170. https://doi.org/10.1016/0017-9310(87) 90094-9.

20 Davis, E.S. (1943). Heat Transfer and Pressure Drop in Annuli. *Journal of Fluids Engineering, 65*(7), 755–759. https://doi.org/10.1115/1.4018918

21 Stein, R.P. & Begell, W. (1958). Heat transfer to water in turbulent flow in internally heated annuli. *AIChE Journal, 4*(2), 127–131. https://doi.org/10.1002/aic.690040203

Information about authors

Sattinova, Zamira — Candidate of physical and mathematical sciences, Associate Professor, L.N. Gumilyov Eurasian National University, Astana, Kazakhstan; e-mail: sattinova.kz@gmail.com; ORCID ID: https://orcid.org/0000-0002-2990-6581;

Assilbekov, Bakytzhan — Ph.D, Associate Professor, Satbayev University, Almaty, Kazakhstan. Email: b.assilbekov@satbayev.university; ORCID ID:https://orcid.org/0000-0002-0368-0131;

Zhapbasbayev, Uzak — Doctor of technical sciences, Professor, Head of the Research and Production Laboratory “Modeling in Energy”, Satbayev University, Almaty, Kazakhstan; e-mail: uzak.zh@mail.ru; ORCID ID: https://orcid.org/0000-0001-5973-5149;

Ramazanova, Gaukhar — Candidate of physical and mathematical sciences, Leading Researcher. Research and Production Laboratory “Modeling in Energy”, Satbayev University, Almaty, Kazakhstan; e-mail: g.ramazanova@satbayev.university; ORCID ID:https://orcid.org/0000-0002-8689-9293;

Sagyndykova, Gibrat — Candidate of physical and mathematical sciences, Associate Professor, L.N. Gumilyov Eurasian National University, Astana, Kazakhstan; e-mail: gibrat75@mail.ru; ORCID ID:https://orcid.org/0000-0001-5792-8799.